NASA Contractor Report 4011

Development of a Sensitive Superconducting Gravity Gradiometer for Geological and Navigational Applications

H. J. Paik and J-P. Richard

CONTRACT NAS8-33822
SEPTEMBER 1986

NASA

NASA Contractor Report 4011

Development of a Sensitive Superconducting Gravity Gradiometer for Geological and Navigational Applications

H. J. Paik and J-P. Richard
University of Maryland
College Park, Maryland

Prepared for
George C. Marshall Space Flight Center
under Contract NAS8-33822

National Aeronautics
and Space Administration

Scientific and Technical Information Branch

1986

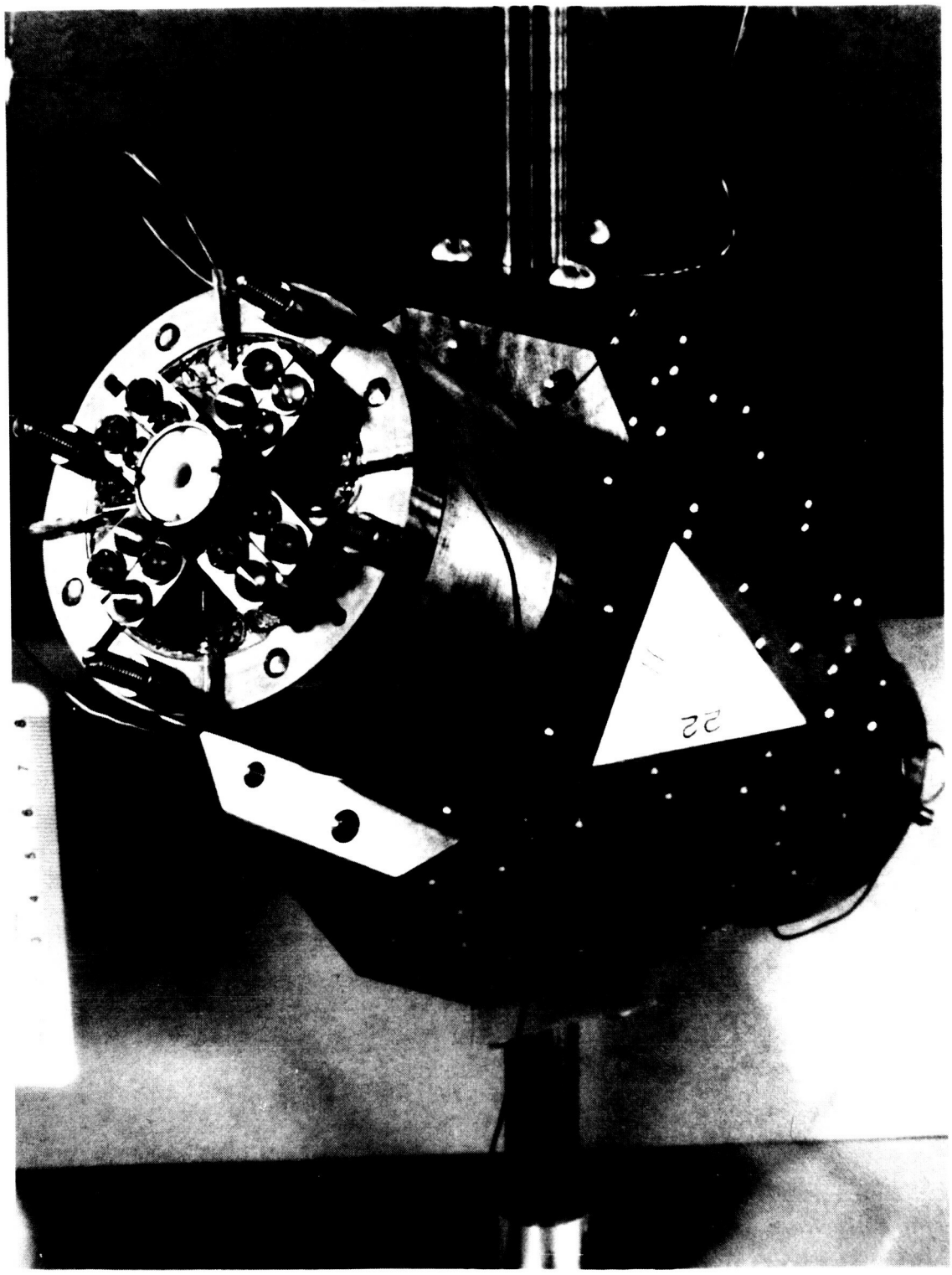

PROTOTYPE SUPERCONDUCTING GRAVITY GRADIOMETER

PREFACE

This report describes research on the superconducting gravity gradiometer program performed at the University of Maryland from July 1980 to July 1985 under NASA Contract NAS8-33822.

This report consists of three main parts: Parts 1 and 2 describing the theoretical and experimental work on a prototype superconducting gravity gradiometer, respectively, and Part 3 discussing the design of a new advanced model of superconducting gradiometer. These three parts represent three separate papers being submitted for publication. In addition, two published papers, one reporting a null test of the gravitational inverse square law performed with the prototype superconducting gradiometer and the other discussing space applications of the advanced three-axis instrument, are attached as appendices.

An advanced three-axis superconducting gravity gradiometer, designed along the line proposed in Part 3 of this report, is being developed under new NASA Contract NAS8-36165. An associated instrument, a six-axis superconducting accelerometer, is under development with support from AFGL under Contract F19628-85-K-0042. Electronic control of the gradiometer has been supported in part by Army Contract DACA-72-84-C-0004.

TABLE OF CONTENTS

LIST OF FIGURES

LIST OF TABLES

SUMMARY

A sensitive and stable gravity gradiometer is needed for precision tests of fundamental laws of physics and for moving-base gravity survey and inertial guidance. Through the five years of research and development at the University of Maryland we have demonstrated the feasibility that superconducting technology can be utilized not only to lower the intrinsic noise of the instrument but also to meet many practical challenges of operating a sensitive gravity measuring instrument in a noisy environment.

A relatively simple prototype single-axis superconducting gravity gradiometer has been constructed to investigate the basic physics of a superconducting gradiometer. At the same time, a detailed analysis of the instrument dynamics has been carried out including extensive error modelling. Thorough experimental tests of the instrument have shown that the superconducting device closely follows the analytical model. The performance level of $0.3 \sim 0.7$ E $Hz^{-1/2}$ (1 E $\equiv 10^{-9} s^{-2}$) achieved with this instrument in the laboratory without any active control or compensation represents the best reported sensitivity of any gradiometer to date. The instrument has already been used successfully to perform a new null test of the gravitational inverse square law.

Based on the experience obtained with this first instrument and additional superconducting technologies developed to improve the performance of the superconducting gradiometer, an advanced design of a three-axis superconducting gravity gradiometer has been produced. Incorporated into the new design are the concepts of a "superconducting negative spring", "three-dimensional residual common mode balance" and a "six-axis superconducting accelerometer." Various feedbacks will be applied to control the instrument and the platform. This second generation superconducting gravity gradiometer should be able to

meet the instrument noise goal, 3×10^{-4} E $Hz^{-1/2}$, defined for NASA's Gravity Gradiometer Mission (GGM).

Part 1 of this report discusses the theory of the superconducting gravity gradiometer. Although the particular superconducting circuit used for the prototype is analyzed here, the method and results are quite general and can be readily applied to the new model. Part 2 reports details of the design, fabrication, and various tests of the single-axis gradiometer. Calibration experiments performed by using gravity gradient signals are described here. Part 3 contains the design and theoretical analysis of the new gradiometer. It is found that the improved common mode rejection characteristic and the ease of g-nulling in the new instrument would enable its operation in a more hostile terrestrial moving-base environment. A null test of the inverse square law by use of the superconducting gradiometer is reported in Appendix I. Finally, the basic concept of GGM is discussed in Appendix II.

The Maryland superconducting gravity gradiometer project has served as an excellent training ground for physicists. A strong Ph.D. thesis was produced on the development of the prototype gradiometer and the test of the inverse square law (Chan, 1982). Another Ph.D. thesis is nearing completion on the development of the six-axis accelerometer. A third student is testing a transducer concept for the cryogenic gravitational wave detector, which came as a spin-off from the gradiometer project. The many challenges that one has to overcome to realize the fabulous sensitivity of the space-borne gravity gradiometer, orders of magnitude beyond the state of the art, and the exotic new technologies being invented to meet them have been inspirational to the scientific team of the Maryland gravity gradiometer project.

PART 1

THEORY OF A SUPERCONDUCTING GRAVITY GRADIOMETER

SUPERCONDUCTING GRAVITY GRADIOMETER FOR SENSITIVE GRAVITY MEASUREMENTS:

I. THEORY*

H.A. Chan and H.J. Paik
Department of Physics and Astronomy,
Univeristy of Maryland, College Park, MD 20742

Due to the Equivalence Principle, a global measurement is necessary to distinguish gravity from acceleration of the reference frame. A gravity gradiometer is therefore an essential instrument needed for precision tests of gravity laws and for applications in gravity survey and inertial navigation. Superconductivity and SQUID (Superconducting QUantum Interference Device) technology can be used to obtain a gravity gradiometer with very high sensitivity and stability. A superconducting gravity gradiometer has been developed for a null test of the gravitational inverse square law and spaceborne geodesy. Here we present a complete theoretical model of this instrument. Starting from dynamical equations for the device, we derive transfer functions, common mode rejection characteristic, and an error model of the superconducting instrument. Since a gradiometer must detect a very weak differential gravity signal in the midst of large platform accelerations and other environmental disturbances, the scale factor and common mode rejection stability of the instrument is extremely important in addition to its immunity to temperature and electromagnetic fluctuations. We show how flux quantization, the Meissner effect and properties of liquid helium can be utilized to meet these challenges.

*Work supported by NASA under contract No. NAS 8-33822.

I. INTRODUCTION

Highly sensitive gravity sensors are needed to investigate fundamental properties of gravitation and to improve accuracies of gravity survey and inertial navigation. Torsion balances have been used over two centuries for sensitive gravity experiments [1]. Spring-mass, pendulum, and free-fall type gravimeters [2] have been developed as survey instruments as well as a superconducting version of the first type [3]. Research to develop detectors for gravitational waves of extraterrestrial origin has started over two decades ago [4]. Cryogenic mass-quadrupole type and laser interferometer type detectors are under vigorous development [5]. The last two decades have also seen dedicated efforts to develop room temperature gravity gradiometers [6-8] for moving base survey applications. Superconducting gravity gradiometers have emerged more recently as an outgrowth of the superconducting transducer work for low temperature gravitational wave detectors [9].

The extremely weak nature of gravitational interaction poses a challenge to the state of the art technology for signal transduction and amplification as well as isolation of environmental noise. To compound the problem, the gravitational field cannot be distinguished in a local measurement from acceleration of the reference frame by the Equivalence Principle. In order to separate gravity from frame accelerations, one must resort to a second order measurement using the tensor nature of gravitational field gradient or "gravity gradient". When the platform is undergoing a linear acceleration, a differential measurement over a baseline between two proof masses will cancel out the acceleration noise, leaving gravity to be detected as the signal. Likewise, an angular acceleration can be taken out by combining signals from four proof masses as we will see in Section II. Thus, unlike in electromagnetism, where a single test charge can be used to determine the

field uniquely, a tidal force sensor or a "gradiometer" is the fundamental instrument in gravity which is capable of measuring its field, independent of platform motion. True acceleration measurement, in turn, requires removal of gravity noise which again calls for the use of a gravity gradiometer. It is therefore not surprising to find that instruments employed in most precision gravity experiments, such as torsion balances and Weber-type gravitational wave detectors, have actually been special types of gradiometers.

The acceleration difference along the direction j per unit separation along the direction i is defined to be the ij-component of the gravity gradient tensor $\vec{\vec{\Gamma}}$:

$$\Gamma_{ij}\ (\vec{r},t) \equiv -\frac{\partial^2 \phi(\vec{r},t)}{\partial x_i \partial x_j}\ , \qquad (1)$$

where $\phi(\vec{r},t)$ is the gravitational potential. A very weak gradient of 1 nm s^{-2} per m is equal to one Eötvös (E) unit, defined by

$$1\ E \equiv 10^{-9}\ s^{-2}. \qquad (2)$$

Many ground-based survey applications call for such high sensitivity. Geodesy application in space requires even higher sensitivity at the level of 10^{-4} E $Hz^{-1/2}$ [10]. The extreme weakness of gravitational interaction and the practical difficulties associated with balancing out the acceleration noise to a sufficient degree have limited the sensitivity of room temperature gradiometers to a level of $1 \sim 10$ E $Hz^{-1/2}$ [10]. Major improvements in sensitivity and stability are expected of the superconducting devices under development. It appears that a superconducting gravity gradiometer of a relatively compact design will have a sufficient sensitivity for space applications.

Besides possessing low thermal noise and low mechanical drift as direct consequences of a cryogenic temperature, the new gradiometer takes advantage of many exotic properties of superconductivity. Quantized magnetic flux is used as an extremely stable tool to achieve transducer action and common mode balance. Operating at liquid helium temperatures, SQUID (Superconducting QUantum Interference Device) serves as the most sensitive amplifier of today. Superconductivity can be used to make a nearly perfect electromagnetic shield and superfluid helium can provide a stable, gradient-free temperature environment. Flux quantization can further be used to accomplish stable levitation of proof masses against gravity in a terrestrial environment and to enhance the gradiometer sensitivity by means of a "superconducting negative spring" [11].

Two schemes (current-differencing and displacement-differencing) of superconducting gravity gradiometer have been demonstrated by Paik et al [12]. Error models were analyzed by Wang [13]. Mapoles [14] has extended the development of a displacement-differencing gravity gradiometer. In this work, we have chosen the current-differencing scheme. One advantageous feature of the current-differencing gradiometer is the remote coupling of the two differencing acceleration transducers independent of their separation and their respective orientations. Therefore, three in-line (or diagonal) component gradiometers can be combined together by mounting all three pairs of acceleration transducers on the six faces of a common cube, with the sensitive axes normal to the surfaces of the cube, to form a three-axis in-line component gravity gradiometer. Construction of cross (or off-diagonal) component gravity gradiometer is feasible by orienting the sensitive axes of the acceleration transducers perpendicular to the direction of the baseline. A tensor gravity gradiometer to measure all the six Γ_{ij} components has been

proposed [15] as a combination of the in-line and cross component gradiometers.

While developing a three-axis gradiometer for precision gravity experiments in Earth's orbit [16], we have completed, with our colleague, a prototype single-axis in-line component gradiometer. This instrument has been used to perform a laboratory null test of the gravitational inverse square law [17]. The details of this gradiometer development are described in Ref. 18 in which the theory of the gradiometer has been given a new formulation with generalization and more rigor than the preliminary analysis in Ref. 13. This paper (I) is a modified version of this new theoretical analysis with an extended error model of the instrument. Paper II presents the construction and test results of the gradiometer. Although we confine ourselves to the discussion of an in-line component gradiometer with a particular superconducting circuit chosen, the methods developed in these papers could easily be adapted to cross-component gradiometers and different superconducting circuits.

II. PRINCIPLE OF GRAVITY GRADIENT DETECTION

In this section we briefly review the basic principle of separating gravity signal from dynamical variables and set a basis for the error model developed in Section V. Let the instrument platform be moving with respect to an inertial frame with an instantaneous angular velocity $\vec{\Omega}(t)$ and linear acceleration $\vec{a}(t)$. Then, the accelerations of a proof mass observed in the two coordinate systems are related by the well-known equation [19]:

$$\left(\frac{d^2\vec{r}}{dt^2}\right)_{in} = \left(\frac{d^2\vec{r}}{dt^2}\right)_{p\ell} + \vec{\Omega} \times (\vec{\Omega} \times \vec{r}) + 2\vec{\Omega} \times \left(\frac{d\vec{r}}{dt}\right)_{p\ell} + \left(\frac{d\vec{\Omega}}{dt}\right)_{p\ell} \times \vec{r} + \vec{a} \quad .(3)$$

Here the subscripts in and pℓ represent the inertial and platform coordinate systems in which respective measurements are made. The second and third terms on the right-hand side are the centrifugal and the Coriolis accelerations, respectively. If $\phi(\vec{r},t)$ is the gravitational potential in the inertial frame, the resulting acceleration of the proof mass with respect to the moving platform is given by

$$\vec{g}'(\vec{r},t) \equiv \left(\frac{d^2\vec{r}}{dt^2}\right)_{p\ell}$$

$$= -\vec{\nabla}\,\phi(\vec{r},t) - \vec{\Omega} \times (\vec{\Omega} \times \vec{r}) - 2\vec{\Omega} \times \left(\frac{d\vec{r}}{dt}\right)_{p\ell} - \left(\frac{d\vec{\Omega}}{dt}\right)_{p\ell} \times \vec{r} - \vec{a}(t) \quad . \qquad (4)$$

The Coriolis term produces a force perpendicular to the velocity in the platform coordinates and therefore drops out when the proof mass is confined to move in a single direction. The quantity $\vec{g}'(\vec{r},t)$ is what is measured by an accelerometer or a gravimeter undergoing an acceleration.

It is clear from Eq. (4) that the linear acceleration term, $-\vec{a}(t)$, can be eliminated by a differential measurement over a spatial coordinate x_j:

$$\frac{\partial g_i'(\vec{r},t)}{\partial x_j} = -\frac{\partial^2 \phi(\vec{r},t)}{\partial x_i \partial x_j} - \frac{\partial}{\partial x_j}\left[\Omega_i(\vec{\Omega}\cdot\vec{r}) - \Omega^2 x_i\right]$$

$$- \sum_{k,\ell} \varepsilon_{ik\ell} \left(\frac{d\Omega_k}{dt}\right)_{p\ell} \frac{\partial x_\ell}{\partial x_j} . \qquad (5)$$

Substituting $\partial x_\ell/\partial x_j = \delta_{\ell j}$, and introducing the notations of Eq. (1) and

$$\Gamma_{ij}'(\vec{r},t) \equiv \frac{\partial g_i'(\vec{r},t)}{\partial x_j} , \qquad (6)$$

$$\alpha_k(t) \equiv \left(\frac{d\Omega_k}{dt}\right)_{p\ell} , \qquad (7)$$

one finds

$$\Gamma_{ij}'(\vec{r},t) = \Gamma_{ij}(\vec{r},t) - (\Omega_i\Omega_j - \Omega^2\delta_{ij}) + \sum_k \varepsilon_{ijk}\,\alpha_k(t) . \qquad (8)$$

Notice that the <u>angular</u> acceleration term is antisymmetric whereas the first two terms in Eq. (8) are symmetric tensors. Therefore, one can further drop $\vec{\alpha}(t)$ by symmetrization of Γ_{ij}':

$$\Gamma_{(ij)}'(\vec{r},t) \equiv \frac{1}{2}\left(\frac{\partial g_i'}{\partial x_j} + \frac{\partial g_j'}{\partial x_i}\right) = \Gamma_{ij}(\vec{r},t) - (\Omega_i\Omega_j - \Omega^2\delta_{ij}) . \qquad (9)$$

The centrifugal acceleration term can be taken out in principle by taking another spatial derivative: i.e., by means of a third order gravity gradiometer. In practice, one measures $\vec{\Omega}$ with the aid of gyroscopes and removes the effect of the centrifugal acceleration by actively stabilizing the platform or by compensating the induced error.

The <u>diagonal</u> component of the tensor, $\Gamma_{(ii)}' = \Gamma_{ii}'$, can be measured by detecting the relative acceleration along the in-line direction between <u>two</u>

proof masses, separated in the x_i direction. The off-diagonal components $\Gamma'_{(ij)}$ $(j \neq i)$, however, requires four proof masses because of the symmetrization. The relative accelerations in the cross directions in two pairs of accelerometers, which are separated in the x_i and x_j directions, respectively, can be added to yield $\Gamma'_{(ij)}$. Notice that one can instead subtract these two signals to determine the antisymmetric component:

$$\Gamma'_{[ij]}(\vec{r},t) \equiv \frac{1}{2}\left(\frac{\partial g'_i}{\partial x_j} - \frac{\partial g'_j}{\partial x_i}\right) = \sum_k \varepsilon_{ijk}\, \alpha_k(t) \ . \qquad (10)$$

The angular acceleration of the platform can be obtained by inverting this equation:

$$\alpha_k(t) = \varepsilon_{ijk}\, \Gamma'_{[ij]}(\vec{r},t) \ . \qquad (11)$$

A time integration of this vector then gives an alternative means of determining the angular velocity $\vec{\Omega}$.

A tensor gravity gradiometer with common mode readouts is therefore self-sufficient for true gravity detection [15]. On the other hand, the device can measure true linear and angular accelerations of a moving platform by removing gravity-induced errors. Equation (4) shows that the gravitational field $-\vec{\nabla}\phi$ remains as the fundamental error in linear acceleration measurement after removing dynamical error terms. The gravity gradiometer comes to the rescue. The gradient output $\vec{\vec{\Gamma}}$ can be integrated over a spatial coordinate to determine $-\vec{\nabla}\phi$. Therefore, a true accelerometer requires an aid from a gradiometer.

The symmetrization technique discussed above has been incorporated in the rotating gravity gradiometers [6, 7] whereas, in the floated gradiometer which has only two proof masses [8], the angular motion of the gradiometer is

attenuated by floating the proof masses in a liquid. In the rotating gradiometers, the common mode acceleration $\vec{g}'$ is further rejected by its frequency characteristic. The gradient $\vec{\vec{\Gamma}}$, being a tensor of rank 2, is modulated at the second harmonic of the rotation frequency whereas the acceleration $\vec{g}'$ is modulated at the fundamental frequency by its vector nature [6]. A side benefit of this heterodyne detection is the translation of signal bandwidth away from the 1/f noise region of the instrument in frequency space. The mechanical rotation, however, brings in a penalty: additional, dynamically induced errors. From Eq. (8) one can clearly see, for example, the devastating effect of the angular velocity error $\delta\Omega$, which now contributes a first order term $O(\Omega\delta\Omega)$ to the measurement.

For the prototype superconducting gravity gradiometer, we have chosen a non-rotating configuration. The extreme stability of the superconducting sensing circuit, combined with the low noise of the SQUID amplifier down to low signal frequencies, permits a very high degree of common mode rejection without rotation. For orbital applications, however, the superconducting gradiometer could be rotated to its advantage by spinning the entire satellite quietly.

The symmetric nature of Γ_{ij} has been used to construct a gravity gradiometer. Further, the trace of this tensor is constrained by the Poisson equation:

$$\sum_i \Gamma_{ii}\,(\vec{r},t) = -\nabla^2\phi(\vec{r},t) = -4\pi G\,\rho(\vec{r},t), \qquad (12)$$

which is a consequence of the inverse square law of the gravitational force. This leaves <u>five</u> independent components for the gravity gradient tensor Γ_{ij}. With a three-axis diagonal component gravity gradiometer, the validity of Eq.

(12) could be tested by summing the three outputs and comparing the result with the local mass density ρ. This experiment has been proposed as a precision null test of the inverse square law [20], and an early result of such an experiment has been reported [17]. In an actual experiment, the measured quantity is the trace of $\Gamma'_{(ij)}$:

$$\sum_i \Gamma'_{(ii)}(\vec{r},t) = - 4\pi G\, \rho(\vec{r},t) + 2\, \Omega^2(t). \qquad (13)$$

It is therefore important to suppress or separate out the centrifugal acceleration term carefully in such an experiment.

III. DYNAMICS OF THE SUPERCONDUCTING GRAVITY GRADIOMETER

The superconducting gravity gradiometer consists of a pair of superconducting acceleration transducers and a superconducting inductive load which is connected to a SQUID amplifier. The coupling between the transducers and the output load is provided by flux quantization.

The principle of one acceleration transducer element is first discussed and its equation of motion is then derived. Each transducer communicates to the rest of the superconducting circuit only through one current component that flows through the transducer. In a coupled circuit of a pair of transducers and a load, flux quantization imposes constraints to the superconducting circuit. For detection purposes, the currents at the load, rather than the current through the transducers, are the observable quantities at the output. The complete dynamical equations are then linearized and expressed in terms of these currents, the respective displacements of the proof masses, together with the applied common and differential acceleration signals [21]. Because the gradiometer is a differential accelerometer over a finite baseline, the gradiometer must reject common acceleration signals. The conditions for a common mode balance is derived. The parameters used to accomplish the balance are the persistent, but adjustable, currents stored in various superconducting loops. Further, a wideband common mode balance is shown to be possible by iteratively adjusting at least two current components. After balancing the common accelerations, only differential acceleration will be detected at the load. The transfer function of an applied differential acceleration to the corresponding current output at the load is derived.

Throughout the remainder of this paper, a variable with time or frequency dependency will be written explicitly as such functions, whereas the average values of these variables will be denoted by the same notation as the

function, but with the functional dependency deleted.

A. Principle of a Superconducting Acceleration Transducer

The principle of the superconducting acceleration transducer is illustrated schematically in Fig. 1. Analysis of this device as a resonant transducer for a gravitational wave antenna and as a sensitive accelerometer has been given previously in a different format [9]. A superconducting proof mass, which is suspended by spring and is confined to one linear degree of freedom, responds to an acceleration signal with a displacement relative to a sensing coil. The inductance of the coil is then modulated, due to the Meissner effect, by the superconducting plane of the proof mass. The coil is connected to an output inductor through a superconducting path and a quantized magnetic flux is stored in the superconducting loop formed by the sensing and output inductors. The current flow through the output inductor is modulated as a result of the inductance modulation of the sensing coil. The persistent current provides the stability of the transducer scale factor. A low noise SQUID amplifier is then used as a dc current-to-voltage power amplifier to produce a readout.

B. Analysis of a Single Acceleration Transducer

The transfer of mechanical energy to electrical energy is accomplished at the sensing coil. In order that the sensing coil converts a displacement to a current more linearly within a transducer, a symmetrical pair of "pancake" coils are utilized. The coils are located on the opposite faces of the proof mass and are connected in parallel (Fig. 2). Each having winding density n_L and area A_L, the coils are at mean distances of d_a and d_b from the respective superconducting planes of the proof mass. If the displacement of the proof

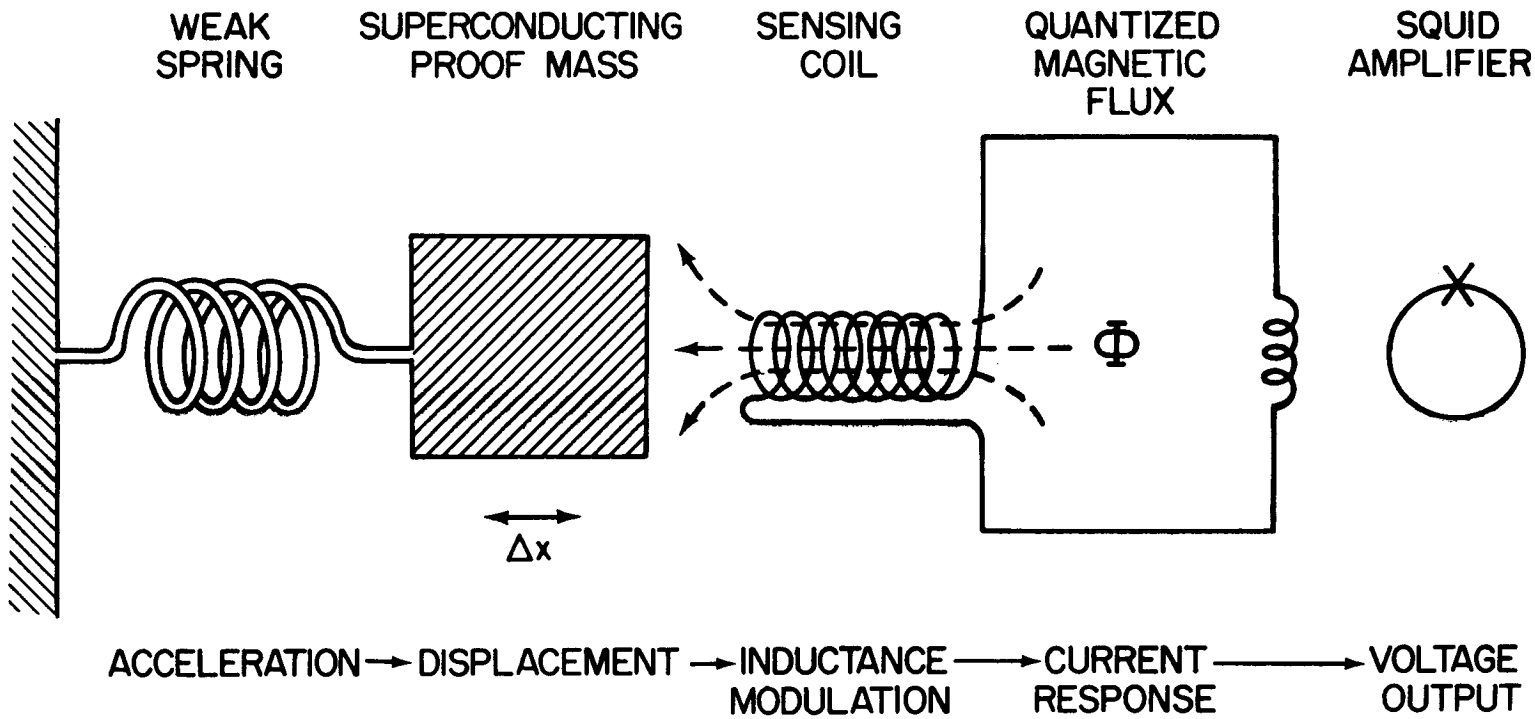

Fig. 1. Principle of the superconducting acceleration transducer.

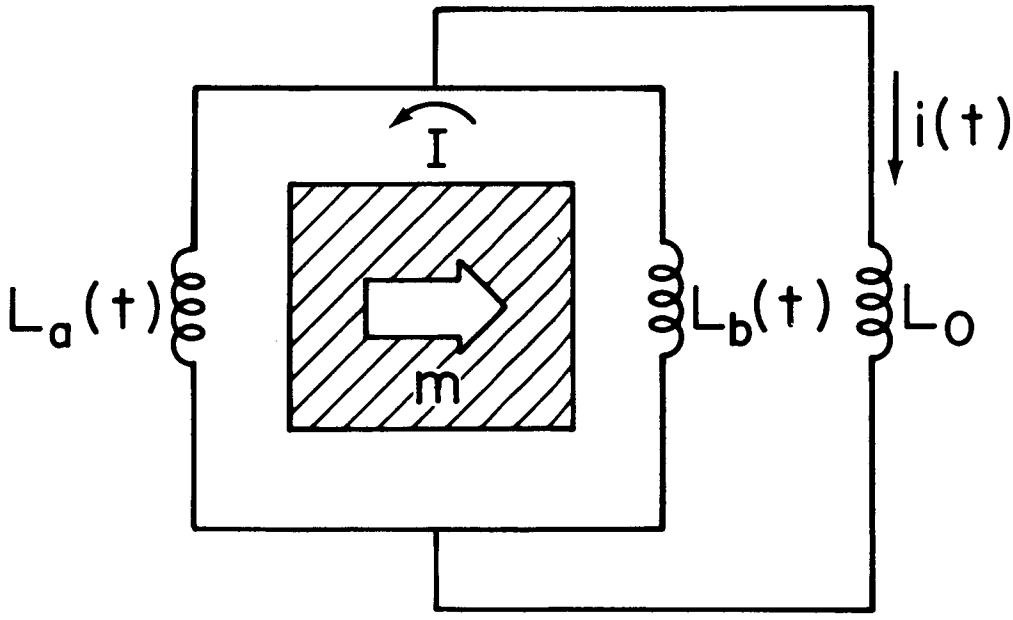

Fig. 2. Superconducting circuit and its current variables of a single acceleration transducer.

mass from its average position is x(t), the inductances of the coils are given by

$$L_a(t) = \Lambda\ [d_a + x(t)] = L_a + \Lambda\ x(t), \tag{14a}$$

$$L_b(t) = \Lambda\ [d_b - x(t)] = L_b - \Lambda\ x(t). \tag{14b}$$

Here

$$\Lambda \equiv \mu_o\ n_L^2\ A_L, \tag{15}$$

where μ_o is the permeability in free space and

$$L_a \equiv \langle L_a(t) \rangle \quad , \quad L_b \equiv \langle L_b(t) \rangle, \tag{16}$$

as was noted earlier concerning notation.

Two current components are needed to characterize the electromagnetic state of the two sensing coils. One obvious choice of variables [9, 13] is the currents $I_a(t)$ and $I_b(t)$ which flow through each of the two coils, so that the electromagnetic energy in the two coils is

$$V_{EM} = \frac{1}{2}\ L_a(t)\ I_a(t)^2 + \frac{1}{2}\ L_b(t)\ I_b(t)^2. \tag{17}$$

However, in order to make the analysis simpler, a different choice [18] of the two current variables can be made with the aim that the expression for the electromagnetic energy has as simple a denominator as possible. Such a way of choosing variables is a classical analog of the renormalization procedure in

quantum field theory.

Before making the choice, we make two observations. The first observation is that the series inductance of the sensing coils is a constant [9]:

$$L_s(t) \equiv L_a(t) + L_b(t) = L_a + L_b = L_s. \tag{18}$$

Consequently, the current I through the superconducting loop of these two inductors in series is also a constant because the trapped flux Φ_{ab} in this loop is quantized. The second observation is that the parallel combination of the two sensing coils has a constant denominator in the expression for its inductance:

$$L_p(t) \equiv \frac{L_a(t)\, L_b(t)}{L_a(t) + L_b(t)} = \frac{1}{L_a + L_b} [L_a L_b - (L_a - L_b)\, \Lambda\, x(t) - \Lambda^2 x^2(t)]. \tag{19}$$

In fact, even the numerator of this parallel inductance will also be a constant up to the first order if the mean spacings d_a and d_b are matched so as to make $L_a \simeq L_b$. The nonlinearity of the inductance modulation is exhibited by the second order term in Eq. (19).

Expressed in terms of one parameter Φ_{ab} and one current variable i(t), which flows through the parallel combination of $L_a(t)$ and $L_b(t)$, the electromagnetic energy has a <u>constant denominator</u> and has thus acquired a "renormalized" form:

$$V_{EM} = \frac{1}{2} \frac{\Phi_{ab}^2}{L_a + L_b} + \frac{1}{2} L_p(t)\, i^2(t). \tag{20}$$

It is straightforward to show that the expressions in Eqs. (17) and (20) are equivalent to each other [18].

The only variable i(t), once the parameter I or Φ_{ab} is fixed, possesses all the dynamical information in the electromagnetic system of the transducer. As the inductances $L_a(t)$ and $L_b(t)$ are modulated by the displacement of the proof mass, the current i(t) must always split between the two inductors according to the inverse ratio of the respective inductances in order to produce equal and opposite magnetic flux contributions to the superconducting loop formed by the series inductor $L_a + L_b$. The net currents $I_a(t)$ and $I_b(t)$ through $L_a(t)$ and $L_b(t)$ are therefore the following linear combinations of I and i(t):

$$I_a(t) = \frac{L_b(t)}{L_a + L_b}\, i(t) - I, \tag{21a}$$

$$I_b(t) = \frac{L_a(t)}{L_a + L_b}\, i(t) + I. \tag{21b}$$

The force due to magnetic field pressure on the proof mass is given by

$$F_{EM} = -\frac{\partial}{\partial x}\left[\frac{\Phi_a^2(t)}{2\,L_a(t)} + \frac{\Phi_b^2(t)}{2\,L_b(t)}\right]\Big|_{\Phi_a,\Phi_b}$$

$$= \frac{\Lambda}{2}\left[I_a^2(t) - I_b^2(t)\right], \tag{22}$$

where $\Phi_a(t)$ and $\Phi_b(t)$ denote magnetic fluxes in $L_a(t)$ and $L_b(t)$, respectively. In terms of I and i(t), this force can be rewritten as

$$F_{EM} = -\Lambda\left[I + \frac{1}{2}\,\frac{L_a(t) - L_b(t)}{L_a + L_b}\, i(t)\right] i(t). \tag{23}$$

The total force acting on the proof mass consists of this magnetic force together with a restoring force of the mechanical spring suspension of the proof mass and any externally applied force, f(t), on the proof mass relative to the platform of the sensing coils. We will ignore the effects of damping term for the time being. When the proof mass m is approximated as a point mass located at its center of mass $\vec{r}$, the external force becomes

$$f(t) = m\,\hat{n} \cdot \vec{g}'(\vec{r},t) \ , \tag{24}$$

where $\hat{n}$ is the unit vector along the direction of the sensitive axis, and $\vec{g}'(\vec{r},t)$ is the specific force given by Eq. (4). The equation of motion for the proof mass in the platform frame can now be written as

$$\ddot{x}'(t) + \omega_M^2\, x'(t) + \frac{A}{m}\left[I + \frac{1}{2}\,\frac{L_a(t) - L_b(t)}{L_a + L_b}\, i(t)\right] i(t) = \hat{n} \cdot \vec{g}'(\vec{r},t) \ , \tag{25}$$

where ω_M is the angular resonance frequency of the mechanical spring. An alternative derivation of this equation, in which an electromechanical Lagrangian approach is used for the superconducting transducer, is found in Ref. 18.

The dc component of Eq. (25) defines the equilibrium position, x_o, of the proof mass. This position is shifted from the relaxed position of the mechanical spring by Earth's gravity, $\vec{g}_E$, and by a dc magnetic force. Substituting

$$x'(t) \equiv x_o + x(t), \tag{26a}$$

$$\vec{g}'(\vec{r},t) \equiv \vec{g}_E(\vec{r}) + \vec{g}'_p(\vec{r},t) \tag{26b}$$

into Eq. (25), we find

$$x_o = - \frac{g_E \cos \theta_n}{\omega_M^2} - \frac{\Lambda}{m\omega_M^2} \left(I + \frac{1}{2} \frac{L_a - L_b}{L_a + L_b} i \right) i \ , \qquad (27)$$

in the general case where $i \equiv \langle i(t) \rangle \neq 0$. Here θ_n is the angle that the sensitive axis makes with the upward vertical. The local vertical is defined by Earth's gravity vector which is found from Eq. (4) as

$$\vec{g}_E(\vec{r}) = - \vec{\nabla} \phi_E(\vec{r}) - \vec{\Omega}_E \times [\vec{\Omega}_E \times (\vec{R}_E + \vec{r})] \ , \qquad (28)$$

where $\phi_E(\vec{r})$, $\vec{\Omega}_E$ and $\vec{R}_E$ are, respectively, Earth's gravitational potential, spin angular velocity, and the geocentric position vector of the coordinate origin.

The linearized equation of motion for the ac part, after Fourier transformation, can be readily shown as

$$\left(-\omega^2 + \omega_M^2 + \frac{\Lambda^2 i^2}{mL_s} \right) x(\omega) + \frac{\Lambda I'}{m} i(\omega) = g(\omega) \ , \qquad (29)$$

where $g(\omega)$ is the Fourier transform of

$$g(t) \equiv \hat{n} \cdot \vec{g}_p(\vec{r},t) \qquad (30)$$

and

$$I' \equiv I + \frac{L_a - L_b}{L_a + L_b} i. \qquad (31)$$

There are two independent superconducting loops in the circuit. The flux

quantization condition in the loop $L_a(t) + L_b(t)$ has already been used in representing I as a constant. An additional constraint in the dynamical equation comes from the flux quantization condition in the loop $L_b(t) + L_o$:

$$L_b(t)\ I_b(t) + L_o i(t) = \Phi_{bo}. \tag{32}$$

The first order equation becomes, after Fourier transformation,

$$\Lambda I' x(\omega) = (L_o + L_p)\ i(\omega). \tag{33}$$

Simultaneous equations (29) and (33) determine the dynamics of a single transducer completely. In particular, the acceleration-to-current transfer function can be shown to be

$$H_{gi}(\omega) = \frac{1}{\omega_o^2 - \omega^2} \frac{\Lambda I'}{L_o + L_p}. \tag{34}$$

Here, ω_o is the resulting angular resonance frequency of the transducer due to the addition of spring constant to $m\omega_M^2$ by the superconducting circuit:

$$\omega_o^2 \equiv \omega_M^2 + \frac{\Lambda^2 i^2}{mL_s} + \frac{\Lambda^2 I'^2}{m(L_o + L_p)}. \tag{35}$$

C. Dynamical Equations for the Gradiometer

The gradiometer, shown in Fig. 3, consists of a pair of the above acceleration tranducers and a superconducting inductive load. The coupling among these elements is through flux quantization in the superconducting circuit which has four independent superconducting loops.

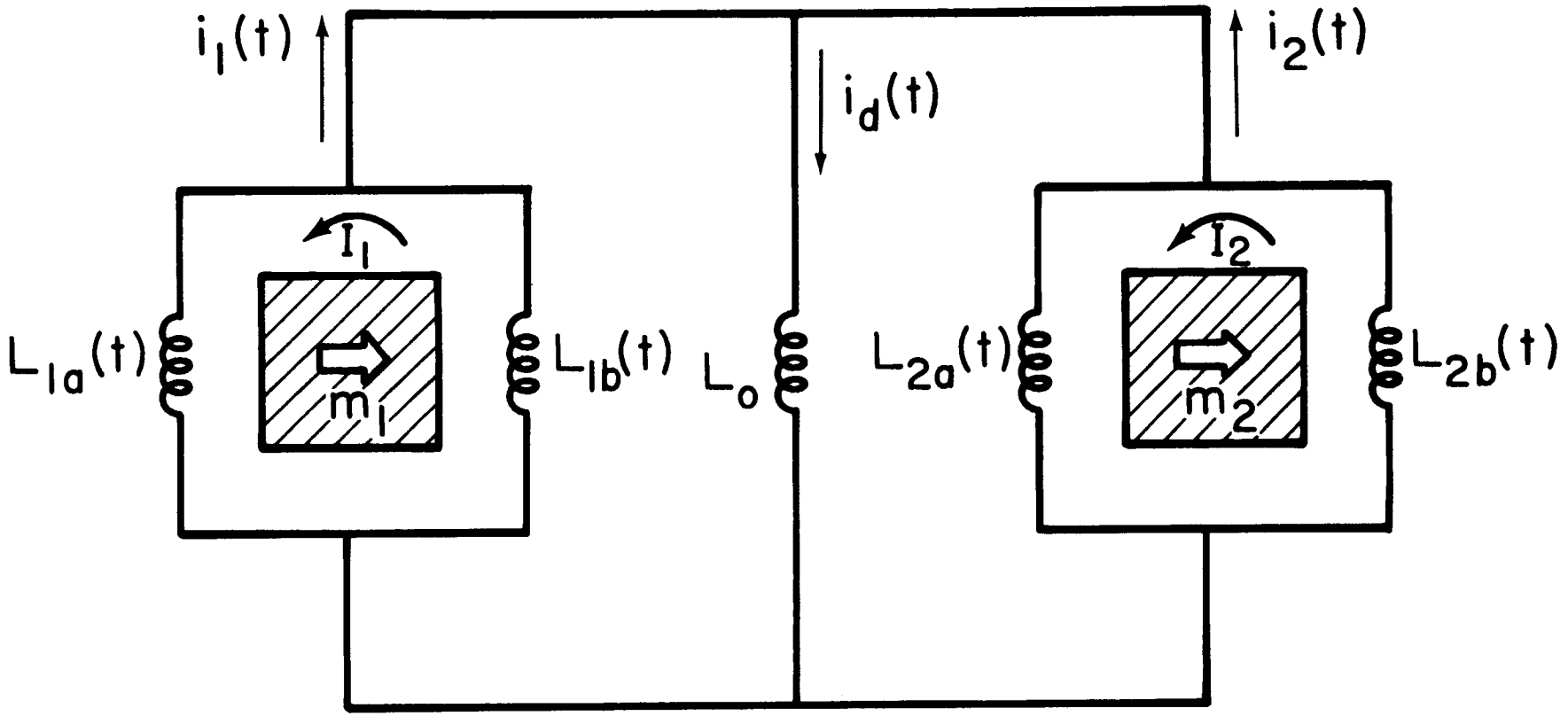

Fig. 3. Superconducting circuit of the current-differencing gradiometer.

The dynamical equations for each transducer is analogous to Eqs. (29) and (33) for a single accelerometer. An additional subscript,

$$k = 1 \text{ or } 2, \tag{36}$$

is now used for the respective variables and parameters to distinguish between the two transducers. With this subscript, the linearized equations of motion for the proof masses in the transducers, being similar to Eq. (29), are written as

$$\left(-\omega^2 + \omega_{kM}^2 + \frac{\Lambda^2 i_k^2}{m_k L_{ks}}\right) x_k(\omega) + \frac{\Lambda I_k'}{m_k} i_k(\omega) = g_k(\omega) \ . \tag{37}$$

Here, the geometries of the sensing coils are again assumed to be identical so that they can be represented by a single parameter Λ defined by Eq. (15). Also, the two flux quantization constraints in the superconducting loops $L_{ka} + L_{kb}$ have again been used in deriving Eq. (37). Two more constraints, similar to Eq. (33), are obtained by using flux quantization conditions in two other independent superconducting loops such as $L_{kb}(t) + L_o$. However, a generalization from Eq. (33) is needed here because the current through L_o is now the sum of the current outputs from each transducer. The linearized constraints are therefore given by

$$\Lambda \ I_k' \ x_k(\omega) = L_{kp} \ i_k(\omega) + L_o \ [i_1(\omega) + i_2(\omega)] \ . \tag{38}$$

Notice that these two equations are coupled through $i_1(\omega)$ and $i_2(\omega)$.

The dynamics of the gradiometer, governed by the four coupled equations (37) and (38) in the four variables $x_k(\omega)$ and $i_k(\omega)$, has two degrees of

freedom. Each of the two transducers couple to the rest of the circuit through one single current signal, $i_1(\omega)$ or $i_2(\omega)$. Depending on the signature of the applied acceleration components, these current modulations can add or subtract at the output inductor L_o. It is therefore convenient to use a new set of current variables $i_d(\omega)$ and $i_c(\omega)$ defined by the sum and half of the difference of the two transducer currents. In terms of $i_d(\omega)$ and $i_c(\omega)$, the transducer currents $i_1(\omega)$ and $i_2(\omega)$ can be expressed as

$$i_k(\omega) = \frac{1}{2}\, i_d(\omega) + (-1)^k\, i_c(\omega). \tag{39}$$

Likewise, the applied accelerations $g_1(t)$ and $g_2(t)$ at the proof masses m_1 and m_2 can be expressed in terms of their differential and common accelerations, $g_d(\omega)$ and $g_c(\omega)$, as

$$g_k(\omega) = (-1)^k\, \frac{1}{2}\, g_d(\omega) + g_c(\omega). \tag{40}$$

Notice that $i_d(\omega)$ is the actual current flowing through L_o and detected by the SQUID.

With the change of variables in Eqs. (39) and (40), the dynamical equations (37) and (38) become

$$\left(-\omega^2 + \omega_{kM}^2 + \frac{\Lambda^2 i_k^2}{m_k L_{ks}}\right) x_k(\omega) + \frac{\Lambda I_k'}{m_k}\, \frac{1}{2}\, i_d(\omega) + (-1)^k\, \frac{\Lambda I_k'}{m_k}\, i_c(\omega)$$

$$= (-1)^k\, \frac{1}{2}\, g_d(\omega) + g_c(\omega), \tag{41}$$

$$x_k(\omega) = \frac{L_{kp} + 2L_o}{\Lambda I_k'}\, \frac{1}{2}\, i_d(\omega) + (-1)^k\, \frac{L_{kp}}{\Lambda I_k'}\, i_c(\omega). \tag{42}$$

Upon eliminating the displacement coordinates, we obtain

$$(-\omega^2 + \omega_{kd}^2)\,\frac{L_{kp} + 2L_o}{\Lambda I_k'}\,\frac{1}{2}\,i_d(\omega) + (-1)^k\,(-\omega^2 + \omega_{kc}^2)\,\frac{L_{kp}}{\Lambda I_k'}\,i_c(\omega)$$

$$= (-1)^k\,\frac{1}{2}\,g_d(\omega) + g_c(\omega) = g_k(\omega), \tag{43}$$

where

$$\omega_{kc}^2 \equiv \omega_{kM}^2 + \frac{1}{m_k}\left(\frac{\Lambda^2 i_k^2}{L_{ks}} + \frac{\Lambda^2 I_k'^2}{L_{kp}}\right), \tag{44a}$$

$$\omega_{kd}^2 \equiv \omega_{kM}^2 + \frac{1}{m_k}\left(\frac{\Lambda^2 i_k^2}{L_{ks}} + \frac{\Lambda^2 I_k'^2}{L_{kp} + 2L_o}\right). \tag{44a}$$

Solving Eq. (43) for the signal current, we find

$$i_d(\omega) = H_{gi}^d(\omega)\; g_d(\omega) + H_{gi}^c(\omega)\; g_c(\omega), \tag{45}$$

where $H_{gi}^d(\omega)$ and $H_{gi}^c(\omega)$ are the transfer functions from $g_d(\omega)$ and $g_c(\omega)$, respectively, to $i_d(\omega)$. These transfer functions of the gradiometer are given by

$$H_{gi}^d(\omega) = \frac{\dfrac{1}{\omega_{2c}^2 - \omega^2}\,\dfrac{\Lambda I_2'}{L_{2p}} + \dfrac{1}{\omega_{1c}^2 - \omega^2}\,\dfrac{-\Lambda I_1'}{L_{1p}}}{\dfrac{\omega_{2d}^2 - \omega^2}{\omega_{2c}^2 - \omega^2}\,\dfrac{2L_o + L_{2p}}{L_{2p}} + \dfrac{\omega_{1d}^2 - \omega^2}{\omega_{1c}^2 - \omega^2}\,\dfrac{2L_o + L_{1p}}{L_{1p}}}, \tag{46a}$$

$$H_{gi}^c(\omega) = \frac{2\left(\dfrac{1}{\omega_{2c}^2 - \omega^2}\,\dfrac{\Lambda I_2'}{L_{2p}} - \dfrac{1}{\omega_{1c}^2 - \omega^2}\,\dfrac{-\Lambda I_1'}{L_{1p}}\right)}{\dfrac{\omega_{2d}^2 - \omega^2}{\omega_{2c}^2 - \omega^2}\,\dfrac{2L_o + L_{2p}}{L_{2p}} + \dfrac{\omega_{1d}^2 - \omega^2}{\omega_{1c}^2 - \omega^2}\,\dfrac{2L_o + L_{1p}}{L_{1p}}}. \tag{46b}$$

The four parameters ω_{kd} and ω_{kc} are, in general, not the two resonances of the gradiometer. Nevertheless, comparing the expressions for these parameters with Eqs. (34) and (35) suggests intuitive meaning to these nonobservables. Thus, ω_{kc} can represent the angular resonance frequencies that the two transducers would separately have if they were each connected to a short-circuited load. A short-circuited load arises in these models because, when $i_d(\omega) = 0$ in the gradiometer circuit, the two transducers are driving the current $i_c(\omega)$ in a push-pull manner, contributing zero impedance to each other. Likewise, ω_{kd} can represent the angular resonance frequencies that the two transducers would separately have if they were each loaded with an inductance of $2L_o$ but were otherwise decoupled from each other. The appearance of $2L_o$ here is due to the equal contributions of currents $\frac{1}{2} i_d(\omega)$ to the signal at L_o. Thus, under the restriction $i_c(\omega) = 0$, the flux modulation produced by each transducer at L_o as seen by the transducer itself is doubled by the presence of the other transducer. The transfer functions of these separated model accelerometers are given from Eq. (43) as

$$\frac{\partial i_d}{\partial g_k}\Big|_{i_c} = \frac{(-1)^k \Lambda I_k'}{2L_o + L_{kp}} \frac{1}{\omega_{kd}^2 - \omega^2}, \tag{47a}$$

$$\frac{\partial i_c}{\partial g_k}\Big|_{i_d} = \frac{(-1)^k \Lambda I_k'}{L_{kp}} \frac{1}{\omega_{kc}^2 - \omega^2}. \tag{47b}$$

D. Common Mode Balance and Gradiometer Transfer Function

For operation as a gradiometer in the presence of common accelerations, the transducers need to be tuned such that $H_{gi}^c(\omega) = 0$. No common acceleration signal will then appear at the output load L_o, and the coupled acceleration transducers are said to operate in a "gradiometer mode". On the other hand,

parameters can be chosen such that $H^d_{gi}(\omega)$ vanishes instead. Then, the output will respond only to common accelerations and the system is said to operate in an "accelerometer mode". The accelerometer mode operation is a powerful means of obtaining a precise calibration of the gradiometer. A detailed discussion of the accelerometer mode is found in Section IVB of Paper II. From Eq. (46b), the common mode balance is obtained when

$$\frac{-\Lambda I_1'}{(\omega_{1c}^2 - \omega^2)\, L_{1p}} = \frac{\Lambda I_2'}{(\omega_{2c}^2 - \omega^2)\, L_{2p}} . \tag{48}$$

This balance condition can be satisfied at any single frequency by adjusting only one persistent current parameter. Balancing over a small frequency range near dc appears sufficient for normal low-frequency use of the gradiometer in which $\omega \ll \omega_{1c}, \omega_{2c}$. In the terrestial environment, however, the environmental vibrations occur in a wideband and are very large compared with the extremely weak gravitational signals. A wideband balance will help to immunize the gradiometer against such environmental vibrations.

The four current components, I_1, I_2, i_1, and i_2, do provide more than sufficient degrees of freedom to tune for wideband balance. In principle, Eq. (48) becomes an identity if

$$\omega_{1c} = \omega_{2c} \tag{49a}$$

and

$$-\frac{\Lambda\, I_1'}{L_{1p}} = \frac{\Lambda\, I_2'}{L_{2p}} \tag{49b}$$

are simultaneously satisfied. However, direct matching of ω_{kc} is not

practical because these equivalent resonances are observable only when the output load is shorted and when the two transducers are also decoupled mechanically [18]. In the experiment, a wideband balance can be achieved instead by iterating the balance at two frequencies. Tuning I_1 or I_2 to balance out an applied common acceleration at a high frequency ($\omega >> \omega_{1c}, \omega_{2c}$) will achieve the condition (49b). This adjustment is followed by tuning of i_1 or i_2 for balance at a low frequency ($\omega << \omega_{1c}, \omega_{2c}$), yielding

$$-\frac{1}{\omega_{1c}^2}\frac{\Lambda I_1'}{L_{1p}} = \frac{1}{\omega_{2c}^2}\frac{\Lambda I_2'}{L_{2p}} . \tag{49c}$$

The latter operation will, in general, affect the previous balance (49b), and iteration between the two balance procedures is needed. When the conditions (49b) and (49c) are both satisfied, the condition (49a) follows. This frequency-independent balance has been applied in the experiment and is reported in Paper II.

Upon substitution of Eq. (48) into Eq. (46a), $H_{gi}^d(\omega)$ assumes a simple form:

$$[H_{gi}^d(\omega)]^{-1} = (\omega_{1d}^2 - \omega^2)\frac{L_o + \frac{1}{2}L_{1p}}{-\Lambda I_1'} + (\omega_{2d}^2 - \omega^2)\frac{L_o + \frac{1}{2}L_{2p}}{\Lambda I_2'} . \tag{50}$$

Notice that the transfer function of a balanced gradiometer becomes the harmonic mean of the transfer functions of the two separated model accelerometers, given by Eq. (47a).

When the common mode balance is not precise, $H_{gi}^c(\omega) \neq 0$ constitutes an error coefficient. This error, which will be discussed in Section V, is obtained from Eqs. (46) as

$$H_{gi}^{c}(\omega) \simeq H_{gi}^{d}(\omega) \frac{\frac{1}{\omega_{2c}^2 - \omega^2} \frac{\Lambda I_2'}{L_{2p}} - \frac{1}{\omega_{1c}^2 - \omega^2} \frac{-\Lambda I_1'}{L_{1p}}}{\frac{1}{2}\left(\frac{1}{\omega_{2c}^2 - \omega^2} \frac{\Lambda I_2'}{L_{2p}} + \frac{1}{\omega_{1c}^2 - \omega^2} \frac{-\Lambda I_1'}{L_{1p}}\right)} \quad . \qquad (51)$$

In the foregoing analysis, the transducer has been approximated as a linear system. The dynamical equations (25) and (32), however, are nonlinear in nature so that the response current $i_d(\omega)$ must contain nonlinear terms in general, in addition to the linear terms shown in Eq. (45). These nonlinear terms may not drop out even when $H_{gi}^{c}(\omega) = 0$. The scale factor nonlinearity therefore constitutes an important error source, which will be discussed in Section V of this paper and in Appendix B of Paper II.

E. Equivalent Accelerometer Representation

With two coupled acceleration transducers in the gradiometer, only the differential acceleration is the measured signal at L_o. The common acceleration drops out upon balance. Therefore, a convenient representation of the gradiometer is a single (differential) accelerometer which converts a differential acceleration into a signal current. Such a representation involves identification of the gradiometer transfer function with the parameters of a single accelerometer, as discussed in Section IIIB. These parameters include a resonance frequency, a mass and the parameters of a superconducting circuit.

The two normal mode resonance frequencies of the gradiometer are some weighted average of the parameters ω_{1c} and ω_{2c} for the common mode and also some other weighted average of ω_{1d} and ω_{2d} for the differential mode. In the particular case of wideband balance, ω_{1c} and ω_{2c} are equal to each other and hence equal to the common mode angular resonance frequency, denoted by ω_c. The differential mode angular resonance frequency, denoted by ω_o, is then defined from the singularity of $H_{gi}^{d}(\omega)$ in Eq. (50). In practice, the gradiometer need only be balanced at a limited frequency band of the signal. Then,

Eq. (50) is only valid in this limited frequency band. Therefore, the exact differential mode resonance is determined from the singularity of $H^d_{gi}(\omega)$ in the more general equation (46a). Yet, as far as signal transduction within the limited signal frequency band is concerned, we can still use Eq. (50) to define ω_o.

By defining equivalent circuit parameters to satisfy

$$\frac{L_o + L_p}{I'} \equiv \frac{L_o + \frac{1}{2} L_{1p}}{-I'_1} + \frac{L_o + \frac{1}{2} L_{2p}}{I'_2} , \tag{52}$$

we can convert Eq. (50) into the form of Eq. (34):

$$H^d_{gi}(\omega) \equiv \frac{\Lambda I'}{L_o + L_p} \frac{1}{\omega_o^2 - \omega^2} , \tag{53}$$

where the effective resonance frequency, ω_o, is related to ω^2_{kd} by

$$\frac{L_o + L_p}{I'} \omega_o^2 \equiv \frac{L_o + \frac{1}{2} L_{1p}}{-I'_1} \omega^2_{1d} + \frac{L_o + \frac{1}{2} L_{2p}}{I'_2} \omega^2_{2d} . \tag{54}$$

While there is freedom in defining the individual circuit parameters which appear on the lefthand side of Eq. (52), one natural choice is to identify L_o with the load inductance and L_p with the output inductance of the superconducting circuit:

$$\frac{1}{L_p} \equiv \frac{1}{L_{1p}} + \frac{1}{L_{2p}} . \tag{55}$$

Then, the current parameter I' is defined by Eq. (52). With the aid of Eqs. (49b) and (55), this definition of I' in Eq. (52) simplifies to

$$\frac{1}{I'} \equiv \frac{1}{-I_1'} + \frac{1}{I_2'} , \tag{56}$$

under wideband balance condition.

The transfer function in Eq. (53) has only characterized the overall signal transduction of the gradiometer. The intrinsic noise of the gradiometer will be given in Section IV in terms of Brownian motion noise and amplifier noise. For a single spring-mass system, the Brownian motion depends on the mass and the fluctuating force of the spring. Therefore, once the effective mass in the equivalent accelerometer representation is determined, the Brownian motion of the two coupled acceleration transducers in the differential mode can be derived using this equivalent single spring-mass model. This effective mass requires a unique definition in order to give the correct Brownian motion noise of the gradiometer and must therefore be derived from the dynamics of the gradiometer.

Dynamically, the gradiometer consists of two coupled masses connected to the platform and to each other by three springs. Thus, the homogeneous equations of motion of the two proof masses are obtained by eliminating $i_k(\omega)$ from Eqs. (37) and (38):

$$\omega^2 m_k \, x_k(\omega) = K_k x_k(\omega) + K_{12} x_{3-k}(\omega), \tag{57}$$

where the three spring constants K_k and K_{12} are given by

$$K_k \equiv m_k \, \omega_{kM}^2 + \frac{\Lambda^2 i_k^2}{L_{ks}} + \frac{(\Lambda I_k')^2 (L_o + L_{kp})}{(L_o + L_p)(L_{1p} + L_{2p})} , \tag{58}$$

$$K_{12} \equiv \frac{(-\Lambda I_1')(\Lambda I_2') L_o}{(L_o + L_p)(L_{1p} + L_{2p})} . \tag{59}$$

Now, we need to find out what displacement variable, $x_d(\omega)$, cause the signal current $i_d(\omega)$. Thus, we break up the signal transduction into two intermediate steps: $g_d(\omega)$ to $x_d(\omega)$ and then $x_d(\omega)$ to $i_d(\omega)$. From Eqs. (41) and (42), we obtain

$$(-\omega^2 + \omega_o^2)\, x_d(\omega) = g_d(\omega), \tag{60}$$

$$i_d(\omega) = \frac{\Lambda I'}{L_o + L_p}\, x_d(\omega), \tag{61}$$

where

$$x_d(\omega) \equiv \frac{L_p}{I'}\left[\frac{I_2'}{L_{2p}}\, x_2(\omega) - \frac{-I_1'}{L_{1p}}\, x_1(\omega)\right]. \tag{62}$$

The effective mass is therefore the inertia for the coupled spring mass system of Eqs. (57) - (59) towards the motion $x_d(\omega)$ of Eq. (62).

We next note that a simple scaling of the two separate displacement variables,

$$x_k'(\omega) \equiv \frac{L_p}{I'}\,\frac{(-1)^k I_k'}{L_{kp}}\, x_k(\omega), \tag{63}$$

simplifies $x_d(\omega)$ into the form:

$$x_d(\omega) \equiv x_2'(\omega) - x_1'(\omega). \tag{64}$$

The corresponding scaling required for the masses and spring constants are

$$m_k' \equiv \left(\frac{x_k}{x_k'}\right)^2 m_k, \tag{65a}$$

$$K'_k \equiv \left(\frac{x_k}{x'_k}\right)^2 K_k, \tag{65b}$$

$$K'_{12} \equiv \frac{x_1 x_2}{x'_1 x'_2} K_{12}, \tag{65c}$$

because, under these scaling, the dynamical equation (60) is invariant in form and both the kinetic and potential energies (within the frequency range of common mode balance) remain unchanged.

Now, the effective mass corresponding to $x_d(\omega)$ of Eq. (64) is just the reduced mass of m'_1 and m'_2. By using Eqs. (63) and (65a), this effective mass, denoted by m, can be shown to satisfy a simple formula:

$$\frac{L_p^2}{I'^2 m} \equiv \frac{L_{1p}^2}{I_1'^2 m_1} + \frac{L_{2p}^2}{I_2'^2 m_2} . \tag{66}$$

In Section IVA, the effective mass defined here will be used in conjunction with the equivalent accelerometer representation for finding the Brownian motion noise of the transducer.

IV. NOISE AND OPTIMIZATION

In the light of the equivalent accelerometer model given in Section IIIE, the fundamental noise terms of the gradiometer will be derived by treating the gradiometer as a single accelerometer. In this section, we introduce damping and consider its effects.

A. Transducer Brownian Motion Noise

The fundamental noise source of a spring-mass system at a temperature T is the Brownian motion of the harmonic oscillator at that temperature. The force of the spring on the proof mass undergoes random fluctuations. The spectral density of such force fluctuations at the resonance frequency ω_o of the oscillator is related, by the Fluctuation-Dissipation Theorem, to the damping of the oscillator at resonance.

In applying the Fluctuation-Dissipation Theorem, emphasis is made here that measurement of relaxation time $\tau(\omega_o)$ or quality factor $Q(\omega_o) \equiv \omega_o\tau(\omega_o)$ gives information on the force fluctuations only at ω_o. The Langevin equation is a modification of the equation of motion in Section III by including a damping term and an acceleration noise $g_n^T(\omega)$ term:

$$\left[-\omega^2 + \frac{j\,\omega}{\tau(\omega_o)} + \omega_o^2\right] x(\omega) = g_n^T(\omega). \tag{67}$$

Thus the energy of the oscillator at a temperature T:

$$m\,\omega_o^2\,\langle x^2(t)\rangle = k_B\,T, \tag{68}$$

where

$$\langle x^2(t)\rangle = \int_0^\infty x(\omega)\, x^*(\omega)\, d\omega, \tag{69}$$

is dominated by its spectral density at resonance. Use of Eqs. (67) - (69) gives the Nyquist formula:

$$S_g^T(\omega_o) = \frac{2}{\pi} k_B T \frac{1}{m\tau(\omega_o)}, \tag{70}$$

where $S_g^T(\omega_o)$ is the spectral density [22] of the acceleration noise g_n^T at ω_o.

The force or acceleration fluctuations at a signal frequency $\omega << \omega_o$ is in general <u>different</u> from that at ω_o because the noise could have a complicated frequency dependence which is governed by the nature of the loss mechanisms in the spring. The noise at ω due to force fluctuations in the spring is obtained from Eq. (70) with $\tau(\omega_o)$ replaced by $\tau(\omega)$:

$$S_g^T(\omega) = \frac{2}{\pi} k_B T \frac{1}{m\tau(\omega)}. \tag{71}$$

A direct measurement of $\tau(\omega)$ requires shifting the resonance frequency from ω_o to ω. In principle, one can increase the mass m or use a "negative spring" [11] so that the new spring-mass system indeed resonates at ω and therefore the Q factor of this new system can be measured. From a knowledge of the new mass used or of the loss in the negative spring, the dissipation in the original spring can be determined.

The Q factor of the accelerometer depends on both the mechanical and the electrical parameters because the electromechanical spring of the accelerometer has contributions from a mechanical spring and two electromagnetic springs, in the ratio given by the three terms in Eq. (35), for the total spring constant and hence for the stored ac energy at ω_o. The power loss in

each of these constituent springs is then proportional to this ratio of stored ac energies in these springs divided by a certain relaxation time at ω_o. Therefore, the following relationship for the relaxation times results from the obvious observation that, at ω_o, the total ac power loss is the sum of the power losses in the respective springs:

$$\frac{1}{\tau(\omega_o)} = \frac{1 - \gamma - \beta}{\tau_M(\omega_o)} + \frac{\gamma}{\tau_i(\omega_o)} + \frac{\beta}{\tau_{I'}(\omega_o)} . \tag{72}$$

Here $\tau_M(\omega_o)$, $\tau_i(\omega_o)$ and $\tau_{I'}(\omega_o)$ are the relaxation times that each spring would have if it is separately resonated at ω_o, and γ and β are the transducer energy coupling coefficients via i and I' defined by

$$\gamma \equiv \frac{\Lambda^2 i^2}{m\omega_o^2 L_s} , \tag{73a}$$

$$\beta \equiv \frac{\Lambda^2 I'^2}{m\omega_o^2 (L_o + L_p)} . \tag{73b}$$

In order to reduce dissipation in all the constituent springs, choice of material and geometry, material treatment, surface preparation as well as choice of electrical parameters must be optimized.

B. SQUID Amplifier Noise

A SQUID can be modelled as an ideal current-to-voltage amplifier having an input inductor L_i and two noise generators for its voltage and current noise with spectral densities $S_V(\omega)$ and $S_I(\omega)$, respectively, at the amplifier input (see Fig. 4a) [23].

The optimum source impedance, $(S_V/S_I)^{1/2}$, is much smaller than the parasitic impedance ωL_i unless L_i is tuned out (at one frequency) to noise match

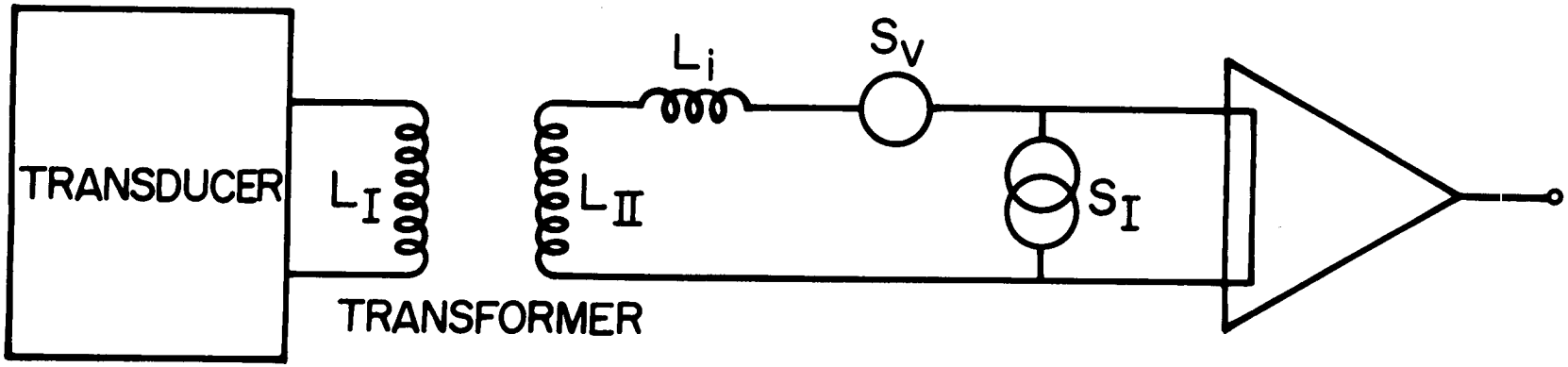

Fig. 4(a). Transducer coupled to a SQUID through a transformer.

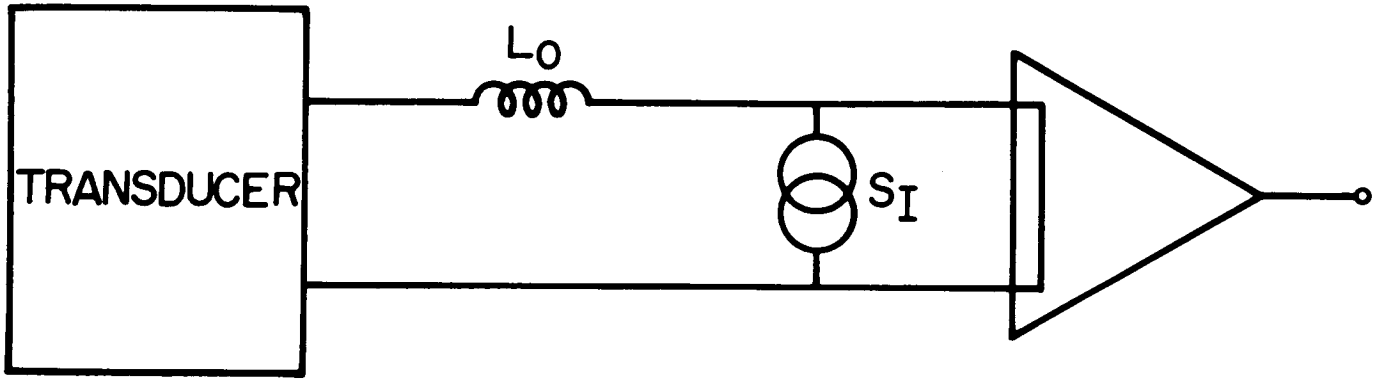

Fig. 4(b). An equivalent circuit of the SQUID noise for an untuned SQUID input.

the input impedance. Therefore, when the SQUID is used as a wideband amplifier, the noise is dominated by S_I and can be characterized by an "input energy sensitivity":

$$E_A(\omega) \equiv \frac{1}{2} L_i S_I(\omega). \tag{74}$$

In a practical gradiometer design, the transducer output inductance L_p is usually larger than L_i and a superconducting transformer is desired to bridge between L_p and L_i. The equivalent load, representing L_i and the transformer, seen by the transducer is an inductor L_o:

$$L_o = \frac{L_i + (1 - k_t^2) L_{II}}{L_i + L_{II}} L_I, \tag{75}$$

where k_t, L_I and L_{II} are the magnetic-field coupling constant, the primary and the secondary inductances of the transformer. The ratio of the power being detected in L_i to the power sent from L_p to L_o is the forward power transfer function $H_p^{I,II}(\omega)$ of the transformer and can be shown to be given by a frequency-independent expression:

$$H_p^{I,II} = \frac{k_t^2 \frac{L_i}{L_{II}}}{(\frac{L_i}{L_{II}} + 1 - k_t^2)(\frac{L_i}{L_{II}} + 1)}. \tag{76}$$

The equivalent current noise for $S_I(\omega)$ seen by the transducer is therefore given by

$$S_I'(\omega) \equiv \frac{L_i S_I(\omega)}{L_o H_p^{I,II}} = \frac{2 E_A(\omega)}{L_o H_p^{I,II}}. \tag{77}$$

Now, the circuit in Fig. 4a can be represented by an equivalent circuit with

the transducer connected in series with L_o and a current-to-voltage amplifier which has the equivalent current noise $S_I'(\omega)$, as shown in Fig. 4b.

The quantity of interest is the equivalent (differential) acceleration noise at the transducer that would correspond to the amplifier noise of Eq. (77). The conversion from current noise to differential acceleration noise is made by use of the transfer function of the transducer, Eq. (53):

$$S_g^A(\omega) = \left[\frac{(\omega_o^2 - \omega^2)(L_o + L_p)}{A\, I'}\right]^2 \frac{2\, E_A(\omega)}{L_o H_p^{I,II}} \,. \tag{78}$$

For $\omega << \omega_o$, substitution of Eq. (73b) reduces this amplifier noise term to

$$S_g^A(\omega) = \frac{4}{m} \frac{\omega_o^2}{2\beta\eta} E_A(\omega) \,, \tag{79}$$

where

$$\eta \equiv \frac{L_o}{L_o + L_p} H_p^{I,II} \tag{80}$$

is the fraction of electrical energy coupled to the amplifier. The product $\beta\eta$ represents the fraction of the total electromechanical energy coupled to the SQUID input, or the "SQUID energy coupling coefficient".

There are three factors to optimize. The transfer function (75) is optimized when the transformer secondary is

$$(L_{II})_{opt} = \frac{L_i}{\sqrt{(1 - k_t^2)}} \,, \tag{81}$$

yielding

$$(H_p^{I,II})_{opt} = \frac{k_t^2}{[1 + \sqrt{(1 - k_t^2)}]^2} \cdot \tag{82}$$

From Eqs. (75) and (81), the transformer primary is chosen according to

$$(L_I)_{opt} = \frac{L_o}{\sqrt{(1 - k_t^2)}} \cdot \tag{83}$$

The impedance factor $L_o/(L_o + L_p)$ in Eq. (80) is maximized by choosing $L_o >> L_p$. Finally, the frequency factor assumes a minimum:

$$\left(\frac{\omega_o^2}{2\beta}\right)_{min} = \omega_o^2 \, , \tag{84}$$

when I' is chosen such that $\beta = 1/2$: namely,

$$\frac{\Lambda^2 I'^2}{m(L_o + L_p)} = \frac{1}{2}\,\omega_o^2 \cdot \tag{85}$$

This last optimization is applicable only when the amplifier noise is dominating.

C. Potential Sensitivity

The fundamental noise of the gradiometer is the sum of its Brownian motion noise and SQUID amplifier noise. In terms of an equivalent gravity gradient noise Γ_n, the spectral density of the gradiometer noise is

$$S_\Gamma(\omega) = \frac{1}{\ell^2}\left[S_g^T(\omega) + S_g^A(\omega)\right] \, , \tag{86}$$

where ℓ is the length of the baseline between the two proof masses. Substitution from Eqs. (71) and (79) gives the one-sided noise spectral

density:

$$S_\Gamma(f) = \frac{4}{m\ \ell^2}\left[\frac{k_B\ T}{\tau\ (f)} + \frac{\omega_o^2}{2\beta\eta}\ E_A(f)\right]\ , \qquad (87)$$

where a factor 2π has been dropped from Eq. (71) by going from the angular frequency domain to the frequency domain. Here, the numeral 4 will become 8 if m_1 is used instead of the reduced mass m.

In the usual case when $\tau_M > \tau_{I'}$, the optimum value for I' satisfies an inequality:

$$0 < \frac{\Lambda^2 I'^2_{opt}}{m(L_o + L_p)} < \frac{1}{2}\ \omega_o^2\ . \qquad (88)$$

Toward the lower bound, the power coupled to the SQUID tends to zero. Toward the upper bound, the Brownian motion noise term increases because of the relatively short $\tau_{I'}$. If the amplifier noise dominates, the choice is made at the upper bound. If this bound is exceeded, the electromechanical spring has become so stiff that a given acceleration signal applied to the proof mass is producing less displacement, thus making it more difficult for the superconducting circuit to measure.

The SQUID input energy sensitivity $E_A(f)$ is usually a white noise plus a 1/f noise at very low frequencies. In addition, a dc drift can be caused by a temperature drift of the gradiometer [14]. The drift changes the penetration depth and hence the inductances of the superconducting circuit [24]. Temperature related drifts can be suppressed by regulating the temperature or be balanced out with an improved circuit [25]. This and other errors are the subject that will be considered in Section V. The noise given in Eq. (87) represents the fundamental noise of the gradiometer which can be reached only

when other instrument errors are suppressed sufficiently. However, having very low fundamental noise in the gradiometer itself is a prerequisite for achieving the desired high sensitivity.

V. ERROR MODEL OF THE INSTRUMENT

As we have seen in Section II, the gradiometer measures in general a differential gravity signal superposed with specific pseudoforces such as centrifugal acceleration and angular acceleration. In addition, the large dc gravity bias is modulated by the motion of the platform, resulting in error signals which compete with the ac signals under investigation. Thermal and electromagnetic fluctuations of the environment can also be coupled to the gradiometer. It is important to have a complete error model of the instrument because, for many applications, errors could dominate over the gravity gradient signals and therefore must be compensated for to recover the true signals. We start this section with a derivation of general expressions for the driving accelerations $g_d(t)$ and $g_c(t)$. We will then elaborate on specific error sources. The kinematic and dynamic error mechanisms discussed in this section are independent of the particular electrical circuit chosen for the superconducting gradiometer. Hence our results have general applicability beyond the specific instrument discussed in this paper.

A. Geometrical Metrology Errors

Let us consider the case in which the gradiometer is used to measure a time-varying in-line component gravity gradient at $\vec{r}$ in the direction of a unit vector $\hat{n}$ fixed in the laboratory frame:

$$\Gamma_{nn}(\vec{r},t) = -(\hat{n}\cdot\vec{\nabla})^2\,\phi(\vec{r},t)\ . \tag{89}$$

Let $\vec{r}_1$ and $\vec{r}_2$ represent the <u>actual</u> position vectors for the centers of mass of the two proof masses m_1 and m_2, and $\hat{n}_1$ and $\hat{n}_2$ be the unit vectors representing the <u>actual</u> sensitive axes of the two component accelerometers, as indicated in

Fig. 5. Let $\vec{\rho}$ and $\vec{\ell}$ represent the average proof mass position vector and the baseline vector of the gradiometer, respectively, so that

$$\vec{r}_1 \equiv \vec{\rho} - \frac{\vec{\ell}}{2} , \tag{90a}$$

$$\vec{r}_2 \equiv \vec{\rho} + \frac{\vec{\ell}}{2} . \tag{90b}$$

Ideally, one wants $\vec{\rho} = \vec{r}$. In general, one has a gradiometer position error $\delta\vec{\rho}$:

$$\vec{\rho} \equiv \vec{r} + \delta\vec{\rho} . \tag{91}$$

Likewise, in an ideal gradiometer, $\hat{n}_1$, $\hat{n}_2$ and $\hat{\ell} \equiv \vec{\ell}/\ell$ are perfectly aligned to each other and are oriented along $\hat{n}$. In a practical gradiometer, however, there are various alignment and orientation errors. The axes alignment errors consist of the misalignment between the sensitive axes of the two accelerometers:

$$\delta\hat{n}_- \equiv \hat{n}_2 - \hat{n}_1 , \tag{92}$$

and the misalignment between the average direction of the sensitive axes and the direction of the baseline $\hat{\ell} \equiv \vec{\ell}/\ell$:

$$\delta\hat{n}_{+\hat{\ell}} \equiv \frac{1}{2}(\hat{n}_2 + \hat{n}_1) - \hat{\ell} . \tag{93}$$

These alignment errors will be shown to cause coupling to the gravity gradient output from the common linear acceleration component along the $\delta\hat{n}_-$ direction

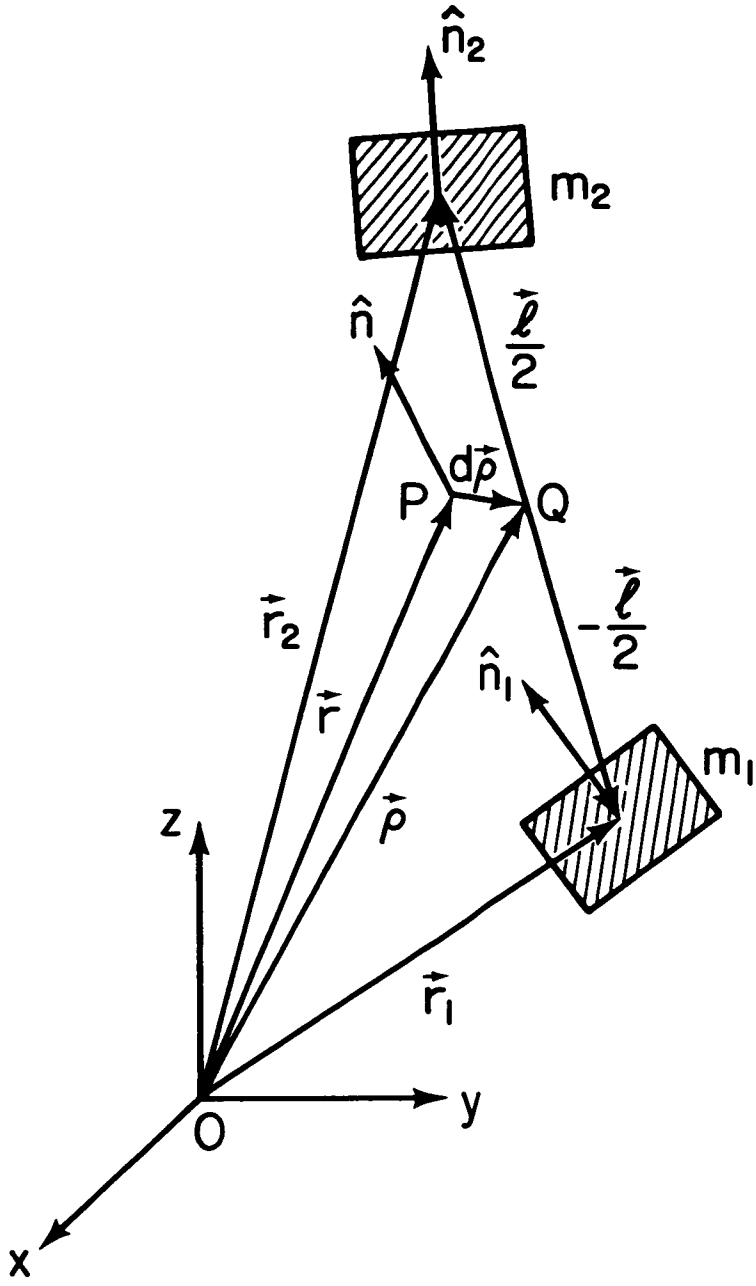

Fig. 5. Position, orientation and sensitive axes alignment of the gradiometer.

and from the angular acceleration component along the $\delta\hat{n}_{\hat{n}} \times \hat{n}$ direction. The gradiometer orientation error is due to the directions $\hat{\ell}^{+\ell}_{+n}$ and $(\hat{n}_2 + \hat{n}_1)/2$ being misoriented from $\hat{n}$ by $\delta\hat{\ell}$ and $\delta\hat{n}_{\hat{n}}$, respectively:

$$\hat{\ell} \equiv \hat{n} + \delta\hat{\ell} \ , \tag{94a}$$

$$\frac{1}{2}(\hat{n}_2 + \hat{n}_1) \equiv \hat{n} + \delta\hat{n}_{\hat{n}}^{+n} \ , \tag{94b}$$

and will be shown to cause coupling from the differential acceleration component along the $\delta\hat{\ell} + \delta\hat{n}_{\hat{n}}^{+n}$ direction. Notice that only one of the two quantities $\delta\hat{\ell}$ and $\delta\hat{n}_{\hat{n}}^{+n}$ in conjunction with the misalignment $\delta\hat{n}_{\hat{n}}^{+\ell}$ in Eq. (93) is sufficient to define the misorientation of the gradiometer. Introducing additional notations in Eqs. (94), however, have the advantage of simplifying expressions for misorientation errors by avoiding explicit reference to the misalignment parameters, defined within the gradiometer hardware.

In order to find the specific forces acting on m_1 and m_2, Eqs. (90) are substituted into Eq. (4). After Taylor series expansion in $\vec{\ell}$, one finds

$$\vec{g}'(\vec{r}_1,t) = -\vec{\nabla}\left[1 - (\frac{\vec{\ell}}{2}\cdot\vec{\nabla}) + \frac{1}{2!}(\frac{\vec{\ell}}{2}\cdot\vec{\nabla})^2 - \frac{1}{3!}(\frac{\vec{\ell}}{2}\cdot\nabla)^3 + \ldots\right]\phi(\vec{\rho},t)$$

$$- \vec{\Omega}(t) \times [\vec{\Omega}(t) \times (\vec{\rho} - \frac{\vec{\ell}}{2})] - \vec{\alpha}(t) \times (\vec{\rho} - \frac{\vec{\ell}}{2}) - \vec{a}(t) \ , \tag{95a}$$

$$\vec{g}'(\vec{r}_2,t) = -\vec{\nabla}\left[1 + (\frac{\vec{\ell}}{2}\cdot\vec{\nabla}) + \frac{1}{2!}(\frac{\vec{\ell}}{2}\cdot\vec{\nabla})^2 + \frac{1}{3!}(\frac{\vec{\ell}}{2}\cdot\vec{\nabla})^3 + \ldots\right]\phi(\vec{\rho},t)$$

$$- \vec{\Omega}(t) \times [\vec{\Omega}(t) \times (\vec{\rho} + \frac{\vec{\ell}}{2})] - \vec{\alpha}(t) \times (\vec{\rho} + \frac{\vec{\ell}}{2}) - \vec{a}(t) \ , \tag{95b}$$

where we dropped the Coriolis terms assuming a rectilinear compliance of the

proof mass suspension. In general, $\vec{\rho}$ and $\vec{\ell}$ are also time-varying due to the translational and rotational motions of the platform with respect to an inertial frame.

In Section IIIB, we defined as the acceleration signal the time-varying part over the constant background gravity of Earth. Since we are now interested in the mechanisms which modulate the Earth's bias to produce error signals, we consider in this section the response of the gradiometer to the <u>total</u> accelerations:

$$g'_k(t) \equiv \hat{n}_k \cdot \vec{g}'(\vec{r}_k,t) = g_k(t) + \hat{n} \cdot \vec{g}_E(\vec{r}) \ . \qquad (96)$$

We return at the end to the signal variables $g_k(t)$ to connect back to the analyses presented in earlier sections. With Earth's gravity vector $\vec{g}_E(\vec{r})$ as defined by Eq. (28), the last equality in Eq. (96) can be viewed as a rigorous re-definition of $g_k(t)$. Here a point-mass (or a spherical-mass) approximation of the proof masses has been used to avoid volume integration of $\vec{g}'(\vec{r}_k,t)$ over the finite dimensions of the proof masses.

The <u>total</u> common and differential accelerations <u>for the gradiometer</u>, defined in a similar fashion as $g_c(t)$ and $g_d(t)$ in Eq. (40), can now be shown to be

$$g'_c(t) = (\hat{n} + \delta\hat{n}_{+n}) \cdot \vec{g}'_{C\vec{\ell}}(\vec{\rho},t) + \frac{1}{4}\,\delta\hat{n}_- \cdot \vec{g}'_{D\vec{\ell}}(\vec{\rho},t) \ , \qquad (97a)$$

$$g'_d(t) = \delta\hat{n}_- \cdot \vec{g}'_{C\vec{\ell}}(\vec{\rho},t) + (\hat{n} + \delta\hat{n}_{+n}) \cdot \vec{g}'_{D\vec{\ell}}(\vec{\rho},t) \ , \qquad (97b)$$

where $\vec{g}'_{C\vec{\ell}}(\vec{\rho},t)$ and $\vec{g}'_{D\vec{\ell}}(\vec{\rho},t)$ are the <u>total true</u> common and differential accelerations acting at $\vec{\rho} \pm \vec{\ell}/2$:

$$\vec{g}'_{C\vec{\ell}}(\vec{\rho},t) = -\vec{\nabla}[1 + \frac{1}{2!}(\frac{\vec{\ell}}{2}\cdot\vec{\nabla})^2 + \ldots]\,\phi(\vec{\rho}) - \vec{a}(\vec{\rho}) \ , \qquad (98a)$$

$$\vec{g}'_{D\vec{\ell}}(\vec{\rho},t) = -\vec{\nabla}[(\vec{\ell}\cdot\vec{\nabla}) + \frac{2}{3!}(\frac{\vec{\ell}}{2}\cdot\nabla)^3 + \ldots]\phi(\vec{\rho}) - \vec{\Omega}\times(\vec{\Omega}\times\vec{\ell}) - \vec{\alpha}\times\vec{\ell} . \qquad (98b)$$

Here $\vec{a}(\vec{\rho})$ is the total linear acceleration experienced at $\vec{\rho}$:

$$\vec{a}(\vec{\rho}) \equiv \vec{\Omega}\times(\vec{\Omega}\times\vec{\rho}) + \vec{\alpha}\times\vec{\rho} + \vec{a} \ , \qquad (99)$$

and the time dependencies have been omitted on the righthand side of Eqs. (98) for notational simplicity.

Equations (97) through (99) are in the platform frame representation. It is straightforward to convert these equations into the laboratory frame representation by substituting Eqs. (91), (93) and (94). The relative uncertainties between the two frames, $\delta\vec{\rho}$, $\delta\hat{n}_{\underset{+n}{\wedge}}$ and $\delta\hat{\ell}$, then constitute new error sources. Thus, it can be shown that Eqs. (97) become

$$g'_c(t) = (\hat{n} + \delta\hat{n}_{\underset{+n}{\wedge}})\cdot\vec{g}'(\vec{r}+\delta\vec{\rho},t) + \frac{\ell}{4}\,\delta\hat{n}_-\cdot\vec{\vec{\Gamma}}'(\vec{r}+\delta\vec{\rho},t)\cdot(\hat{n}+\delta\hat{\ell})$$

$$-\frac{\ell}{4}\,\delta\hat{n}_-\cdot\vec{\alpha}\times(\hat{n}+\delta\hat{\ell}) + \delta g_{c,\vec{\ell}} \ , \qquad (100a)$$

$$g'_d(t) = \delta\hat{n}_-\cdot\vec{g}'(\vec{r}+\delta\vec{\rho},t) + \ell\,(\hat{n}+\delta\hat{n}_{\underset{+n}{\wedge}})\cdot\vec{\vec{\Gamma}}'(\vec{r}+\delta\vec{\rho},t)\cdot(\hat{n}+\delta\hat{\ell})$$

$$-\ell\,\delta\hat{n}_{\underset{+\ell}{\wedge}}\cdot\vec{\alpha}\times\hat{n} + \delta g_{d,\vec{\ell}} \ . \qquad (100b)$$

Here $\vec{g}'$ and $\vec{\vec{\Gamma}}'$ are the specific force vector and the specific force gradient tensor defined in Eqs. (4) and (8); $\delta g_{c,\vec{\ell}}$ and $\delta g_{d,\vec{\ell}}$ are the finite size terms given in Eqs. (A1). Equation (100b) shows that the "sensitive axis of the

gradiometer" can be defined by the average of $(\hat{n}_1 + \hat{n}_2)/2$ and $\hat{\ell}$.

B. General Description of Errors

The accelerations in Eqs. (100) contain two types of error sources. The first type is intrinsic error sources due to angular motions as given in Eqs. (4) and (8), the second type is in geometrical metrology. Further error sources arise from non-ideal behaviors of the mechanical and electrical springs, scale factor mismatch, incorrect calibration, and residual coupling of the gradiometer to temperature and electromagnetic fluctuations of the environment, etc. Equation (45) can therefore be generalized as

$$i_d(\omega) = H^c_{gi}(\omega)\, g_c(\omega) + H^d_{gi}(\omega)\, g_d(\omega) + H^{cc}_{Gi}(\omega)\, G_{cc}(\omega) + H^{dd}_{Gi}(\omega)\, G_{dd}(\omega)$$

$$+ H^{cd}_{Gi}(\omega)\, G_{cd}(\omega) + H^c_{Ti}(\omega)\, T_c(\omega) + H^d_{Ti}(\omega)\, T_d(\omega) + \ldots, \qquad (101)$$

where $G_{cc}(\omega)$, $G_{dd}(\omega)$ and $G_{cd}(\omega)$ are the Fourier transforms of

$$G_{cc}(t) \equiv [g_c(t)]^2, \qquad (102a)$$

$$G_{dd}(t) \equiv [g_d(t)]^2, \qquad (102b)$$

$$G_{cd}(t) \equiv g_c(t) g_d(t), \qquad (102c)$$

and $T_c(\omega)$ and $T_d(\omega)$ are the Fourier transforms of the common and differential temperature fluctuations, $T_c(t)$ and $T_d(t)$, over the two transducers, defined in Eqs. (A26). The coefficients in front of these functions represent the transfer functions for the signal variables that they are multiplied with.

The centrifugal acceleration and the linear and angular accelerations, which are coupled to the gradiometer due to its metrology errors, appear in Eq. (101) through errors in $g_c(\omega)$ and $g_d(\omega)$ that they cause.

Notice that Eq. (101) contains the original signal variables, $g_c(\omega)$ and $g_d(\omega)$, which are identical to $g'_c(\omega)$ and $g'_d(\omega)$ due to the relationships:

$$g_c(t) = g'_c(t) - \hat{n} \cdot \vec{g}_E(\vec{r}) \ , \tag{103a}$$

$$g_d(t) = g'_d(t) \ , \tag{103b}$$

which follow from Eq. (96). Equations (103) imply that the errors in the unprimed variables are given by the errors in the primed variables:

$$\delta g_c(t) = \delta g'_c(t) \ , \tag{104a}$$

$$\delta g_d(t) = \delta g'_d(t) \ . \tag{104b}$$

It is also clear that the Fourier components of the errors are also identifical between the two sets of variables. Equations (100) and (103) can be combined to obtain the unperturbed acceleration signals:

$$g_{co}(\omega) = g'_{co}(\omega) = \hat{n} \cdot [\vec{g}(\vec{r},\omega) - \vec{a}(\vec{r},\omega)] \ , \tag{105a}$$

$$g_{do}(\omega) = g'_{do}(\omega) = \ell \, \hat{n} \cdot [\overleftrightarrow{\Gamma}(\vec{r},\omega) - \overleftrightarrow{C}(\omega)] \cdot \hat{n} \ , \tag{105b}$$

where $\vec{g}(\vec{r},\omega)$, $\vec{a}(\vec{r},\omega)$, $\overleftrightarrow{\Gamma}(\vec{r},\omega)$ and $\overleftrightarrow{C}(\omega)$ are the Fourier transforms of

$$\vec{g}(\vec{r},t) \equiv -\vec{\nabla}\phi(\vec{r},t) = -\vec{\nabla}\phi_p(\vec{r},t) - \vec{\nabla}\phi_E(\vec{r}) \ , \qquad (106a)$$

$$\vec{a}(\vec{r},t) = \vec{a}_p(\vec{r},t) + \vec{\Omega}_E \times [\vec{\Omega}_E \times (\vec{R}_E + \vec{r})] \ , \qquad (106b)$$

$$\vec{\vec{\Gamma}}(\vec{r},t) \equiv -\vec{\nabla}\vec{\nabla}\phi(\vec{r},t) = -\vec{\nabla}\vec{\nabla}\phi_p(\vec{r},t) - \vec{\nabla}\vec{\nabla}\phi_E(\vec{r}) \ , \qquad (106c)$$

$$\vec{\vec{C}}(t) \equiv \vec{\dot{\Omega}}(t)\,\vec{\Omega}(t) - \Omega^2(t)\,\vec{\vec{I}} \ . \qquad (106d)$$

Here $\phi_E(\vec{r})$, Ω_E and R_E are Earth's variables introduced in Eq. (28); $\phi_p(\vec{r},t)$ and $\vec{a}_p(\vec{r},t)$ are the gravitational potential and the linear acceleration measured relative to Earth; and $\vec{\vec{C}}(t)$ is the "centrifugal accelerator tensor." The dyadic notation is used in Eqs. (106) to represent rank-2 tensors. The first term in Eq. (105b) is ℓ times the gravity gradient signal $\Gamma_{nn}(\vec{r},\omega)$ to be measured.

It is useful to divide Eq. (101) by $\ell\, H^d_{gi}(\omega)$ to obtain an equation of the form:

$$[\Gamma_{nn}(\vec{r},\omega)]_{\text{measured}} \equiv \frac{1}{\ell}\frac{i_d(\omega)}{H^d_{gi}(\omega)} = [\Gamma_{nn}(\vec{r},\omega)]_{\text{true}} + \frac{1}{\ell}\sum_i \delta g_{d,i}(\omega) \ , \qquad (107)$$

where $\delta g_{d,i}(\omega)$ is the <u>equivalent</u> error in the differential acceleration $g_d(\omega)$ due to the i-th type error source. Derivation and discussion of $\delta g_{d,i}$ for various error sources are given in Appendix. Equation (107) can be converted into another convenient form:

$$\delta\Gamma_{nn}(\vec{r},\omega) = \sum_{\ell,m} \varepsilon^{\Gamma}_{n\ell m}(\omega)\,\Gamma_{\ell m}(\vec{r},\omega) + \sum_{\ell,m} \varepsilon^{C}_{n\ell m}(\omega)\,C_{\ell m}(\omega) + \sum_{\ell} \varepsilon^{a}_{n\ell}(\omega)\,a_{\ell}(\vec{r},\omega)$$

$$+ \sum_{\ell} \varepsilon^{\Omega}_{n\ell}(\omega)\,\Omega_{P,\ell}(\omega) + \varepsilon^{T}_{n}(\omega)\,T_c(\omega) + \cdots \ , \qquad (108)$$

in which dominant error sources have been shown explicity. Here the laboratory has been assumed to be stationary with respect to Earth and $\vec{\Omega}_p(\omega)$ is the angular velocity of the platform in the laboratory frame. The first two error coefficients can be identified from Eqs. (A6b) and (A19):

$$\varepsilon^{\Gamma}_{n\ell m}(\omega) = \delta_{\ell n}\delta_{mn}\delta\sigma_{\Gamma}(\omega) + (1 - \delta_{\ell n})\,\delta_{mn}(\delta\hat{n}_{\hat{+n}} + \delta\hat{\ell})_{\ell}\,, \qquad (109a)$$

$$\varepsilon^{C}_{n\ell m}(\omega) = -\,\delta_{\ell n}\delta_{mn}\delta\sigma_{C}(\omega) - (1 - \delta_{\ell n})\,\delta_{mn}(\delta\hat{n}_{\hat{+n}} + \delta\hat{\ell})_{\ell}\,, \qquad (109b)$$

where $\delta\sigma_{\Gamma}(\omega)$ and $\delta\sigma_{C}(\omega)$ are the (dimensionless) calibration error coefficients for $\vec{\vec{\Gamma}}(\vec{r},\omega)$ and $\vec{\vec{C}}(\omega)$, respectively. It is assumed that the zeroth order part of $\vec{\vec{C}}(\omega)$ has been measured independently and removed from the gradiometer output. Otherwise, $\delta\sigma_{c}(\omega)$ must be replaced by unity. The common acceleration error coefficient is read off Eq. (A21):

$$\varepsilon^{a}_{n\ell}(\omega) = -\,\delta_{\ell n}\,\frac{1}{\ell}\,\delta\sigma_{S}(\omega) - (1 - \delta_{\ell n})\,\frac{1}{\ell}\,(\delta\hat{n}_{-})_{\ell}\,, \qquad (109c)$$

where $\delta\sigma_{S}(\omega)$ is the (dimensionless) scale factor mismatch between two constituent accelerometers. The coefficient for the first-order angular velocity induced error is obtained from Eqs. (A10) and (A12):

$$\varepsilon^{\Omega}_{n\ell}(\omega) = (1 - \delta_{\ell n})\,2\Omega_{E,\ell} - \frac{1}{j\omega\ell}\sum_{k,m}(1 - \delta_{kn})\,\varepsilon_{k\ell m}\,(\delta\hat{n}_{-})_{k}\,g_{E,m}(\vec{r})$$

$$+\,j\omega\sum_{k}(1 - \delta_{kn})\,\varepsilon_{k\ell n}\,(\delta\hat{n}_{\hat{+\ell}})_{k}\,, \qquad (109d)$$

where $\delta\vec{\Omega}_p = \vec{\Omega}_p$ has been assumed and $\varepsilon_{k\ell m}$ is the totally antisymmetric tensor of rank 3.

Unlike in some conventional gravity gradimeters, matching of proof masses and spring constants are not necessary in the superconducting device because the balance is achieved by tuning persistent currents. However, the alignment of the sensitive axes of the proof masses is still important.

The temperature error coefficient can be determined from the results of Section H of Appendix. Depending on the relative magnitude of the two competing thermal effects, the error coefficient can be written as

$$\varepsilon_n^T(\omega) = \frac{1}{\ell}\, h_{Tc}(\omega) \ , \tag{109e}$$

where $h_{Tc}(\omega)$ is given by Eq. (A42a), or by

$$\varepsilon_n^T(\omega) = \frac{1}{\ell}\, \delta\sigma_S(\omega)\ g_E \cos\theta_n \frac{1}{E(T)} \frac{dE}{dT} \ , \tag{109e'}$$

where E(T) is the Young's modulus of the spring material at temperature T.

In Paper II, we discuss the observed values or limits of these major error coefficients. Once these error coefficients have been determined experimentally, the relevant dynamic variables can be measured simultaneously along with the gravity gradient by independent instrumentation and the respective errors can be compensated for by using the error model derived in this section and Appendix. In a three-axis gradiometer, it is possible to suppress several error sources by using the geometrical properties of the device [18].

VI. SUMMARY AND CONCLUSION

A gravity gradiometer is a fundamental instrument which can separate gravity from frame accelerations. A sensitive tensor gravity gradiometer needs to be developed to carry out precision tests on gravity as well as for applications in gravity survey and inertial navigation. Since a large common mode background has to be removed in gradiometry by differencing signals at two or more proof masses, extreme stability is required for the sensitive axis orientation and for the scale factors of the component accelerometers. We have shown how these challenges can be met at low temperatures by utilizing the stability of persistent currents, the enhanced mechanical stability of materials and the sensitivity of SQUID amplifiers. An accompanying penalty is of course the inconvenience of having to keep the instrument in liquid helium. The liquid helium environment, however, can be used further to isolate the gradiometer from the fluctuations in the ambient temperature and electromagnetic fields.

In this paper, we have analyzed a superconducting current-differencing gravity gradiometer. Complete dynamical equations have been derived from the first principles. Transfer functions, common mode balance conditions and procedures as well as a rather extensive error model have been developed from these equations. The complicated differential instrument has been reduced to an equivalent accelerometer which simplifies the noise analysis and the electronic control of the device. In Paper II, we report the performance of the superconducting gradiometer in the laboratory, which verifies details of the theory developed here. Although our analysis has been confined to a specific instrument reported in Paper II, the theoretical methods presented in this paper will be a useful guide in analyzing other superconducting inertial instruments that may be developed in the future.

ACKNOWLEDGEMENTS

We would like to thank Professors Daniel DeBra and Alex Dragt for valuable suggestions. We also thank Dr. M.V. Moody for fruitful collaboration in the experiment which checks the theory developed here and Mr. K. Fitzgibbon for proof reading this manuscript.

APPENDIX: DERIVATION OF VARIOUS ERROR COEFFICIENTS

A. Finite Size Effects

There are two error sources related to the finite dimensions of a practical gradiometer: (1) the finite volume of the proof masses and (2) the finite baseline of the instrument. The first effect can be minimized by choosing a nearly spherical geometry for the proof masses, whereas the second effect is reduced when the baseline length $\ell = |\vec{\ell}|$ is shortened. The finite baseline effect has been taken into account in Eqs. (95) by the Taylor expansion in $\vec{\ell}$. The finite volume effect has been ignored in the previous analysis because of its high order nature. The departure from a spherical geometry gives a nonvanishing quadrupole moment to each proof mass or a small octupole moment to the gradiometer. Since this will couple at best to the fourth order derivatives of $\phi(\vec{\rho},t)$, which is generally small except when the source is extremely close to the gradiometer, this error can be ignored in most situations. Clearly, the finite volume error is always smaller than the finite baseline error.

The dominant gravity error terms arising from the finite baseline are obtained from Eqs. (97) and (98).

$$\delta g_{c,\vec{\ell}}(t) = -\frac{\ell^2}{8}(\hat{\ell}\cdot\vec{\nabla})^3\,\phi(\vec{\rho},t)\ , \tag{A1a}$$

$$\delta g_{d,\vec{\ell}}(t) = -\frac{\ell^3}{24}(\hat{\ell}\cdot\vec{\nabla})^4\,\phi(\vec{\rho},t)\ . \tag{A1b}$$

When $\phi(\vec{\rho},t)$ varies with a characteristic length R, these errors become $O(\ell^2/R^2)$ of the signal. Therefore, the finite baseline error can also be ignored when $\ell/R \ll 1$.

B. Misposition of the Gradiometer

The acceleration errors due to the misposition of the gradiometer are obtained from Eqs. (4) and (100):

$$\delta g_{c,\vec{\rho}}(t) = -\hat{n} \cdot [\vec{\nabla}\vec{\nabla}\phi(\vec{r}) + \vec{\Omega}\vec{\Omega} - \Omega^2\vec{\vec{I}}] \cdot \delta\vec{\rho} - \hat{n} \cdot \vec{\alpha} \times \delta\vec{\rho} \ , \quad \text{(A2a)}$$

$$\delta g_{d,\vec{\rho}}(t) = -\ell\,(\hat{n} \cdot \vec{\nabla})[\hat{n} \cdot \vec{\nabla}\vec{\nabla}\phi(\vec{r}) \cdot \delta\vec{\rho}] \ , \quad \text{(A2b)}$$

to the leading order in $\delta\vec{\rho}$. These errors are usually negligible because of the higher order gradients involved. The displacement $\delta\vec{\rho}(t)$, produced by the linear acceleration $\vec{a}(\vec{r},t)$, modulates the large dc gravity of Earth and produces errors that compete with ac signals:

$$\delta g_{c,\vec{\rho}}(t) = 0\left(\frac{\delta\rho(t)}{R_E}\, g_E\right) \ , \quad \text{(A3a)}$$

$$\delta g_{d,\vec{\rho}}(t) = 0\left(\frac{\delta\rho(t)}{R_E}\, \ell\Gamma_E\right) \ , \quad \text{(A3b)}$$

where $g_E \equiv 9.8\ \text{m s}^{-2}$, $\Gamma_E \equiv 3.1 \times 10^3$ E and $R_E \equiv 6.4 \times 10^6$ m are the vertical gravitational acceleration, the vertical gravity gradient and the radius of Earth. It is clear that these errors can be ignored in general because $\delta\rho(t)/R_E \ll 1$.

C. Misalignment and Misorientation of the Gradiometer

The acceleration errors caused by the misalignments, $\delta\hat{n}_-$ and $\delta\hat{n}_{\hat{+}\ell}$, and the misorientations, $\delta\hat{n}_{\hat{+}n}$, and $\delta\hat{\ell}$, are obtained from Eqs. (100):

$$\delta g_{c,n+\ell}(t) = \delta\hat{n}_{\hat{+}n} \cdot \vec{g}'(\vec{r},t) + \frac{\ell}{4}(\delta\hat{n}_- + \delta\hat{\ell}) \cdot \vec{\vec{\Gamma}}'(\vec{r},t) \cdot \hat{n}$$

$$- \frac{\ell}{4} \delta\hat{n}_- \cdot \vec{\alpha} \times \hat{n} , \qquad \text{(A4a)}$$

$$\delta g_{d,n+\ell}(t) = \delta\hat{n}_- \cdot \vec{g}'(\vec{r},t) + \ell(\delta\hat{n}_{+n} + \delta\hat{\ell}) \cdot \vec{\Gamma}'(\vec{r},t) \cdot \hat{n}$$

$$- \ell \, \delta\hat{n}_{+\ell} \cdot \vec{\alpha} \times \hat{n} , \qquad \text{(A4b)}$$

to the leading order in $\delta\hat{n}_-$, $\delta\hat{n}_{+\ell}$, $\delta\hat{n}_{+n}$. It follows from the definitions (92) - (94) that, in the limits $|\delta\hat{n}_-|$, $|\delta\hat{n}_{+\ell}|$, $|\delta\hat{n}_{+n}|$, $|\delta\hat{\ell}| \ll 1$,

$$\delta\hat{n}_-, \delta\hat{n}_{+\ell}, \delta\hat{n}_{+n}, \delta\hat{\ell} \perp \hat{n} . \qquad \text{(A5)}$$

Hence these errors cause the cross components of the common acceleration and the acceleration gradient to couple to the gradiometer. Written out explicitly, Eqs. (A4) become

$$\delta g_{c,n+\ell}(t) = - \delta\hat{n}_{+n} \cdot [\vec{\nabla}\phi(\vec{\rho}) + \vec{a}(\vec{\rho})] - \frac{\ell}{4} (\delta\hat{n}_- + \delta\hat{\ell}) \cdot [\vec{\nabla}\vec{\nabla}\phi(\vec{\rho}) + \vec{\Omega}\vec{\Omega}] \cdot \hat{n}$$

$$- \frac{\ell}{4} \delta\hat{n}_- \times \hat{n} \cdot \vec{\alpha} , \qquad \text{(A6a)}$$

$$\delta g_{d,n+\ell}(t) = - \delta\hat{n}_- \cdot [\vec{\nabla}\phi(\vec{\rho}) + \vec{a}(\vec{\rho})] - \ell \, (\delta\hat{n}_{+n} + \delta\hat{\ell}) \cdot [\vec{\nabla}\vec{\nabla}\phi(\vec{\rho}) + \vec{\Omega}\vec{\Omega}] \cdot \hat{n}$$

$$- \ell \, \delta\hat{n}_{+\ell} \times \hat{n} \cdot \vec{\alpha} . \qquad \text{(A6b)}$$

In Eq. (A6b), the misalignments <u>within</u> the gradiometer are expressed in terms of the misalignment $\delta\hat{n}_-$ of the accelerometer axes with respect to each other and the misalignment $\delta\hat{n}_{+\ell}$ between the average accelerometer axis $(\hat{n}_1 + \hat{n}_2)/2$ and the baseline direction $\hat{\ell}$. These errors cause coupling to

cross components of linear and angular accelerations which can be large compared with acceleration gradient signals of interest. The combined error $\delta\hat{n}_{+n} + \delta\hat{\ell}$ appearing in the second term of Eq. (A6b) represents the misorientation of the gradiometer sensitive axis relative to the theoretical direction $\hat{n}$ fixed to the laboratory frame, which is used for interpretating the data. This misorientation produces coupling to cross gradients.

The coupling to the gradiometer from the dynamic variables of the platform, $\vec{a}(\vec{\rho},t)$, $\vec{\Omega}(t)$ and $\vec{\alpha}(t)$, are revealed in Eqs. (A6). Since $\hat{\ell}$ and $\delta\hat{n}_{\pm}$ are time-varying in general due to $\vec{\Omega}(t)$, the large dc gravity of Earth, $\phi_E(\vec{\rho})$, will be modulated to produce errors at the frequency of interest. This important error mechanism will be studied in detail in the next section.

D. Angular Motions of the Platform

The centrifugal acceleration appears without attenuation in Eq. (105b) in direct competition with the gravity gradient signal. This problem is fundamental in any second-order gradiometer, in-line or cross component, as is evidenced by Eq. (9), and therefore does not depend on the particular design of the instrument. This makes the attitude control or detection as the most formidable task in precision gravity gradiometry. One can easily compute the required attitude rate ($\vec{\Omega}$) accuracy from Eq. (105b) for a given sensitivity of $\ddot{\Gamma}$.

When the instrument is in a laboratory rotating at an angular velocity $\vec{\Omega}_o(t)$ with respect to an inertial frame, it is convenient to define

$$\vec{\Omega}(t) \equiv \vec{\Omega}_o(t) + \vec{\Omega}_p(t) \ . \qquad \text{(A7)}$$

If uncertainties in $\vec{\Omega}_o(t)$ and $\vec{\Omega}_p(t)$ are $\delta\vec{\Omega}_o(t)$ and $\delta\vec{\Omega}_p(t)$, respectively, then

the error in the differential acceleration due to centrifugal acceleration is obtained from Eqs. (105b), (106d) and (A7) as

$$\delta g_{d,\vec{C}}(t) = -2\ell\,[\{\hat{n}\cdot(\vec{\Omega}_o + \vec{\Omega}_p)\}\{\hat{n}\cdot(\delta\vec{\Omega}_o + \delta\vec{\Omega}_p)\} - (\vec{\Omega}_o + \vec{\Omega}_p)\cdot(\delta\vec{\Omega}_o + \delta\vec{\Omega}_p)]\,. \tag{A8}$$

If the gradiometer platform is moving with a velocity $\vec{v}(t)$ with respect to Earth and the gradiometer is in a local geographic orientation, then $\vec{\Omega}_o(t)$ is given by

$$\vec{\Omega}_o(t) = \vec{\Omega}_E + R_E^{-2}\,\vec{R}_E \times \vec{v}(t)\,, \tag{A9}$$

where $\vec{\Omega}_E$ and $\vec{R}_E$ are the angular velocity and radius vectors of Earth, introduced in Eq. (28). In the case when the platform is stationary with respect to Earth; i.e. $\vec{v}(t) = 0$, Eq. (A8) reduces, after Fourier transformation, to

$$\delta g_{d,\vec{C}}(\omega) = -2\ell\,[(\hat{n}\cdot\vec{\Omega}_E)\{\hat{n}\cdot\delta\vec{\Omega}_p(\omega)\} - \vec{\Omega}_E\cdot\delta\vec{\Omega}_p(\omega)]\,, \tag{A10}$$

where we have assumed the condition $\Omega_P << \Omega_E = 7.27 \times 10^{-5}$ rad s^{-1}, which is not difficult to satisfy for a stationary platform.

In a terrestrial laboratory, the <u>modulation of Earth's gravity bias</u> by the tilt of the sensitive axes is another important error mechanism, as was pointed out in Section C of this Appendix. Since the common mode errors in Eq. (A6a) produce second order errors in the differential signal when multiplied by the common mode balance error H_{gi}^{c} according to Eq. (51), these errors will, in general, be dominated by the errors in Eq. (A6b), which is multipled by H_{gi}^{d}.

When the platform moves at an angular velocity $\vec{\Omega}_p(t)$ with respect to the terrestrial laboratory, the misalignment and misorientation vectors are modulated according to

$$\frac{d}{dt}\vec{A} = \vec{\Omega}_p(t) \times \vec{A} , \tag{A11}$$

where $\vec{A}$ stands for $\delta\hat{n}_-$, $\delta\hat{n}_{+\ell}$, $\delta\hat{n}_{+n}$ and $\delta\hat{\ell}$. Equation (A6b) becomes, upon Fourier transformation,

$$\delta g_{d,n+\ell}(\omega) = -\delta\hat{n}_- \cdot \frac{\vec{\Omega}_p(\omega)}{j\omega} \times \vec{g}_E(\vec{r}) - \ell(\delta\hat{n}_{+n} + \delta\hat{\ell}) \cdot \frac{\vec{\Omega}_p(\omega)}{j\omega} \times [\vec{\Gamma}_E(\vec{r}) \cdot \hat{n}]$$

$$-\ell\, \delta\hat{n}_{+\ell} \times \hat{n} \cdot [j\omega\, \vec{\Omega}_p(\omega)] , \tag{A12}$$

where $\vec{g}_E \equiv -\vec{\nabla}\phi_E$, $\vec{\Gamma}_E \equiv -\vec{\nabla}\vec{\nabla}\phi_E$ and $\vec{\alpha}(\omega) \equiv j\omega\, \vec{\Omega}_p(\omega)$ were substituted. The term arising from the angular modulation of $\delta\hat{n}_{+\ell}$ produces a second order effect in $\vec{\Omega}_p(\omega)$ and therefore has been dropped. In the case when

$$|\delta\hat{n}_-| > |\delta\hat{n}_{+n} + \delta\hat{\ell}| \times \frac{\ell\Gamma_E}{g_E} , \tag{A13}$$

the second term in Eq. (A12) can be ignored. The third term becomes negligible compared to the first term at sufficiently low signal frequencies:

$$\omega < \left(\frac{g_E}{\ell}\right)^{1/2} \left|\frac{\delta\hat{n}_-}{\delta\hat{n}_{+\ell}}\right|^{1/2} . \tag{A14a}$$

Comparing Eq. (A12) with Eq. (A10), one finds that the time-varying tilt noise is the dominant source of angular motion induced errors in the frequency range

$$\omega < \frac{g_E}{\ell\Omega_E} |\hat{\delta n}_-| \ , \qquad \text{(A14b)}$$

even when $\delta\vec{\Omega}_p = \vec{\Omega}_p$, the worst case for the centrifugal acceleration error. In Paper II, we will see that the angular motion noise given by Eq. (12) is indeed the dominant error mechanism for our prototype superconducting gravity gradiometer.

The foregoing discussion clearly reveals the advantage of operating a sensitive gradiometer in space where the gradiometer platform is freely falling. If an Earth-pointing reference frame is chosen so that $\vec{\Omega}_o(t)$ coincides with the orbital angular velocity of the satellite, then Eqs. (A8) and (A6b) reduce respectively to

$$[\delta g_{d,\vec{\vec{C}}}(\omega)]_{space} = -2\ell \ [(\hat{n} \cdot \vec{\Omega}_o)\{\hat{n} \cdot \delta\vec{\Omega}_p(\omega)\} - \vec{\Omega}_o \cdot \delta\vec{\Omega}_p(\omega)] \ , \qquad \text{(A15)}$$

$$[\delta g_{d,\hat{n}+\hat{\ell}}(\omega)]_{space} = -\ell \ (\delta\hat{n}_{+\hat{n}} + \delta\hat{\ell}) \cdot \frac{\vec{\Omega}_p(\omega)}{j\omega} \times [\vec{\vec{\Gamma}}_E(\vec{r}) - \vec{\Omega}_o\vec{\Omega}_o] \cdot \hat{n}$$

$$-\ell \ \delta\hat{n}_{+\hat{\ell}} \times \hat{n} \cdot [j\omega \ \vec{\Omega}_p(\omega)] \ , \qquad \text{(A16)}$$

where $\vec{\vec{\Gamma}}_E(\vec{r})$ is the gravity gradient tensor of (spherical) Earth. Comparison of Eqs. (A15) and (A16) leads to a conclusion that the centrifugal acceleration error could be dominant in most practical cases.

One can see from Eq. (A8) that $\delta g_{d,\vec{\vec{C}}}(t)$ has a minimum when the gradiometer is in an inertial orientation; i.e., $\vec{\Omega}_o = 0$. The worst situation for the centrifugal acceleration error is the case when the gradiometer is rotated at a frequency high compared to the signal frequency for heterodyne detection of the gravity signal. In this case, $\vec{\Omega}_o$ is the spin angular velocity which is large compared to $\vec{\Omega}_E$. One advantage of the superconducting gravity gradio-

meter is that the heterodyne detection is not necessary, unlike in some conventional devices, because of its low drift and excellent low frequency noise characteristics. The superconducting gradiometer therefore permits complete freedom in orientation: inertial, earth-pointing, or spin-stabilized [26]. Hence, an optimum orientation, which minimizes the overall error budget, is available to the superconducting instrument although the angular motion induced errors are fundamental.

In Eqs. (A10) and (A15), we considered only the first order errors in $\delta\vec{\Omega}_p(\omega)$. This is justified when $\delta\vec{\Omega}_p(\omega)$ is bandwidth limited. The Fourier transform of $[\delta\vec{\Omega}_p(t)]^2$ down-converts the centrifugal acceleration noise from high frequencies to the vicinity of dc, the signal bandwidth. A low-pass filter for angular vibrations of the platform is therefore needed to suppress this error.

E. Scale Factor Errors

There are two types of scale factor errors in a gradiometer: (1) a relative error, which comes from the mismatch of the scale factors of the component accelerometers, and (2) an absolute error, which is the error in the calibration of the gradiometer transfer function. Since the scale factors are determined by persistent currents in the superconducting gradiometer, extreme stability is expected in the scale factor match and calibration. The passive, iterative, common mode balance procedure described in Section IIID allows in principle an arbitrarily precise match of scale factors in one direction independent of signal frequency. In practice, however, $H^c_{gi}(\omega)$ is not precisely zero in Eq. (101), thus producing a common mode rejection error, and $H^d_{gi}(\omega)$ also contains a calibration error $\delta H^d_{gi}(\omega)$.

Let us define the (dimensionless) coefficients for scale factor mismatch

and gradiometer calibration error by

$$\delta\sigma_S(\omega) \equiv \frac{H^c_{gi}(\omega)}{H^d_{gi}(\omega)} , \tag{A17a}$$

$$\delta\sigma_\Gamma(\omega) \equiv \frac{\delta H^d_{gi}(\omega)}{H^d_{gi}(\omega)} - \frac{\delta\ell}{\ell} , \tag{A17b}$$

and for the centrifugal acceleration calibration error by $\delta\sigma_C(\omega)$, which is usually different from $\delta\sigma_\Gamma(\omega)$ because independent instruments, such as gyroscopes, are used to measure and compensate the effect. The error arising from the use of an inaccurate value of ℓ in the recovery of $\Gamma_{nn}(\vec{r},t)$ from $g_{do}(t)$ in Eq. (105b) is represented by the second term in Eq. (A17b). With the aid of Eqs. (105), the equivalent differential acceleration errors due to scale factor mismatch and calibration errors can be written as

$$\delta g_{d,S}(\omega) = \delta\sigma_S(\omega)\ \hat{n} \cdot [\vec{g}(\vec{r},\omega) - \vec{a}(\vec{r},\omega)] , \tag{A18}$$

$$\delta g_{d,C}(\omega) = \ell\ \hat{n} \cdot [\delta\sigma_\Gamma(\omega)\ \vec{\Gamma}(\vec{r},\omega) - \delta\sigma_C(\omega)\ \vec{C}(\omega)] \cdot \hat{n} . \tag{A19}$$

The platform motion terms usually dominate over the ac gravity terms in these equations. The second term in Eq. (A19) constitutes an additional rotation induced error which must be added to the list considered in the previous section. The linear acceleration term in Eq. (A18) will be discussed in the following section along with other translation induced error sources.

Now, we briefly discuss $\delta\sigma_S(\omega)$ which arises from the failure to apply the wideband balance procedure. If the balance is attempted at a single frequency ω_b, Eq. (48) must be violated in general. Substituting Eqs. (46) into Eq. (A17a) and expanding it in a Taylor series, one finds

$$\delta\sigma_S(\omega) = \frac{2(\omega_b - \omega)\,\omega_b(\omega_{2c}^2 - \omega_{1c}^2)}{(\omega_{ic}^2 - \omega_b^2)(\omega_{2c}^2 - \omega_b^2)} + \delta\sigma_S(\omega_b), \qquad \text{(A20)}$$

where $\delta\sigma_S(\omega_b)$ is a residual balance error at ω_b. Although not essential, a highly symmetric gradiometer is convenient because $\omega_{2c} \simeq \omega_{1c}$ and, therefore, the wideband balance can be achieved with only two persistent currents I_1 and $I_2 \simeq I_1$ while keeping $i_1 = i_2 = 0$.

F. Linear Motions of the Platform

Although several sources of linear motion induced errors have been shown in the previous sections, it is instructive to combine these effects here. The linear velocity dependent Coriolis force term has been dropped in Eqs. (95) on the assumption that the proof masses are confined to move along the linear directions $\hat{n}_1$ and $\hat{n}_2$. A non-vanishing residual compliance in the directions perpendicular to the sensitive axes would allow the proof masses to respond to the transverse components of accelerations, thereby contributing to a velocity dependent error. It is therefore important to design the suspension spring with high stiffness for all undesired degrees of freedom while obtaining a very weak spring in a linear direction. We will see in Paper II how this condition is met in the actual design of the superconducting gradiometer.

It has been shown in Section B of this Appendix that the modulation of Earth's gravity by a time-varying displacement error $\delta\vec{\rho}(t)$ can be ignored because of the higher order gradients involved. The dominant mechanisms which convert the linear vibrations of the platform into gradiometer errors are therefore (1) the sensitive axes misalignment $\delta\hat{n}_-$, which couples the cross component accelerations, and (2) the scale factor mismatch $\delta\sigma_S(\omega)$, which couples the in-line component acceleration to the gradiometer output.

Combining proper terms in Eqs. (A6b) and (A18), one finds

$$\delta g_{d,\vec{a}}(\omega) = - [\delta \hat{n}_- + \delta\sigma_S(\omega)\, \hat{n}] \cdot \vec{a}(\vec{r},\omega) \ . \qquad \text{(A21)}$$

The two terms in this equation are related by the condition of the common mode balance. The balance is obtained in the real instrument by requiring $\delta g_{d,\vec{a}}(\omega_b) = 0$ for a given applied acceleration, say, in the z-direction:

$$\vec{a}(\vec{r},\omega_b) = a(\omega_b)\, \hat{z} \ . \qquad \text{(A22)}$$

Substitution of Eq. (A22) into Eq. (A21) leads to

$$\delta\sigma_S(\omega_b) = - \frac{\delta \hat{n}_- \cdot \hat{z}}{\hat{n} \cdot \hat{z}} + \delta\sigma_{S0}, \qquad \text{(A23)}$$

which can be substituted, in turn, into Eq. (A20) to obtain $\delta\sigma_S(\omega)$. Notice that, even with a wideband balance, $\delta\sigma_S(\omega) = \delta\sigma_S(\omega_b) \neq 0$ due to the misalignment of the sensitive axes and the residual balance error $\delta\sigma_{S0}$. The impossibility of obtaining a balance with an applied acceleration normal to $\hat{n}$, or $(\hat{n}_1 + \hat{n}_2)/2$ to be rigorous, is indicated by the divergence of Eq. (A23), which occurs when $\hat{n} \cdot \hat{z} = 0$.

G. Scale Factor Nonlinearity and Dynamic Range

A nonlinear behavior of accelerometer scale factors arises from departure of the acceleration response of the mechanical suspension springs from the linear behavior predicted by Hooke's Law, higher order terms in the modulation of the pancake coil inductances, L_a and L_b, higher order terms in the magnetic force F_{EM}, and, finally, nonlinearity in the current-to-voltage transfer

function of the SQUID electronics. In Eqs. (14), we assumed perfect linearity of L_a and L_b as functions of the coil spacing. This assumption is clearly not rigorous because of the grain structure of the pancake coils and edge effects. The higher order terms in F_{EM}, which are apparent in Eqs. (23) and (25), have been ignored in our attempt to linearize the circuit equations. Therefore, even if the mechanical springs and the SQUID electronics are constructed with sufficient linearity, the response of each accelerometer will be somewhat nonlinear due to the inevitable higher order response of the electrical circuit.

In analogy to Eqs. (A17), we define the nonlinearity error coefficients $h_{cc}(\omega)$, $h_{dd}(\omega)$ and $h_{cd}(\omega)$ by dividing the nonlinearity transfer functions $H_{Gi}^{cc}(\omega)$, $H_{Gi}^{dd}(\omega)$ and $H_{Gi}^{cd}(\omega)$, introduced in Eq. (101), by $H_{gi}^{d}(\omega)$. Then the equivalent differential acceleration error due to scale factor nonlinearity can be written as

$$\delta g_{d,N}(\omega) = h_{cc}(\omega)\, G_{cc}(\omega) + h_{dd}(\omega)\, G_{dd}(\omega) + h_{cd}(\omega)\, G_{cd}(\omega). \quad \text{(A24)}$$

Now, in most practical situations, the gravity terms are small compared to the platform motion terms in Eqs. (100) so that

$$G_{cc}(t) = [\hat{n} \cdot \vec{a}\,(\vec{r},t)]^2 , \quad \text{(A25a)}$$

$$G_{dd}(t) = \ell^2\, [\{\hat{n} \cdot \vec{\Omega}(t)\}^2 - \Omega^2(t)]^2, \quad \text{(A25b)}$$

$$G_{cd}(t) = \ell\, [\hat{n} \cdot \vec{a}\,(\vec{r},t)]\,[\{\hat{n} \cdot \vec{\Omega}(t)\}^2 - \Omega^2(t)]. \quad \text{(A25c)}$$

It is clear that the Fourier transformation of these nonlinear functions of dynamic variables will down-convert the wideband platform noise to the

vicinity of dc, where the gravity gradient signal is to be detected. Therefore, it is imperative that the vibration and jitter noise of the apparatus be low-pass filtered before they reach the gradiometer. Detailed analysis of the nooise down-conversion process will be given in Paper II.

It is difficult to determine the nonlinearity error coefficients analytically. They can however be measured from the departures of the transfer functions $H^c_{gi}(\omega)$ and $H^d_{gi}(\omega)$ from the linear behavior. In principle, the nonlinearity in the two component accelerometers could also be matched. This would not, however, reduce all three error coefficients in Eq. (A24) to zero. A more powerful and practical approach to the problem is the linearization of the system by means of an electromechanical feedback. A feedback force, which is equal and opposite to the detected external force, can be applied to each proof mass so that the total force, the "error signal" for the feedback loop, is reduced by the inverse of the feedback gain. The reduction of the driving accelerations limits the actual displacement of each proof mass to a small amplitude, thereby reducing $\delta g_{d,N}(\omega)$. The error coefficients $h(\omega)$'s have therefore been effectively reduced. The average and differential feedback forces are direct measures of $g_c(t)$ and $g_d(t)$. The gradiometer thus measures the specific force instead of the resulting displacement. The negative feedback comes with another important advantage: increase in the <u>dynamic range</u> of the device. This so-called "force rebalance" feedback has been successfully applied to conventional inertial navigation instruments [27] and gravity gradiometers [7], although it is yet to be applied to superconducting gravity gradiometers.

One of the parameters responsible for the high sensitivity of the superconducting gradiometer is the low damping coefficient of the electromechanical springs. The low dissipation is necessarily accompanied with high Q

resonances of the modes which tend to amplify the acceleration noise at the resonance frequencies. An elegant way to take care of this problem is an active damping method [28] by which the Q's are effectively lowered without increasing the Brownian motion noise level. The gradiometer response is narrowband filtered around the resonances, phase shifted by 90^{o}, and fed back to the proof masses to actively drive down the resonant motions. This "cold damping" has been successfully demonstrated in superconducting gravity gradiometers [13, 14].

H. Nonmechanical Noise of the Environment

It has been pointed out in the Introduction that superconductivity can be used to make a nearly perfect electromagnetic shield. In a practical superconducting shield with impurifies, the Meissner effect does not exclude the magnetic field completely, but instead "freezes" some trapped magnetic field, thus providing a "perfect" shield against time-varying fields. One can combine high permeability shields with superconducting shields to attenuate both dc and ac electromagnetic fields as well as radiation very effectively. Therefore, the electromagnetic susceptibility of the superconducting gradiometer can be made negligible.

The thermal fluctuations of the environment could also be shielded by immersing the apparatus in superfluid helium, the Bose condensate phase of He^4 below 2.17 K. The infinite heat conductivity and the large heat capacity of the superfluid provides a stable, gradient free, thermal environment. Even normal fluid helium can provide an excellent thermal environment provided its vapor pressure is regulated. When the attenuation of the temperature fluctuations of the environment is not sufficient, one will have error terms that couple the temperature noise to the gradiometer output, as shown in Eq. (101).

The fluctuation in the gradiometer temperature can cause error signals through its interaction with (1) the mechanical part and (2) the superconducting circuit.

In analogy to Eqs. (40), the temperature modulations of the two accelerometers, $T_1(\omega)$ and $T_2(\omega)$, are expressed in terms of their common and differential temperatures, $T_c(\omega)$ and $T_d(\omega)$:

$$T_1(\omega) = T_c(\omega) - \frac{1}{2} T_d(\omega), \tag{A26a}$$

$$T_2(\omega) = T_c(\omega) + \frac{1}{2} T_d(\omega). \tag{A26b}$$

The mechanically coupled temperature-induced error could arise simply from the thermal expansion of the baseline:

$$\frac{\delta \ell(\omega)}{\ell} = \alpha(T)\ T_c(\omega), \tag{A27}$$

where $\alpha(T)$ is the thermal expansion coefficient of the gradiometer body at the ambient temperature T. However, $\alpha(T)$ is extremely small for solids at liquid helium temperatures so that the dimensional change $\delta\ell(\omega)$ is negligible in any practical situation [14]. For the same reason, alignment changes $\delta\hat{n}_{\pm}(\omega)$ resulting from temperature fluctuations are negligible, demonstrating the mechanical stability of the cryogenic gravity gradiometer.

There is a more subtle coupling mechanism of the temperature noise through the mechanical part of the system. It is through the temperature dependence of Young's modulus E(T) of the mechanical spring [29]. Since the stiffness of the suspension spring changes as a function of temperature, a temperature fluctuation will cause a displacement modulation when the spring

is under stress either by gravity or by an unbalanced magnetic pressure. This can be seen in Eq. (25) for an accelerometer. When $\hat{n} \cdot \vec{g}_E(\vec{r}) \neq 0$ so that $x_o \neq 0$, the temperature induced modulation of ω_M^2 produces a first order effect in displacement. It is convenient to move this term to the righthand side of Eq. (25) and define an additional effective driving acceleration:

$$\delta g^T(t) = - [\omega_M^2(T + \delta T) - \omega_M^2(T)] \, x_o . \tag{A28}$$

The proportionality of the spring constant $m\omega_M^2$ to E(T) can be used to rewrite Eq. (A28) as

$$\delta g^T(t) = - \omega_M^2(T) \, x_o \, \frac{1}{E(T)} \, \frac{dE}{dT} \, \delta T(t) . \tag{A29}$$

Substitution of Eq. (27) into Eq. (A29) and Fourier transformation leads to

$$g^T(\omega) = \left[g_E \cos \theta_n + \frac{\Lambda}{m} \left(I + \frac{1}{2} \, \frac{L_a - L_b}{L_a + L_b} \, i \right) i \right] \frac{1}{E(T)} \, \frac{dE}{dT} \, T(\omega) . \tag{A30}$$

It is clear from this equation that this effect can be eliminated by choosing i such that the quantity in the square bracket vanishes; i.e., by compensating the gravitational force with a magnetic levitation force.

In the actual operation of the gradiometer reported in Paper II, $i \cong 0$ was chosen so that the magnetic pressure term in Eq. (A30) was negligible. The temperature effect on the gradiometer can be found then by adding

$$g_c^T(\omega) = g_E \cos \theta_n \, \frac{1}{E(T)} \, \frac{dE}{dT} \, T_c(\omega) , \tag{A31a}$$

$$g_d^T(\omega) = g_E \cos \theta_n \, \frac{1}{E(T)} \, \frac{dE}{dT} \, T_d(\omega) \tag{A31b}$$

to $g_c(\omega)$ and $g_d(\omega)$ in Eq. (41). It is assumed here that the two suspension springs of the proof masses have an identical Young's modulus E(T). The temperature-induced current output can be written as

$$i_d^T(\omega) = H_{Ti}^c(\omega)\ T_c(\omega) + H_{Ti}^d(\omega)\ T_d(\omega), \tag{A32}$$

where

$$H_{Ti}^c(\omega) = H_{gi}^c(\omega)\ g_E \cos\theta_n \frac{1}{E(T)} \frac{dE}{dT}\ , \tag{A33a}$$

$$H_{Ti}^d(\omega) = H_{gi}^d(\omega)\ g_E \cos\theta_n \frac{1}{E(T)} \frac{dE}{dT}\ . \tag{A33b}$$

Notice that the common temperature fluctuation $T_c(\omega)$ is balanced out to the same degree as the common acceleration. For a properly balanced gradiometer, therefore, this effect is expected to be negligible as long as $i \cong 0$.

The second effect of the temperature noise, which acts on the superconducting circuit directly, comes from the temperature dependence of the "penetration depth" $\lambda(T)$ of the magnetic field in the superconductor:

$$\lambda(T) = \frac{\lambda(0)}{[1 - (T/T_o)^4]^{1/2}}\ , \tag{A34}$$

where T_o is the critical temperature for the superconductor. For niobium, $\lambda(0) = 5.0 \times 10^{-8}$ m and $T_o = 9.2$ K. The variation of $\lambda(T_k)$ of the proof mass and pancake coils due to a temperature fluctuation $\delta T_k(t)$ of the k-th acceleration transducer,

$$\delta\lambda(T_k) = \lambda(T_k + \delta T_k) - \lambda(T_k) \simeq \frac{d\lambda}{dT}\ \delta T_k, \tag{A35}$$

modulates the superconducting inductances of Eq. (14) according to

$$L_{ka}(t) = L_{ka} + \Lambda(1 + \zeta)\ \delta\lambda(T_k) + \Lambda\ x_k^T(t)\ , \qquad \text{(A36a)}$$

$$L_{kb}(t) = L_{kb} + \Lambda(1 + \zeta)\ \delta\lambda(T_k) - \Lambda\ x_k^T(t)\ . \qquad \text{(A36b)}$$

Here,

$$0 < \zeta < 1 \qquad \text{(A37)}$$

is the modulation efficiency of the penetration depth of the pancake coils. Approximation is made here that the sensing inductances are reasonably well matched so that distinction of ζ for each of these coils is not necessary. In Eqs. (A36), $x_k^T(t)$ is the dynamic displacement produced in self-consistent response to the current modulations resulting from the temperature-induced inductance modulations. Given the penetration depth modulations, the displacement response $x_k^T(t)$ and the current response $i_d^T(t)$ are solved from the dynamical equations of the gradiometer. The dynamical equations and their solutions are modifications of those given in Section III.

Modifying Eqs. (18) and (19), the series and parallel inductances of the sensing coils L_{ka} and L_{kb} now becomes

$$L_{ks}(t) = L_{ks} + 2\ \Lambda(1 + \zeta)\ \delta\lambda(T_k), \qquad \text{(A38)}$$

$$L_{kp}(t) = L_{kp} + \frac{L_{ka}^2 + L_{kb}^2}{L_{ks}}\ \Lambda(1 + \zeta)\ \delta\lambda(T_k) - \frac{L_{ka} - L_{kb}}{L_{ks}}\ \Lambda\ x_k^T(t). \qquad \text{(A39)}$$

Flux quantization through the loops $L_{ka} + L_{kb}$ gives

$$I_k(t) = I_k \left[1 - \frac{2\Lambda(1 + \zeta)\ \delta\lambda(T_k)}{L_{ks}}\right]. \qquad \text{(A40)}$$

Substituting Eqs. (A38) - (A40) into the flux quantization condition for the loops $L_{kb}(t) + L_o$, which is generalized from Eq. (32), and taking Fourier transformation, one finds a modified version of Eq. (42):

$$x_k^T(\omega) + \alpha_k^T(1 + \zeta)\ \delta\lambda(T_k(\omega)) = \frac{L_{kp} + 2L_o}{\Lambda I_k'} \frac{1}{2} i_d^T(\omega) + (-1)^k \frac{L_{kp}}{\Lambda I_k'} i_c^T(\omega)\ , \qquad \text{(A41)}$$

where the coefficients α_k^T are defined by

$$\alpha_k^T \equiv \frac{L_{ka} - L_{kb}}{L_{ks}} + \frac{L_{kp}}{L_{ks}} \frac{i_k}{I_k'}\ . \qquad \text{(A42)}$$

The homogeneous part of Eq. (25) generalized for k = 1, 2 is then solved using Eqs. (A38) - (A40) again, resulting in

$$\left(-\omega^2 + \omega_{kM}^2 + \frac{\Lambda^2 i_k^2}{m_k L_{ks}}\right) x_k^T(\omega) + \frac{\Lambda I_k'}{m_k} \frac{1}{2} i_d^T(\omega) + (-1)^k \frac{\Lambda I_k'}{m_k} i_c^T(\omega)$$

$$= \frac{\Lambda^2(I_k' + I_k)\ i}{m_k L_{ks}} (1 + \zeta)\ \delta\lambda(T_k(\omega)), \qquad \text{(A43)}$$

which are identical to Eqs. (41) with the driving gravity signal replaced by the $\delta\lambda(T_k)$ term on the right hand side.

The relationships between the currents and $\delta\lambda$'s are obtained by eliminating x_k^T from Eqs. (A41) and (A43). The resulting pair of equations are the same as Eq. (43) on the lefthand side and have equal coefficients of $i_c^T(\omega)$ due to the common mode balance condition of Eq. (48). Therefore, the i_c^T terms are readily eliminated, yielding

$$i_d^T(\omega) = H_{gi}^d(\omega)(1 + \zeta)[\alpha_2^T (\omega_{2\lambda}^2 - \omega^2)\, \delta\lambda(T_2(\omega)) - \alpha_1^T(\omega_{1\lambda}^2 - \omega^2)\, \delta\lambda(T_1(\omega))], \tag{A44}$$

where

$$\omega_{k\lambda}^2 \equiv \omega_{kM}^2 + \frac{\Lambda^2 i_k^2}{m_k L_{ks}} + \frac{\Lambda^2(L_k' + L_k)\, i_k}{m_k\, \alpha_k^T\, L_{ks}} . \tag{A45}$$

The temperature induced output current can now be expressed in the form of Eq. (A32) with the identification:

$$H_{Ti}^c(\omega) = H_{gi}^d(\omega)\, h_{Tc}(\omega), \tag{A46a}$$

$$H_{Ti}^d(\omega) = H_{gi}^d(\omega)\, h_{Td}(\omega), \tag{A46b}$$

where the temperature error coefficients are obtained from Eqs. (A26), (A35) and (A44) as

$$h_{Tc}(\omega) = [\alpha_2^T(\omega_{2\lambda}^2 - \omega^2) - \alpha_1^T(\omega_{1\lambda}^2 - \omega^2)](1 + \zeta)\, \frac{d\lambda}{dT} , \tag{A47a}$$

$$h_{Td}(\omega) = \frac{1}{2}\, [\alpha_2^T(\omega_{2\lambda}^2 - \omega^2) + \alpha_1^T(\omega_{1\lambda}^2 - \omega^2)](1 + \zeta)\, \frac{d\lambda}{dT} . \tag{A47b}$$

In terms of these error coefficients, the <u>equivalent differential acceleration error due to temperature sensitivity</u> is

$$\delta g_{d,T}(\omega) = h_{Tc}(\omega)\, T_c(\omega) + h_{Td}\, T_d(\omega). \tag{A48}$$

It is apparent from Eqs. (A42) and (A47a) that the effect of $T_c(\omega)$ is

partially balanced by the match between pancake coil inductances, L_{ka} and L_{kb}, and by the common acceleration balance condition (48). On the other hand, $T_d(\omega)$ is usually negligible because the good thermal conductivity of the gradiometer body keeps the entire instrument in thermal equilibrium.

It has been pointed out [18] that an exact common temperature balance could be achieved by adjusting the fourth persistent current i_2 with respect to I_1, I_2 and i_1 that are used for the wideband common acceleration balance. The adjustments are iterated such that both the common acceleration balance condition (48) and the common temperature balance condition,

$$\alpha_2^T(\omega_{2\lambda}^2 - \omega^2) = \alpha_1^T(\omega_{1\lambda}^2 - \omega^2) \ , \qquad \text{(A49)}$$

are simultaneous satisfied. In practice, it will be easier to couple a separate superconducting loop, which senses only temperature, to the SQUID and adjust the persistent current in this loop to obtain the temperature balance. The advantage of the latter scheme is that the temperature and acceleration balances can be performed independently.

A slowly varying temperature of the environment, if uncompensated, can be an important source of a dc drift of the gradiometer. Such a drift, however, does not produce a random walk of the output, but the error is bounded because the dc level of the output is locked to the temperature of the gradiometer which is self-regulated to a large extent by the liquid helium itself.

REFERENCES

1. For a historical review of torsion balance experiments, see C.W.F. Everitt, in Proceedings of the First Marcel Grossmann Meeting on General Relativity, edited by R. Ruffini (North Holland, Amsterdam, 1978), p. 548.

2. For a historical introduction of room temperature gravimeters, see J.E. Faller, in Proceedings of the 1983 International School and Symposium on Precision Measurement and Gravity Experiment, edited by W.T. Ni (Chuan Wen Book Co., Hsinchu, Taiwan, 1983), p. 466.

3. J.M. Goodkind, Tectonophys. 52, 99 (1979).

4. J. Weber, Phys. Rev. 117, 306 (1960).

5. See a review by J.A. Tyson and R.P. Giffard, Annu. Rev. Astron. Astrophys. 16, 521 (1978).

6. R.L. Forward, in Proceedings of AIAA Unmanned Spacecraft Meeting (Los Angeles, California, 1965), p. 346.

7. E.H. Metzger and D.R. Allen, Report 9500-92044, Bell Aerospace Co., Buffalo, New York (1972).

8. M.B. Trageser, in Proceedings of the First International Symposium on Inertial Technology for Surveying and Geodesy (Ottawa, Canada, 1977).

9. H.J. Paik, J. Appl. Phys. 47, 1168 (1976).

10. Spaceborne Gravity Gradiometers, NASA Conference Publication 2305, edited by W.C. Wells (1984).

11. J.W. Parke, H.J. Paik, H.A. Chan and M.V. Moody, in Proceedings of the Tenth International Cryogenic Engineering Conference, edited by H. Collan et al (Butterworth, Guildford, 1984), p. 361.

12. H.J. Paik, E.R. Mapoles, and K.Y. Wang, in Proceedings of Conference on Future Trends in Superconductive Electronics, edited by B.S. Deaver et al (Charlottesville, Virginia, 1978), p. 166.

13. K.Y. Wang, Ph.D. thesis, Stanford University, Stanford, California (1979), unpublished.

14. E.R. Mapoles, Ph.D. thesis, Stanford University, Stanford, California (1981), unpublished.

15. H.J. Paik, J. Astronaut. Sci. 29, 1 (1981).

16. H.J. Paik, IEEE Trans. Geoscience and Remote Sensing, GE-23, 524 (1985).

17. H.A. Chan, M.V. Moody and H.J. Paik, Phys. Rev. Lett. 49, 1745 (1982).

18. H.A. Chan, Ph.D. thesis, University of Maryland, College Park, Maryland (1982), unpublished.

19. K.R. Symon, Mechanics, 2nd edition (Addison-Wesley, Reading, 1961), p. 278.

20. H.J. Paik, Phys. Rev. D19, 2320 (1979).

21. The term "acceleration signal" hereafter refers to the specific force $\vec{g}'(\vec{r},t)$ defined in Section II.

22. The term "spectral density" refers to a one-sided spectral density in Papers I and II unless specified otherwise.

23. J.N. Hollenhorst and R.P. Giffard, J. Appl. Phys. 51, 1719 (1980).

24. M.V. Moody, H.A. Chan, H.J. Paik, and C. Stephens, in Proceedings of 17th International Conference on Low Temperature Physics, edited by U. Eckern et al, (North-Holland, Amsterdam, 1984), p. 407.

25. H.A. Chan, M.V. Moody, H.J. Paik, and J.W. Parke, in Proceedings of 17th International Conference on Low Temperature Physics, edited by U. Eckern et al, (North-Holland, Amsterdam, 1984), Vol. 2, p. 927.

26. H.J. Paik, Bull. Geod. 55, 370 (1981).

27. C. Broxmeyer, Inertial Navigation Systems (McGraw-Hill, New York, 1964).

28. C. Kittel, Elementary Statistical Physics (Wiley & Sons, New York, 1958), p. 141-156.

29. J.W. Parke, H.J. Paik, E.R. Mapoles, W.M. Fairbank and D. DeBra, paper in preparation.

PART 2

DEVELOPMENT OF A PROTOTYPE SINGLE-AXIS SUPERCONDUCTING GRAVITY GRADIOMETER

SUPERCONDUCTING GRAVITY GRADIOMETER FOR SENSITIVE GRAVITY MEASUREMENTS: II. EXPERIMENT*

H.A. Chan, M.V. Moody and H.J. Paik
Department of Physics and Astronomy
University of Maryland, Collge Park, MD 20742

A sensitive superconducting gravity gradiometer has been constructed and tested. Coupling to gravity signals is obtained by having two superconducting proof masses modulate magnetic fields produced by persistent currents. The induced electrical currents are differenced by a passive superconducting circuit coupled to a SQUID (Superconducting QUantum Interference Device). The experimental behavior of this device has been shown to follow the theoretical model closely in both signal transfer and noise characteristics. While its intrinsic noise level is shown to be 0.07 E $Hz^{-1/2}$ (1 E $\equiv 10^{-9}$ s^{-2}), the actual performance of the gravity gradiometer on a passive platform has been limited to 0.3 ~ 0.7 E $Hz^{-1/2}$ due to its coupling to the environmental noise. The detailed structure of this excess noise is understood in terms of an analytical error model of the instrument. The calibration of the gradiometer has been obtained by two independent methods: by applying a linear acceleration and a gravity signal in two different operational modes of the instrument. This device has been successfully operated as a detector in a new null experiment for the gravitational inverse square law. In this paper, we report the design, fabrication and detailed test results of the superconducting gravity gradiometer. We also present additional theoretical analyses which predict the specific dynamical behavior of the gradiometer and of the test platform, and compare the results with experiments.

*Work supported by NASA under contract No. NAS 8-33822.

I. INTRODUCTION

The Equivalence Principle prohibits distinction of "gravity" from "acceleration" by a local measurement. The same principle, however, implies that a sensitive accelerometer, or a gravimeter, can be used as an approximate detector of gravity in an environment where the platform accelerations are small. Thus, gravimeters, which measure absolute and relative magnitudes of the gravitational acceleration vector, usually from a stationary platform, have been employed as geophysical survey instruments [1]. This method of measuring gravity can be extended to a moving platform by independently determining and compensating for the platform accelerations with the aid of a geodetic navigation device such as the Global Positioning System (GPS) satellite network [2]. The latter measurement is clearly of a global nature.

An alternative, more direct, approach to a rigorous determination of the gravitational field is by means of a gravity gradiometer, which measures components of the tidal force or the Riemann tensor [3]. Here an almost local measurement is made by monitoring relative motions of proof masses separated by a short, but finite, baseline. With the torsion balance as the predecessor, several advanced types of gravity gradiometers have been developed recently [4].

The superconducting gravity gradiometer, to be discussed in this paper, has been developed with the primary motivation being to perform precise tests of gravitational theories in both terrestrial and space laboratories. A preliminary version of a null test of the gravitational inverse square law has been carried out with this instrument [5]. While the instrument has served as a prototype for a three-axis superconducting gravity gradiometer [6] which is under construction, the system has undergone a thorough theoretical and experimental analysis to test the physics of the instrument. The results could

easily be adapted to a more complicated device.

In Paper I, a detailed theoretical analysis of the current-differencing gravity gradiometer was presented. This paper (Paper II) discusses the design, construction and test results of the actual instrument. These test results demonstrate that the physical device is described by the theoretical model in great detail. In addition, we discuss here the principle and operation of two elegant experimental techniques, which have been applied to the superconducting gravity gradiometer: (1) accelerometer mode calibration and (2) vibration isolation by means of pendulum action. Also, the error model of the instrument developed in Paper I is extended and applied here to the specific instrument configuration chosen. Paper II represents an extension of the experimental work reported in Ref. 7.

The gravity gradient signal sought for is usually a small fluctuation over a relatively large background of the Earth's gravity and the seismic activity of the platform. Therefore, precise mechanical alignment of components and extreme stability of scale factors, as well as high sensitivity, are required for a practical gravity gradiometer. Advantages of a superconducting instrument in these regards have been pointed out in Paper I. In this paper, we show how quantum-mechanical properties of superconductors are utilized specifically, along with careful mechanical design, to meet the challenge of constructing a highly sensitive gravity gradiometer.

Notations employed in Paper II follow those of Paper I, unless explicitly stated otherwise.

II. DESIGN AND FABRICATION OF THE SUPERCONDUCTING GRAVITY GRADIOMETER.

A. Gradiometer Hardware

The gradiometer consists of two accelerometers, each with a proof mass, a suspension structure, and sensing coils. The suspension structure consists of mechanical springs which confine the proof mass motion along the desired direction.

A folded cantilever suspension has been employed to produce a suspension with a linear spring constant which is weak, in the direction of motion, yet relatively rigid for other degrees of freedom. This type of suspension was suggested by Prof. Daniel DeBra at Stanford University and has been employed in the displacement-differencing gravity gradiometer [8]. The design contains eight folded cantilevers in an $\bar{8}m$ symmetry (to be defined later) to suspend the proof mass at the center (Fig. 1). Each cantilever consists of three joined diaphragm strips, of length ℓ_s and thickness t_s, formed at the bottom of one radially oriented groove. The "fold" of the cantilever is at the radially outward ends of the strips. The radially inward ends of the strip are the ends of the spring. The middle strip of width b_s holds the center moving mass. The other two strips of width $\frac{1}{2}\, b_s$ link to a bulk mass which is a solid continuation of the outer rim of the suspension. This design allows the cantilevers to undergo pure bending without stretching in order to achieve linearity in the spring constant. There are four folded cantilevers on each of two parallel planes with $2\pi/8$ rotation plus inversion symmetry ($\bar{8}m$ symmetry). Thus, motion of the center mass is linearized along the cylindrical axis.

The entire suspension structure is machined out of a single piece of niobium (Nb) in order to insure mechanical precision and to obtain a high

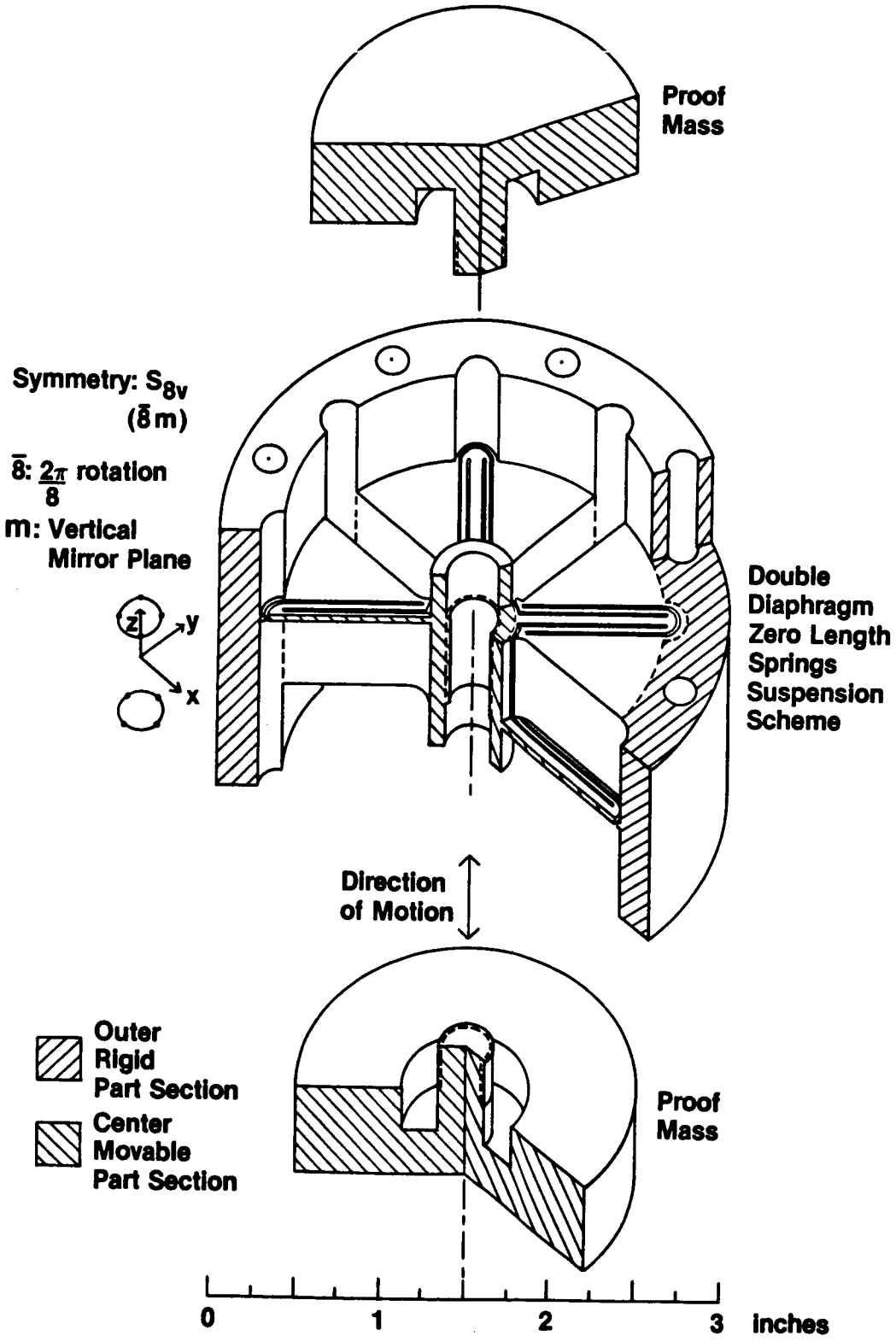

Fig. 1. A cut-away view of proof mass suspension.

quality factor of resonance. Eight grooves, four from each side, are first milled out, leaving a thick diaphragm at their opposite sides. The metal is then stress-relieved at 800°C. The grooves are then electric-discharge-machined (EDM) to thicknesses of (0.35 ± 0.01) mm. Next, the suspension structure is chemically polished with a mixture of hydrofluoric acid (HF), phosphoric acid (H_3PO_4) and nitric acid (HNO_3) in an ultrasonic cleaner. After the polishing, the Nb is partially recrystalized by annealing in a vacuum oven at 1100°C. The designed pattern of slots is then cut with a wire EDM. Finally, the finished proof mass suspension structure is chemically polished again.

The center moving mass of the suspension is loaded with two mushroom-shaped Nb masses which screw into opposite ends to form one proof mass. This added load serves to increase the mass m_k, lower the suspension frequency f_{kM}, and provide two superconducting planes which modulate the inductances of the sensing coils. The mechanical suspension frequency of the proof mass is derived from the formula for a loaded beam and is given by

$$\omega_{kM}^2 = (2\pi f_{kM})^2 = \frac{E_s\, b_s\, t_s^3}{2\,(m_k/n_s)\,\ell_s^3}\,. \qquad (1)$$

Here $E_s = 1.03\times10^{11}$ N m^{-3} is the Young's modulus of Nb and $n_s = 8$ is the number of springs used. Also, $t_s = 0.35$ mm, $\ell_s = 19$ mm, $b_s = 2.5$ mm, and $m_k = 0.40$ kg, giving $f_{kM} \simeq 20$ Hz.

The sensing inductors are "pancake-shaped" coils wound out of thin (0.076 mm in diameter) Nb wire in a single layer. The coil form is made of machinable glass-ceramic, Macor (Corning Glass Works, Corning, New York), whose thermal expansion coefficient matches closely with that of Nb down to cryogenic temperatures. A continuous length of insulated Nb wire is wound uni-

formly on the flat coil form in a spiral shape. Low viscosity, transparent, TRA-CAST BB3002 epoxy (TRA-CON, Inc., Medford, Massachusetts) is used to bond the Nb wire. The coil winding procedure used here is a modification of that described in Ref. 9.

Two such pancake coils are located next to the two plane surfaces of the proof mass in each accelerometer. To a high accuracy, the inductance for each pancake coil,

$$L(t) = \mu_0 \, n_0^2 \, A_L \, [d + x(t)] \, , \qquad (2)$$

changes linearly according to its average spacing from the superconducting ground plane, and is insensitive to any rocking or transverse modes of the proof mass. The coil forms are mounted rigidly on Nb holders using Nb screws and GE 7031 varnish. The two Nb holders are mounted rigidly to the outer rim of the proof mass suspension using titanium (Ti) screws to form a shielded accelerometer. Ti is closely matched in thermal expansion coefficient with Nb. The spacing between the coil and the proof mass is adjusted by adding Nb spacers cut out of Nb sheet. Parallelism between the coil and proof mass surface is desirable to allow the use of a small spacing between them.

Two accelerometers are mounted on the opposite faces of a precision Ti (Ti V4 Al6 alloy) cube to form a single-axis gradiometer (see Fig. 2). The surfaces of the cube have parallelism and orthogonality within 50 ppm. The same degree of parallelism is kept for the mating surfaces of all the gradiometer parts. The Ti material at the center cube is continued down to an aluminum-to-titanium joint. An aluminum (Al) base is tight fitted onto the Ti at room temperature. Differential contraction tightens the joint further as the assembly is cooled down. A similar joint is made at the upper end. The

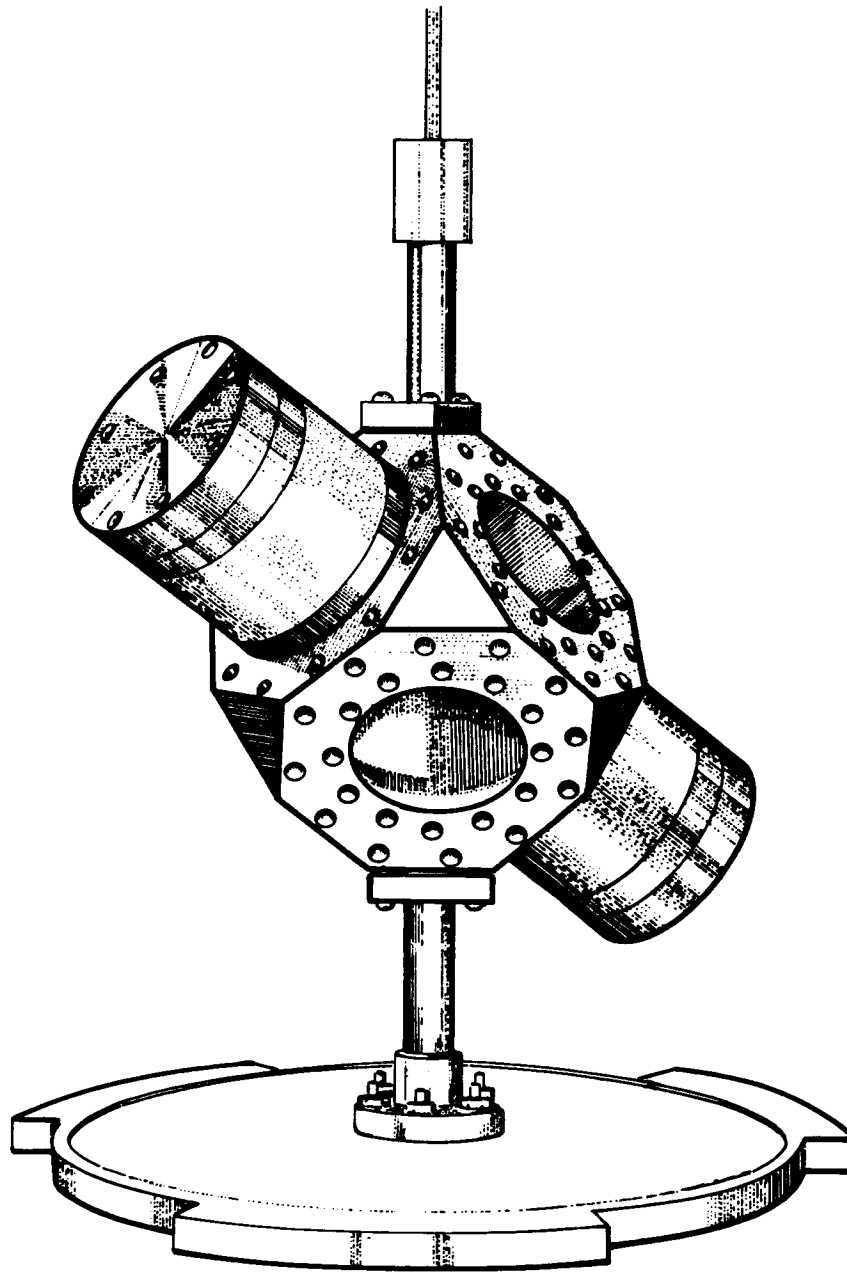

Fig. 2. A perspective view of the single-axis gradiometer in umbrella orientation.

baseline of the gradiometer, which is defined by the distance between the centers of mass for the two proof masses, is $\ell = 0.16$ m.

For most of the tests reported in this paper, one triagonal axis of the mounting cube is aligned with the vertical, as is shown in Fig. 2, so that the sensitive axis of the gradiometer is tilted by an angle

$$\theta_u = \tan^{-1} \sqrt{2} \qquad (3)$$

from the vertical. This "umbrella orientation" has the advantage of allowing measurements in three orthogonal directions to be made by rotating the gradiometer around the vertical axis by 120° increments. The fact that the large dc gravity bias is matched along the sensitive axes is an important scientific reason to prefer this orientation when a careful three-axis measurement is called for. The above procedure has therefore been used for the null test of the gravitational inverse square law [5], which will be discussed in Section VI.

B. Superconducting Circuitry

The superconducting circuit for the gradiometer is shown in Fig 3. L_{1a}, L_{1b}, and L_{2a}, L_{2b} are pancake coil inductors for the two proof masses, m_1 and m_2, respectively. S_{1a}, S_{1b}, S_{2a}, S_{2b} and S_I are current leads from the current supply outside the cryostat. H_1, $H_{1\delta}$, H_2, and $H_{2\delta}$ are shielded heat-switch resistors. When currents are sent through these resistors, appropriate sections of the superconducting path are switched into their normal state. $R_{1\delta}$ and $R_{2\delta}$ represent extremely low resistance current paths (3×10^{-9} Ω). L_i is the input inductor of the SQUID amplifier. L_I and L_{II} are, respectively, the primary and secondary of a high coupling transformer.

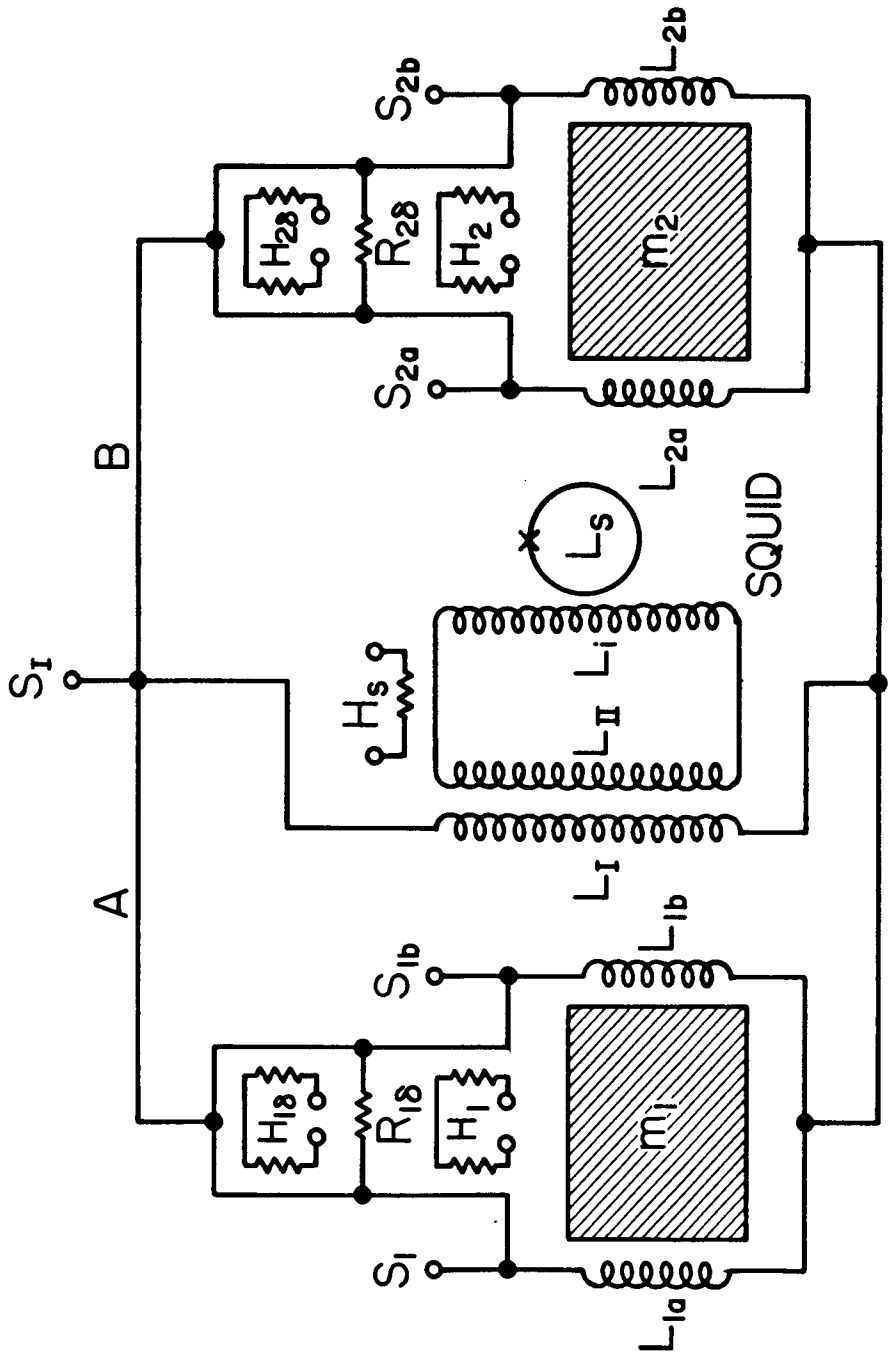

Fig. 3. The superconducting circuit for the gravity gradiometer.

The current I_1 can be stored in $L_{1a} + L_{1b}$ by turning H_1 on and then off while the current is sent across S_{1a} and S_{1b}. The inductance $L_{1a} + L_{1b}$ can be determined by measuring the flux trapped in it after a known current has been stored. The flux is measured by the time integral of the voltage decay across the leads S_{1a} and S_{1b} as H_1 is turned on. This method has been described in Ref. 9. There is also a heat-switch, H_S, between L_{II} and L_I that will be turned on in all operations involving current changes. This heat-switch serves to protect the Josephson junction of the SQUID ring against any surge current induced in the input coil L_I. The currents I_1 and I_2 in the two sensing loops can be fine tuned by letting the stored flux leak very slowly across an ultra low resistance path after a section of the superconducting path has been turned normal. If the heat-switch $H_{2\delta}$ is turned on, the current I_2 in $L_{2a} + L_{2b}$ will decay across $R_{2\delta}$ with a decay time $\tau = (L_{2a} + L_{2b})/R_{2\delta} \cong 3 \times 10^4$ s, which is extremely long. This current will rise or decay even more slowly if a second current, slightly greater or smaller than I_2, is being sent across the leads S_{2a} and S_{2b} while $H_{2\delta}$ is kept on. An additional current i_1 can be added in the loop formed by a parallel combination $L_{1a}//L_{1b}$ and L_I (see Fig. 3 of Paper I) by turning both $H_{1\delta}$ and $H_{2\delta}$ on and then off while a current is sent across S_I and either S_{1a} or S_{1b}. The decay of I_1 and I_2 during the time required to store i_1 is negligible because of the long decay time τ. The directions of these persistent currents are as defined in Fig. 3 of Paper I.

The superconducting circuit is shielded inside Nb. The outer surfaces of the Nb holders for sensing coils are shielded with additional Nb covers to form junction boxes. Circuit components such as superconducting joints, a superconducting transformer, shielded heat-switches and ultra low-value resistors are mounted in these junction boxes.

The superconducting joints and transformers are similar to those used in

References 9 and 10. A pair of Nb lead wires to be joined are twisted together, wrapped around a brass screw, sandwiched between two Nb sheets, and clamped together under a brass washer. They are clamped hard by tightening the brass screw into a piece of insulated brass block. The Nb wires are chemically cleaned with concentrated HNO_3 before they are joined. Flatness and parallelism of the brass block surface relative to the screw head surface is found helpful for making very tight joints without breaking the thin Nb wires. A fresh section of the lead wire is used to make the joint. Joints made this way consistently have critical currents in excess of 3 A through several thermal cycles [11]. The transformer makes use of a Nb sheet to guide the magnetic field through the primary and secondary coils.

Shielded heat-switches are made with a small cylindrical Nb cup which shields the superconducting circuit from the noise of the heater resistor. The heater element is a small 500 Ω Allen-Bradley resistor which is glued with GE 7031 varnish inside the Nb cup. Shielding from the resistor is continued with superconducting lead-tin (PbSn) tubing which starts from inside the Nb cup to enclose the lead wires of the heater. The sections of Nb wire to be affected by the heat-switch are wound non-inductively on the outside surface of the Nb cup and are glued with the GE varnish. The cup is then glued on a piece of fiberglass which is held rigidly inside the junction box. The Nb wires from the heat-switches are heat-sunk to the Nb mass of the junction box.

The shielding of the heat-switches provides significant improvement in preventing electrical pickup and rf interference at the input of the SQUID amplifier. The shielding has a drawback, though, in possessing a higher heat capacity which prolongs the response time of the heat-switch. By making the heat-switch compact, we managed to obtain an on/off response time of about 0.2 s with 4 mW supplied to the heater.

The ultra low-resistance heat-switch makes use of the radial conduction across a very thin cylindrical wall of copper. We simply solder two lengths of copper-clad Nb wires together with PbSn solder. The copper coating gives extremely low resistance between the superconducting PbSn on its outside wall and the Nb wire inside. The resistance between the two Nb wires comes from two such resistors connected in series. This resistance is given by the formula:

$$R_\delta = \frac{\rho_{Cu}(4.2\ K)}{\pi\, \ell_{Cu}} \ln \frac{r_{Cu}}{r_{Nb}} \,. \qquad (4)$$

We used Nb wire of diameter $2r_{Nb} = 0.128$ mm with copper coating which gives an overall diameter of $2r_{Cu} = 0.166$ mm. The resistivity of copper at 4.2 K is $\rho_{Cu} \cong 10^{-9}\ \Omega$ m. Therefore, when a wire of length $\ell_{Cu} = 10$ mm is used, we obtain $R_\delta \cong 10^{-8}\ \Omega$. This resistance has been verified in a decay time measurement of magnetic flux. The other two ends of the copper-clad Nb wires have their copper layer removed with concentrated HNO_3 so that superconducting joints can be made there. In the rest of the superconducting circuit, Nb wires without copper coating are used to avoid ac losses due to eddy currents [9].

In the original circuit used for tests, an additional SQUID was coupled to the superconducting circuit to measure the common acceleration simultaneously. Two identical superconducting transformers were inserted into the paths that connect the two sensing loops to L_I (A and B in Fig. 3), with one on each accelerometer side. The primaries of these transformers completed the gradiometer circuit. Their secondaries were connected in series with the input coil of the second SQUID. The current induced in this loop was proportional to the sum of the signal currents from the two accelerometers, per-

mitting a simultaneous readout of the common acceleration in the "gradiometer mode". Although such a readout is useful for error compensation and active vibration isolation [12], we have omitted, for simplicity, this additional circuit in the later tests in favor of the basic circuit shown in Fig. 3.

III. CONSTRUCTION AND PERFORMANCE OF TEST APPARATUS

A. Mechanical and Thermal Design of Experimental Space

The superconducting gravity gradiometer is operated in a very quiet cryogenic vacuum space with a stable temperature. A low boil-off liquid helium (He) dewar was designed and constructed with great care. Radiation shields with superinsulation are used in preference to a liquid nitrogen (N_2) shield, because boiling liquid N_2 is a much noisier source of vibration than boiling liquid He. Pressure pads are sandwiched near the bottom of the dewar between the fiberglass inner tube and the sturdy outer Al wall. The relatively weak inner tube is then damped against swinging motions. The inside dimensions of the dewar are 0.378 m in diameter and 1.778 m in height.

A low heat-leak insert has been constructed to complement the dewar. An Al vacuum can is supported by three equally spaced fiberglass tubes and one center fiberglass tube which permits access to the vacuum space from the dewar top. The vacuum space is 0.33 m in diameter by 0.61 m in height. The can remains totally submerged for one week with 60 liters of liquid He. A long hold-time of He is needed for an uninterrupted operation of sensitive measurements. The low boil-off rate is also important for lower boiling noise from the He and for lower thermal drift of the experiment.

For most of the experiment, the gradiometer assembly was suspended inside vacuum by means of a fiberglass rod from the room temperature end of the dewar insert. All the lead wires are heat-sunk in liquid He before they enter the vacuum space through specially made feedthroughs. In this setup, long term temperature variations of the gradiometer assembly over many weeks average about 10 mK. In a time scale of several hours, the temperature variations are within the 2 mK resolution of a germanium (Ge) resistance thermometer mounted

on the gradiometer. The heat capacity of the gradiometer and the weak thermal coupling to the He bath form a low-pass filter for the temperature fluctuations between the gradiometer and the He bath. The response time is estimated to be on the order of minutes.

B. Electromagnetic Shielding

External magnetic field fluctuations and electrical pickup can produce a high noise level in comparison with the very weak gravitational force. Rf interference will also deteriorate the noise performance of the rf SQUID and can unlock the SQUID feedback loop. The first stage of magnetic field isolation is provided by a double wall mu-metal shield which surrounds the cryostat. Two additional superconducting stages of magnetic shielding are provided by a 1 μm lead (Pb) film evaporated on the inner wall of the vacuum can, and by the Nb body of the gradiometer itself. Also, the Al walls of the dewar and the vacuum can aid in shielding high frequency electromagnetic radiation.

The success of the electromagnetic shielding is evidenced by the achievement of the optimum SQUID amplifier noise when the SQUID input is coupled to the gradiometer at full sensitivity. The magnetic shielding has also been tested when the gradiometer is balanced. A magnet producting 600 Gauss being flipped just outside the dewar produced a response less than an equivalent flux change of $2\times10^{-3}\ \Phi_0$ or 4×10^{-18} Wb at the SQUID input.

Each current lead for storing a supercurrent has an inductive choke inside the vacuum can. The choke is a high-impedance path to attenuate the electrical noise that the wire can pick up outside the Pb shield and especially outside the dewar. The other leads pass through two stages of rf filters, one inside the Pb shield and the other outside it. The outside one is an RC low-pass filter with the manganin wire down the dewar providing the

resistance and the inside one is a capacitor in parallel with the load.

C. Vibration Isolation

Vibration proved to be the most troublesome source of noise. The test of the gradiometer has therefore been conducted in a deep underground laboratory, which is secluded from the traffic of people. The most critical noise data have been obtained in the evenings to minimize the mechanical and electrical disturbance of the experiment. In spite of these precautions, the gradiometer required careful mechanical isolation from the environment.

The vibration isolation system consists of a three stage low-pass filter schematically shown in Fig. 4. The gradiometer assembly is suspended by a fiberglass rod and a length of latex rubber tubing in vacuum which form the first stage of vibration isolation. The vacuum is extended above the top of the dewar insert by means of a thick-wall plexiglass tube. The rubber tubing inside this plexiglass tube hangs from a connecting rod which is attached to a massive brass plate that seals with the plexiglass at the top. The height of the connecting rod can be adjusted from outside the vacuum so that the gradiometer can be lowered to the bottom of the vacuum can to short out the filter. When the gradiometer is suspended by the rubber tubing, the vertical resonance frequency is 0.9 Hz.

The fiberglass and rubber also give wideband isolation from tilt noise. The gradiometer suspended by a long fiberglass rod constitutes a pendulum. A natural property of a pendulum is its tendency to align itself along the direction of gravity. The gradiometer is therefore decoupled from a crucial error source: the ground tilt, which would cause an error signal due to modulation of Earth's gravity for a hard-mounted gradiometer.

Another important property of the pendulum is that the mass at the end of

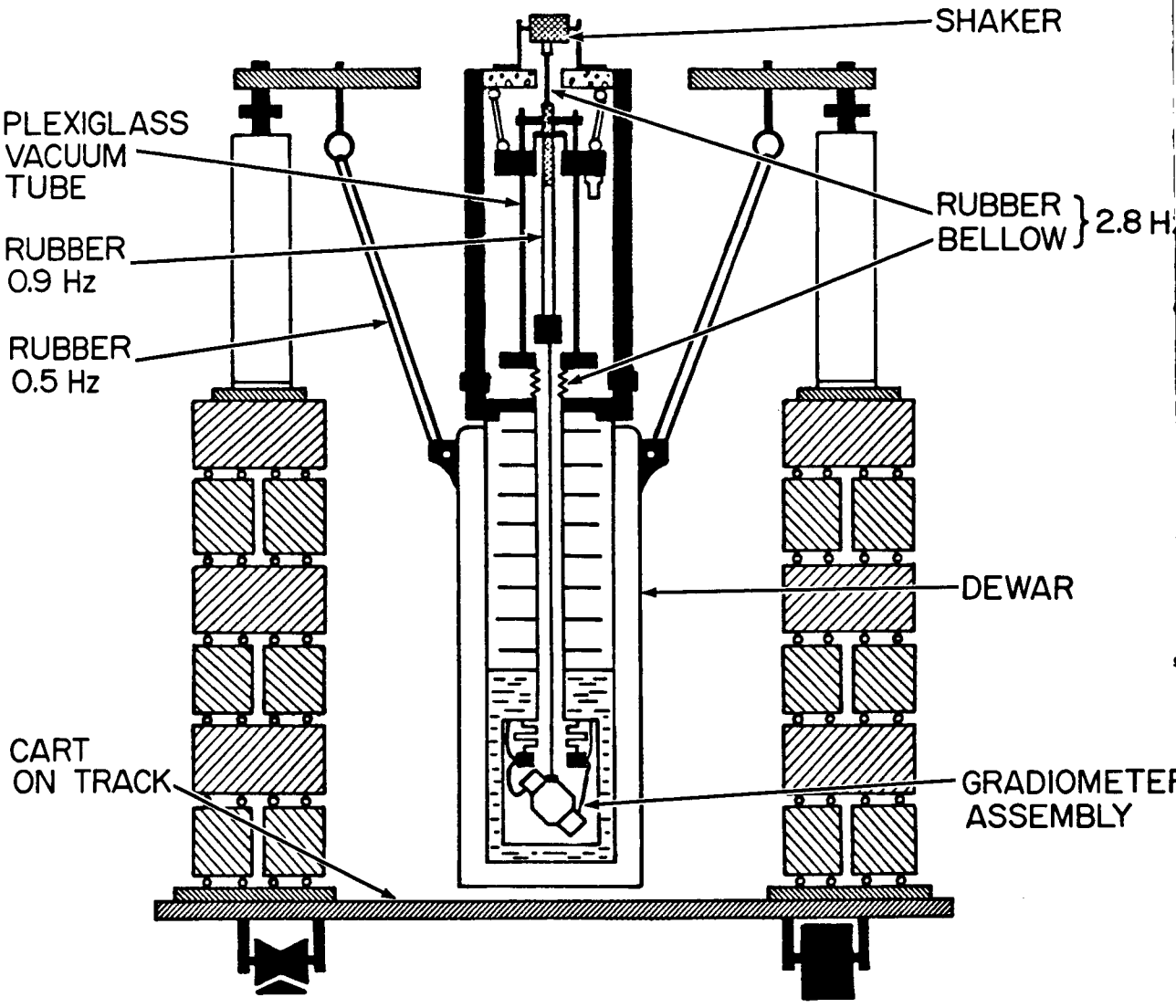

Fig. 4. Three-stage vibration isolation system.

the rod is under a two-dimensional "free fall" in the horizontal plane. An accelerometer mounted on the pendulum bob therefore cannot experience any horizontal acceleration relative to the platform to the first order. A gravity gradiometer can, however, couple to the angular velocity and the angular acceleration which result from the pendulum response to the horizontal acceleration (see Section V and Appendix A for detailed discussions of the pendulum action). The net effect of the pendulum action for the horizontal vibration is that of a low-frequency filter, in series with a wideband attenuator.

Additional resonant modes of the suspension structure can deteriorate vibration isolation at the resonance peaks. In spite of these limitations, we have chosen the pendulum suspension for the gradiometer because of its isolation characteristic for low frequency horizontal acceleration and its simplicity in construction. The pendulum frequency (swinging mode) is approximately 0.3 Hz and the rubber tubing gives a torsional mode at 0.08 Hz. In addition, the massive gradiometer suspended by the long and therefore bendable fiberglass rod gave a troublesome high-Q peak at 2.5 Hz. This peak was the result of a rocking mode of the gradiometer assembly around a horizontal axis.

The massive brass top of the plexiglass column is suspended with a set of rubber tubings. The bottom of the plexiglass column is connected to the top of the dewar insert by a flexible vacuum bellows. The rubber tubing and this bellows form the second stage of the filter with a vertical resonance frequency of 2.8 Hz. This filter can be shorted out by connecting clamps across the bellows.

The third stage of the filter is formed by three sets of rubber tubings that lift the dewar off the floor. The dewar is suspended from a framework by these rubber tubings and has a vertical resonance frequency of 0.5 Hz and a

swinging frequency of 0.3 Hz. The upper joints of the rubber tubings in this suspension are adjustable so that the dewar can be levelled. Again, this filter can be eliminated by lowering the dewar to the cart.

The advantages of using latex tubing as a passive filter are its high elasticity and low Q. A latex tubing of initial length ℓ_i can be extended to a final length ℓ_f which is a few times ℓ_i. The cross-sectional area will decrease from A_i to $A_f = A_i(\ell_i/\ell_f)$ in order to keep the volume constant. We assume that the modulus of elasticity is approximately constant even with such large extension. One can easily show then that the vertical resonance frequency is

$$f = \frac{1}{2\pi}\left(\frac{g_E}{\ell_f - \ell_i}\right)^{1/2}\left(\frac{\ell_i}{\ell_f}\right)^{1/2}, \qquad (5)$$

where ℓ_f is the new length determined by gravity g_E acting on the load. The factor $(\ell_i/\ell_f)^{1/2}$ corrects for a change in the cross-sectional area as the rubber elongates. By having large extension $\ell_f - \ell_i$, a low resonance frequency is obtained. The low Q provides self damping of the own resonance of the filter. Our latex tubing suspending the gradiometer in vacuum has $Q \approx 10$.

The disadvantages of rubber are in relaxation and drift which worsen as the latex extends. A compromise is to keep $\ell_f \lesssim 2\ell_i$. We used $\ell_f \approx 1.6\,\ell_i$ for the rubber inside vacuum. Over a period of three months under load, it stretched by an additional 3 cm.

IV. GRADIOMETER PARAMETER MEASUREMENTS AND CIRCUIT OPTIMIZATION

A. Determination of Geometric Asymmetry

The main asymmetries between the two component accelerometers in a gradiometer come from the spacings of the sensing coils and mechanical spring constants. A high degree of matching for these parameters was not attempted because the mismatch can be compensated for by supercurrents. As can be shown from Section III of Paper I, the low frequency common mode balance condition in the small stored current limit with only two currents I_1 and I_2 reduces to

$$\frac{L_{2b}//L_{2a}}{L_{1b}//L_{1a}} \frac{\omega_{2M}^2}{\omega_{1M}^2} = -\frac{I_2}{I_1} . \qquad (6)$$

The currents I_1 and I_2 can therefore be adjusted to compensate for the mechanical asymmetry, and the ratio I_2/I_1 thus obtained measures the original asymmetry before it was balanced. We shall determine the ratios on both sides of Eq. (6) to check against the theory. This check will also indicate how good a "symmetric component-accelerometer approximation" is. Such an approximation shall often be used later for simplicity.

The parameters measured in a particular cool-down are summarized in Table 1. The uncoupled mechanical frequencies of the proof masses were measured at 4.2 K with the gradiometer assembly firmly attached to an effectively infinite mass platform. This platform is simply the dewar and the ground. We have measured $\omega_{2M}^2/\omega_{1M}^2 = 0.92$, and the mass ratio m_2/m_1 is estimated to be close to unity. Therefore, the ratio of the measured mechanical frequencies reflects the mismatch in the spring constants for the two proof masses.

The experimental values of the various inductances shown in the circuit diagram of Fig. 3 can be measured only when the system becomes superconduc-

Parameter	Symbol	Value
Mass of each proof mass	m_k	0.40 kg
Mass of gradiometer assembly	M	7.7 kg
Mass ratio	m_k/M	0.052
Mechanical proof mass frequency	$\bar{f}_{kM}$	19 Hz
Mechanical spring constant ratio	$\omega_{2M}^2/\omega_{1M}^2$	0.92
Gradiometer Baseline	ℓ	0.16 m
Pancake coil area	A_L	2019 mm^2
Pancake coil wire density	n_L	11 mm^{-1}
Inductance per spacing	$\Lambda \equiv \mu_0 n_L^2 A_L$	0.306 H m^{-1}
Coil-to-proof-mass spacing	$\bar{d}_L$	0.14 mm
Inductance of one coil	$\bar{L}$	42 μH
Measured coil spacing asymmetries	$\frac{L_{1b} - L_{1a}}{L_{1b} + L_{1a}}$	0.15
	$\frac{L_{2b} - L_{2a}}{L_{2b} + L_{2a}}$	0.34
Sensing loop asymmetry	$\frac{L_{2b} \,//\, L_{2a}}{L_{1b} \,//\, L_{1a}}$	0.91
Geometric asymmetry factor	$\frac{L_{2b} \,//\, L_{2a}}{L_{1b} \,//\, L_{1a}} \frac{\omega_{2M}^2}{\omega_{1M}^2}$	0.83

Table 1. Experimental parameters of the gravity gradiometer

ting. The method of stored flux measurement described in Section IIB was employed to measure various loop inductances. The measured series inductances $L_{1b} + L_{1a}$ and $L_{2b} + L_{2a}$ agree with the inductances calculated from Eq. (2).

In order to measure the individual inductances or the parallel inductance $L_{ka}//L_{kb}$, we used an acceleration-response method to measure the ratios L_{1b}/L_{1a} and L_{2b}/L_{2a}. This method does not require knowledge of the behavior of L_0. A very small stored current is used so that negligible shifts are produced in the equilibrium position of the proof mass and in the proof mass resonance frequency. When a current is stored on only one side, say on side one, the accelerometer sensitivity is proportional to the effective current:

$$I_1' = I_1 + \frac{L_{1b} - L_{1a}}{L_{1b} + L_{1a}} i_1 \qquad = \frac{L_{1b}\, I_{1a} - L_{1a}\, I_{1b}}{L_{1b} + L_{1a}} , \qquad (7)$$

as can be seen from Eqs. (34) and (46a) of Paper I. The accelerometer sensitivity is first measured with $I_{1a} = I_t$, $I_{1b} = 0$; and is then remeasured with $I_{1a} = 0$, $I_{1b} = I_t$. The ratio of these two sensitivities is L_{1b}/L_{1a} by Eq. (7). The asymmetry factors $(L_{1b} - L_{1a})/(L_{1b} + L_{1a})$ and $(L_{2b} - L_{2a})/(L_{2b} + L_{2a})$ are then found to be 0.15 and 0.34, respectively, and the ratio of $L_{2b}//L_{2a}$ to $L_{1b}//L_{1a}$ is 0.91. The geometric asymmetry factor can now be calculated as

$$\frac{L_{2b}//L_{2a}}{L_{1b}//L_{1a}} \frac{\omega_{2M}^2}{\omega_{1M}^2} = 0.83 .$$

The supercurrent ratio, $-I_2/I_1$, required to compensate for this asymmetry is found to be 0.84, so that the two measurements are in agreement within the errors.

B. Accelerometer Mode and Gradiometer Mode

In the gradiometer mode, the supercurrents are stored such that only differential accelerations at the two component accelerometers will produce signals. A common acceleration is "current-differenced" out before detection. If the relative polarity between the supercurrents at the two component accelerometers are reversed, the differential acceleration signals will then be current-differenced out. The gradiometer is, thus, activated in a "common accelerometer mode". Being an identical electromechanical system, the accelerometer mode has the same characteristics toward common accelerations as the gradiometer mode has toward differential accelerations.

In the experiment, the application of a pure acceleration is much easier than that of an acceleration gradient. Interchangeability of the roles between common and differential accelerations therefore provides us with an alternate method to evaluate and calibrate the gradiometer. This method is highly sensitive because a known acceleration can be applied with a much higher amplitude than a gravity gradient.

In each mode of circuit operation, the two coupled component accelerometers have two degrees of freedom and will have two normal modes of motion. The two proof masses move with the same phase in one mode at a frequency ω_+ and with opposite phases in the other mode at a frequency ω_-. These normal mode frequencies and Q's can be measured experimentally and provide information on the gradiometer parameters. We will first show how they are related to the gradiometer parameters.

The equations of motion and their constraints have been given in Eqs. (41) and (42) of Paper I. Strictly speaking, the normal mode frequencies ω_+ and ω_- are obtained as eigenfrequencies of these equations. This can be done by first eliminating the current coordinates $i_d(\omega)$ and $i_c(\omega)$. For free

oscillations, i.e., when $g_d(\omega) = g_c(\omega) = 0$, the dynamical equations become

$$(-\omega^2 + \omega_{1M}^2)\left[\frac{(L_0+L_{1p})m_1}{\Lambda^2 I_1'^2} + 1\right] x_1 + (-\omega^2 + \omega_{2M}^2)\frac{L_0\, m_2}{\Lambda^2 I_1' I_2'}\, x_2 = 0 \ , \quad (8a)$$

$$(-\omega^2 + \omega_{1M}^2)\frac{L_0\, m_1}{\Lambda^2 I_1' I_2'}\, x_1 + (-\omega^2 + \omega_{2M}^2)\left[\frac{(L_0+L_{2p})m_2}{\Lambda^2 I_2'^2} + 1\right] x_2 = 0 \ , \quad (8b)$$

where the frequency dependence of x_1 and x_2 have been omitted for simplicity. The resulting eigenfrequencies are given in Ref. 10. We shall obtain approximate solutions in simpler forms to illustrate the physics.

The two component accelerometers in our gradiometer are partially matched geometrically. We use the <u>symmetric component-accelerometer approximation</u>:

$$m_1 = m_2 \ , \quad (9a)$$

$$\omega_{1M} = \omega_{2M} \ , \quad (9b)$$

$$L_{1s} = L_{2s} \ , \quad (10a)$$

$$L_{1p} = L_{2p} \ . \quad (10b)$$

In this case, a wideband balance could be achieved without introducing i_1 and i_2. If we now take $I_1 = -I_2$ in the gradiometer mode, the eigenfrequencies are just given by

$$\omega_+ = \omega_{1c} = \omega_{2c} \ , \quad (11a)$$

$$\omega_- = \omega_{1d} = \omega_{2d} \ , \quad (11b)$$

to the leading term in the above approximation. In the accelerometer mode in which $I_1 = I_2$, the frequencies are reversed:

$$\omega_+ = \omega_{1d} = \omega_{2d} \ , \tag{12a}$$

$$\omega_- = \omega_{1c} = \omega_{2c} \ . \tag{12b}$$

The frequencies ω_{kc} and ω_{kd} are effective frequencies for the "complementary" current (i_c) and "additive" current (i_d) modes, as is evidenced from their definitions in Eq. (43) of Paper I, and are <u>theoretical</u> parameters for describing the operation of the gradiometer. The normal mode frequencies of motion, ω_+ and ω_-, on the other hand, are <u>physically measurable</u> quantities that provide us with approximate values of ω_{kc} and ω_{kd}.

When the gradiometer assembly is suspended by a weak spring system of a low resonance frequency Ω, the gradiometer platform has a finite mass M and will couple with the pair of masses. The three frequencies, Ω, ω_+, and ω_-, will all be shifted, and the equations of motion are modified. If we denote the platform position by X and measure the proof mass coordinates relative to it, the kinetic energy of the system is

$$\mathbf{T} = \frac{1}{2} \left[M\dot{X}^2 + m_1(\dot{X} + \dot{x}_1)^2 + m_2(\dot{X} + \dot{x}_2)^2\right] \ , \tag{13}$$

and the potential energy **V** has an additional term $\frac{1}{2} M\Omega^2 X^2$. The linearized equations of motion, Eq. (37) of Paper I, are then modified into

$$-\omega^2[(M + m_1 + m_2)X + m_1x_1 + m_2x_2] + M\Omega^2X = 0 \ , \tag{14a}$$

$$-\omega^2 m_1(X + x_1) + m_1\left(\omega_{1M}^2 + \frac{\Lambda^2 i_1^2}{m_1 L_{1s}}\right) x_1 + \Lambda I_1' \, i_1(\omega) = 0 \ , \qquad (14b)$$

$$-\omega^2 m_2(X + x_2) + m_2\left(\omega_{2M}^2 + \frac{\Lambda^2 i_2^2}{m_2 L_{2s}}\right) x_2 - \Lambda I_2' \, i_2(\omega) = 0 \ . \qquad (14c)$$

These equations are subject to the constraints given by Eq. (38) of Paper I.

We again make the approximation of Eqs. (9) and (10), along with $i_1 = i_2 = 0$. In the gradiometer mode ($I_1 = -I_2$), the eigenfrequency of the "out-of-phase mode" ($x_1 = -x_2$) of motion is unchanged:

$$\omega_{G-}^2 = \omega_{kd}^2 \ ; \qquad (15a)$$

whereas, the "in-phase mode" ($x_1 = x_2$) eigenfrequency is shifted to

$$\omega_{G+}^2 = \left(1 + \frac{2m_k}{M}\right) \omega_{kc}^2 \ . \qquad (15b)$$

Here we have made an approximation based on $\omega_{kM}^2 \gg \Omega^2$. In the accelerometer mode ($I_1 = I_2$), we find

$$\omega_{A-}^2 = \omega_{kc}^2 \ , \qquad (16a)$$

$$\omega_{A+}^2 = \left(1 + \frac{2m_k}{M}\right) \omega_{kd}^2 \ . \qquad (16b)$$

The parameters ω_{kc}^2 and ω_{kd}^2 are functions of I_k^2:

$$\omega_{kc}^2 = \omega_{kM}^2 + \frac{\Lambda^2 I_k^2}{m_k L_{kp}} \ , \qquad (17a)$$

$$\omega_{kd}^2 = \omega_{kM}^2 + \frac{\Lambda^2 I_k^2}{m_k (L_{kp} + 2L_0)} \ , \qquad (17b)$$

as obtained from Eqs. (44) of Paper I.

The shifted frequencies, f_{G-}, f_{G+}, f_{A-} and f_{A+}, measured as functions of I_k are presented in Fig. 5. The intercepts to $I_k^2 = 0$ are given by

$$f_{G-}^2(0) = f_{A-}^2(0) = f_{kM}^2 , \tag{18a}$$

$$f_{G+}^2(0) = f_{A+}^2(0) = (1 + \frac{2m_k}{M})\, f_{kM}^2 . \tag{18b}$$

Taking the ratio of the two intercepts enables a measurement of the mass ratio. We obtain $m_k/M = 0.052 \pm 0.006$, which is in agreement with the value given in Table 1.

The slopes of the graphs for ω_{A-}^2, ω_{A+}^2, ω_{G-}^2, ω_{G+}^2 versus I_k^2 are

$$\frac{\Lambda^2}{m_k L_p} , \ (1+ \frac{2m_k}{M})\frac{\Lambda^2}{m_k(L_{kp}+2L_0)} , \ \frac{\Lambda^2}{m_k(L_{kp}+2L_0)} , \ (1+ \frac{2m_K}{M})\frac{\Lambda^2}{m_k L_{kp}} , \tag{19}$$

respectively. From these, we obtain an inductance ratio:

$$\frac{2L_0}{L_{kp}} = 1.58 \pm 0.14 . \tag{20}$$

This result indicates that the output impedance has been chosen sufficiently large. Using the value of $\Lambda = 0.306$ H m^{-1} calculated from Eq. (15) of Paper I, we find $L_{kp} = 23$ μH, which is consistent with inductance values in Table 1. Also, we obtain $L_0 = 18$ μH. Consistency in the measurements indicate that the symmetric component accelerometer approximation is sufficiently good for diagnostic purposes.

The output inductance L_0 is the equivalent inductance at the transformer primary when the secondary is loaded by the SQUID input of approximately 2 μH.

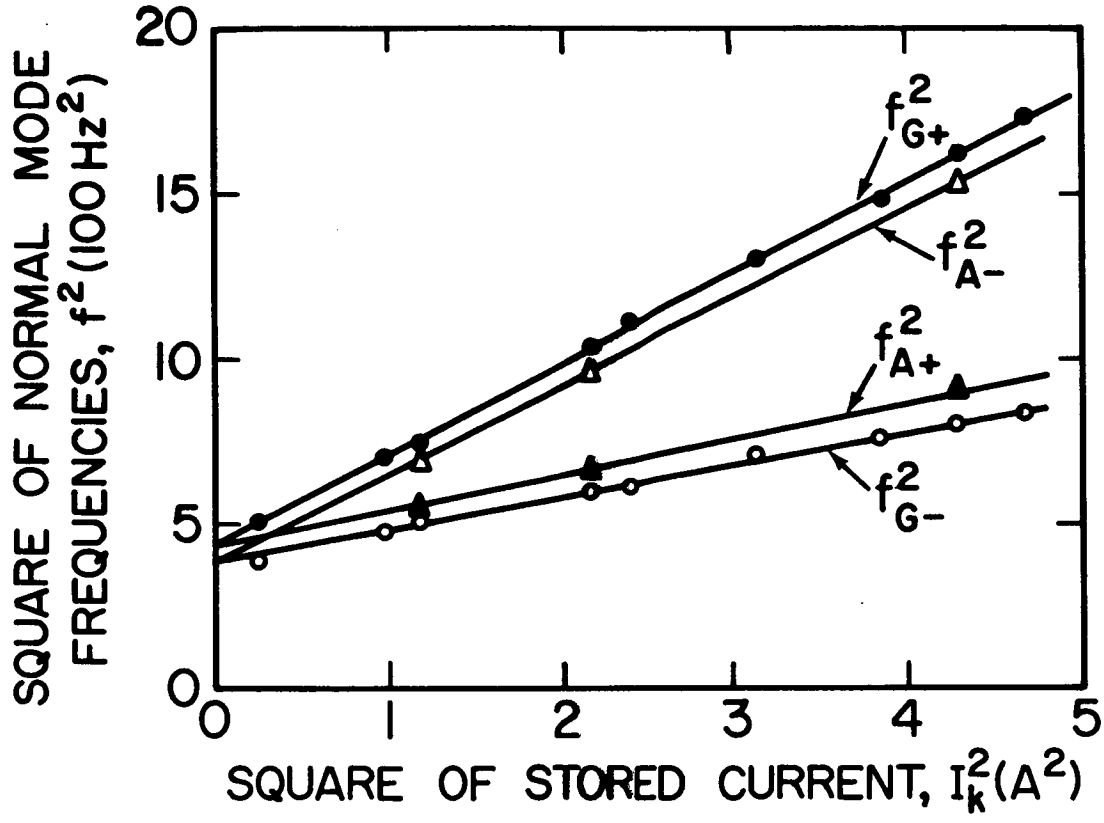

Fig. 5. Normal mode frequencies of the gradiometer as functions of the stored current.

The transformer has a turns ratio of 69:19 with calculated inductances of 42 μH and 3.2 μH, respectively, to a 20 % accuracy. L_0 can then be calculated from Eq. (75) of Paper I, and would have the above measured value of 18 μH if we take the transformer coupling factor to be $k_t^2 = 0.93$. However, the power transfer function of the transformer would then only be $H_p^{I,\ II} = 0.51 \pm 0.10$, as one can see from Eq. (76) of Paper I. The transformer has not been optimized in the past assembly, but this is not a problem until one reaches the amplifier-limited sensitivity. The resulting value of the effective electrical energy coupling to the SQUID is $\eta = 0.31$.

C. Circuit Optimization and Transfer Functions

Equation (53) of Paper I shows that the gradiometer transfer function, $H_{gi}^d(\omega)$, of an equivalent accelerometer is proportional to I'/ω_o^2 in the low signal-frequency limit. In the symmetric component-accelerometer mode, ω_o is identified with ω_{kd}.

In Fig. 6, we plot a measured curve of $|I_k|/f_o^2$ versus $|I_k|$ to indicate the functional dependence of the differential-acceleration-to-response-current transfer function on the stored current $|I_k|$. This plot shows that the gradiometer sensitivity first increases as $|I_k|$ is increased from 0, and then slows down due to an increase in f_o caused by an increasing $|I_k|$. The gradiometer is expected to reach its maximum sensitivity when $f_o^2 \simeq 2f_{kM}^2$ at $|I_k| \simeq 2$ A. However, this maximum is very smooth so that a smaller current can be used without a substantial reduction in sensitivity.

If the gradiometer sensitivity is SQUID noise limited, optimizing the above transfer function yields a maximum signal-to-noise ratio for the gradiometer. However, if the sensitivity is limited by the Brownian motion noise, one would have to maximize the function $Q_-^{1/2}\ |I_k|/f_o^2$ instead, where Q_- is the

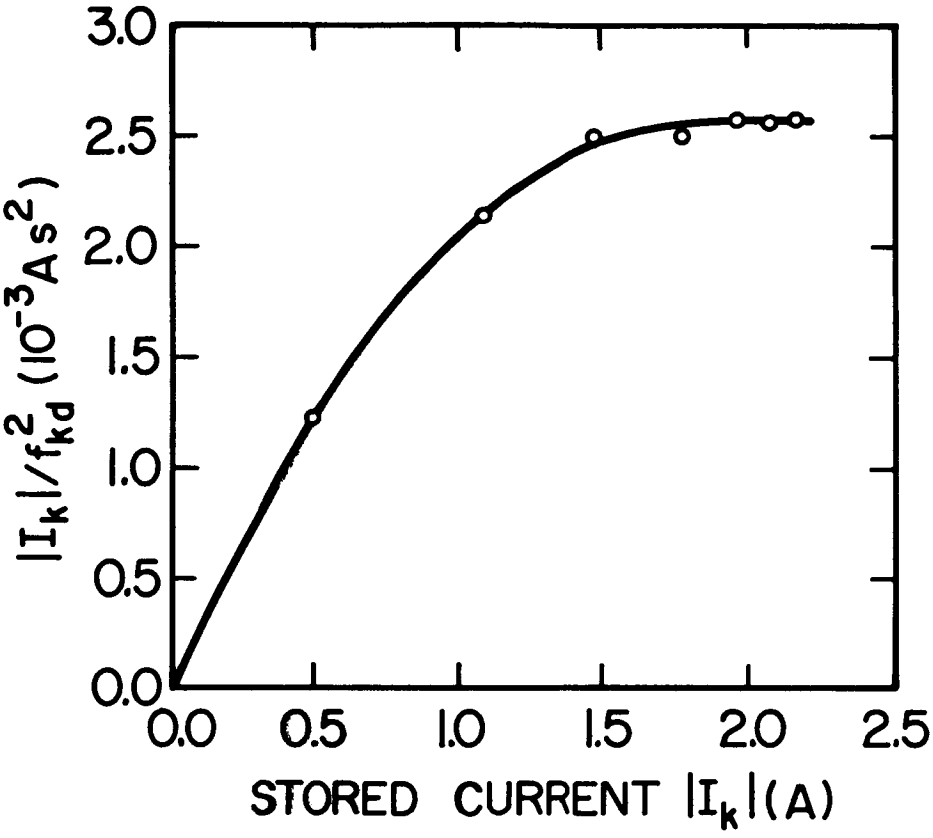

Fig. 6. Sensitivity scaling of the gradiometer as a function of the stored current.

quality factor of the out-of-phase mode: $f_{G_-} = f_o$.

In Section III of Paper I, we used the response current in L_0 to define transfer functions in harmony with the model of a reduced equivalent accelerometer. Here we prefer using the response current <u>at the SQUID input</u> L_1, a quantity which can be directly calibrated using the SQUID transfer function.

The in-phase mode of motion has the following parameters:

$$m_+ = 2m_k, \tag{21}$$

$$x_+ = \frac{x_2 + x_1}{2}. \tag{22}$$

In the calibration experiment, a common acceleration is provided by applying a sinusoidal displacement $X(\omega)$ to the gradiometer assembly. In this case, Eqs. (14) can be solved to obtain

$$(-\omega^2 + \omega_o^2)\, x_+(\omega) = \omega^2 X(\omega) \equiv g_c(\omega). \tag{23}$$

This acceleration produces a response current $i_+(\omega)$ which is proportional to $x_2 + x_1 = 2x_+$. The displacement-to-current transfer function is

$$H^A_{xi}(\omega) = \frac{i_+(\omega)}{x_+(\omega)} = \frac{2i_+}{(x_2 + x_1)_+}. \tag{24}$$

At a low frequency $\omega << \omega_o$, the <u>acceleration-to-current transfer function</u> is

$$H^A_{gi}(\omega) = \frac{i_+(\omega)}{g_c(\omega)} = \frac{2}{\omega_o^2} \frac{i_+}{(x_2 + x_1)_+}. \tag{25}$$

The parameters for the out-of-phase motion are

$$m_- = \frac{m_k}{2} , \tag{26}$$

$$x_- = x_2 - x_1 . \tag{27}$$

Notice that m_- is the effective mass m of the gradiometer defined in Section IIIE of Paper I. In the gradiometer mode, a differential acceleration $g_d(\omega)$ produces a differential proof mass displacement x_- with

$$(-\omega^2 + \omega_o^2)\ x_-(\omega) = g_d(\omega). \tag{28}$$

The response current $i_-(\omega)$ is proportional to just $x_2 - x_1 = x_-$. The displacement-to-current transfer function is therefore

$$H^G_{xi}(\omega) = \frac{i_-(\omega)}{x_-(\omega)} = \frac{i_-}{(x_2 - x_1)_-} . \tag{29}$$

The gravity-gradient-to-current transfer function for $\omega << \omega_o$ is

$$H^G_{\Gamma i}(\omega) = \frac{i_-(\omega)}{\Gamma(\omega)} = \frac{\ell}{\omega_o^2} \frac{i_-}{(x_2 - x_1)_-} , \tag{30}$$

where ℓ is the baseline and $\Gamma(\omega) \equiv g_d(\omega)/\ell$.

If the same magnitudes of stored currents are used in the two modes of circuit operation, the following equality is obeyed by the two equivalent circuits:

$$\frac{i_-}{(x_2 - x_1)_-} = \frac{i_+}{(x_2 + x_1)_+} . \tag{31}$$

The transfer functions in the two circuit modes are therefore related by

$$H^{G}_{Ti}(\omega) = \frac{\ell}{2} H^{A}_{gi}(\omega) \ . \qquad (32)$$

This simple relationship follows because Eqs. (25) and (30) contain the same resonance frequency ω_o, as is expected from Eqs. (11b) and (12a).

The function $H^{A}_{gi}(\omega)$ is measured by applying a sinusoidal acceleration $g_c(\omega) = \omega^2 X(\omega)$ to the gradiometer assembly at ω below 1 Hz. The response current is measured with the SQUID amplifier which has a current-to-voltage transfer function of 0.20 V μA^{-1}. The acceleration is applied to the gradiometer in the vibration isolation system described in Section IIIC. An electromagnetic shaker is coupled with a weak latex tubing from one side to the other of a vibration isolation stage (see Fig. 4) to provide a vertical acceleration to the gradiometer. The weak tubing acts as an attenuator, permitting a good signal-to-noise ratio without degrading the vibration isolation. The platform acceleration produced by the shaker has been calibrated by measuring its displacement and later confirmed with a commercial accelerometer.

Figure 7 shows the calibration of the accelerometer mode measured in terms of the current response i_+ at the SQUID input as a function of the applied acceleration g_c. Very small stored currents are used because of the extremely high sensitivity of the accelerometer. From the graph, we obtain a transfer function of (1.55 ± 0.05) mA per m s^{-2} for the accelerometer with only I_k = 1 mA stored on each side. The transfer function should be linear with the stored currents for low current values that produce negligible shifts of proof mass frequencies. This linearity is confirmed by Fig. 8, which is a plot of the measured acceleration-to-current transfer function as a function of I_k.

At high currents, the calibration curve in Fig. 7, which takes into

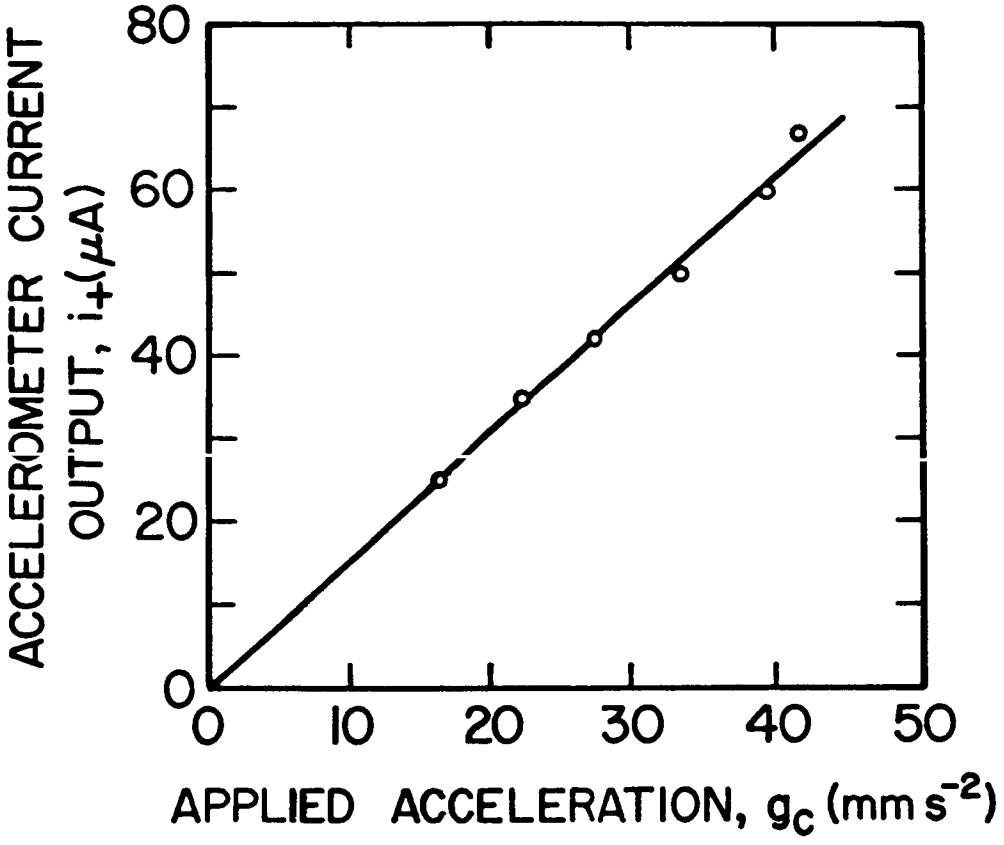

Fig. 7. Calibration in the accelerometer mode with 1 mA stored currents.

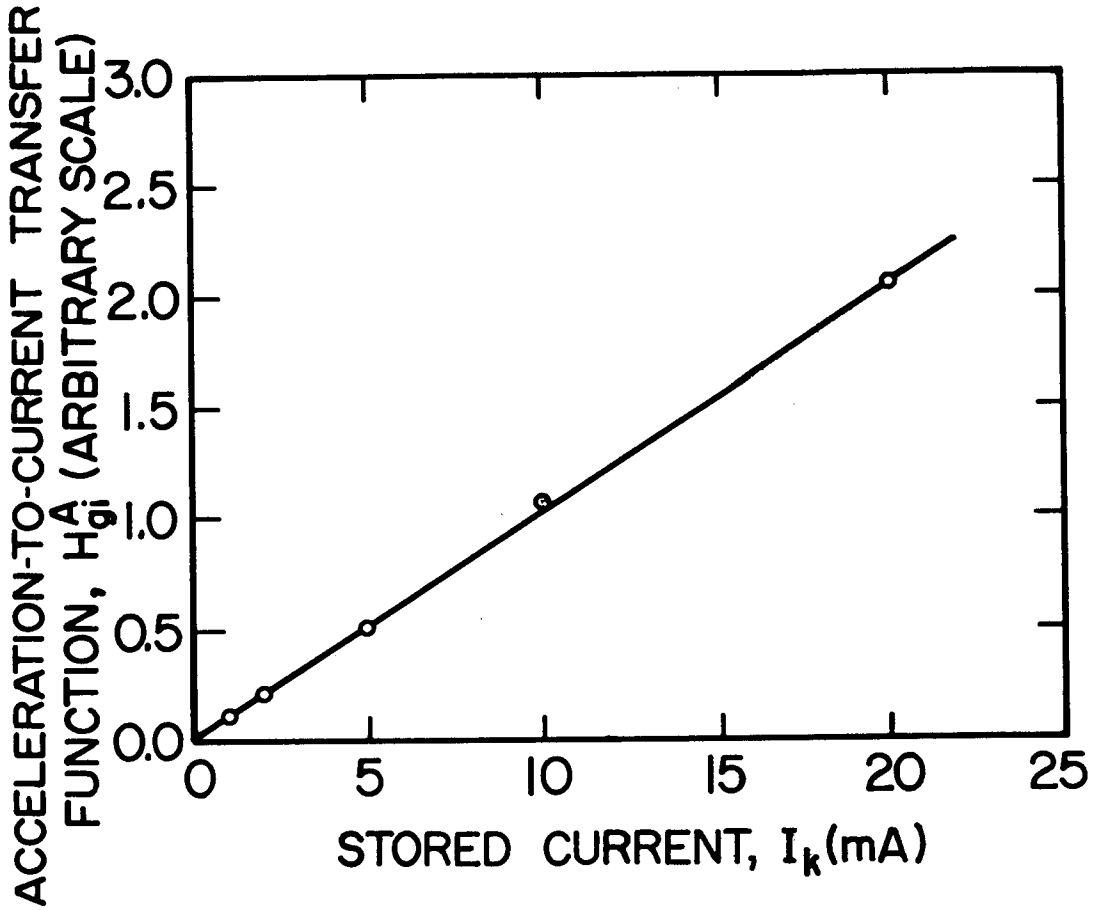

Fig. 8. Sensitivity scaling in the accelerometer mode as a function of the stored current.

account frequency shifts, is used to extrapolate our transfer function measurements. We then obtain

$$H^{A}_{gi}(\omega) = \frac{i_{+}(\omega)}{g_{c}(\omega)} = (1.6 \pm 0.1)\ \text{A}\ (\text{m s}^{-2})^{-1} \qquad (25')$$

for a near optimum current value of I_k = 1.5 A. Converting this value to the transfer function in the gradiometer mode, we have

$$H^{G}_{\Gamma i}(\omega) = \frac{i_{-}(\omega)}{\Gamma(\omega)} = \frac{0.16\ \text{m}}{2}\ \frac{1.6\ \text{A}}{1\ \text{m s}^{-2}} = (0.13 \pm 0.01)\ \text{nA E}^{-1}. \qquad (32')$$

The SQUID amplifier noise, when loaded with the fully charged gradiometer, was measured to be $S_I^{1/2}(f)$ = 8.9 pA $\text{Hz}^{-1/2}$, which corresponds to $E_A(f)$ = $7.9\text{x}10^{-29}$ J $\text{Hz}^{-1/2}$ for L_I = 2 μH, at a high frequency (> 60 Hz) where the proof mass displacement noise becomes negligible. This noise level would correspond to an amplifier-limited gravity gradient noise of 0.069 E $\text{Hz}^{-1/2}$. This value is in close agreement with the theoretical sensitivity of 0.068 E $\text{Hz}^{-1/2}$ which is obtained by directly substituting the measured SQUID noise and the measured values of η = 0.31 and β = 0.53 into Eq. (79) of Paper I. In our tests, the gradiometer noise at low frequencies was limited by seismic noise at 0.3 ~ 0.7 E $\text{Hz}^{-1/2}$ level. Therefore, we would not lose sensitivity by using a somewhat smaller gain. Stored currents of 0.55 A were used in the tests reported in Section VI. The transfer function deduced from the accelerometer mode calibration gives 62 pA E^{-1} at this current level. In Section VIA, we will check this value with the direct calibration of the gradiometer which employs gravity gradient signals.

V. INVESTIGATION OF INSTRUMENT NOISE AND ERRORS

A. Environmental Noise and Common Mode Balance

Vibrations were found to be the most serious environmental noise. Our early tests with the gradiometer rigidly mounted inside a liquid N_2 shielded He dewar have encountered a vibration noise energy of 10^{-8} J at the proof mass resonance frequency of 19 Hz. Such a noise level corresponds to an equivalent Brownian motion at a noise temperature of 7×10^{14} K, which is 10^7 times the 4 K Brownian motion in vibration amplitude!

When the gradiometer is balanced against common accelerations, its response to the vibration noise is greatly reduced. In the experiment, however, the gradiometer can be balanced only if we can use its acceleration response as a guide. Sufficient vibration isolation to achieve a noise level of the unbalanced gradiometer well within the amplifier dynamic range is therefore essential. A minimum of 60 dB isolation is required at the proof mass resonance frequencies in order to be able to operate at the full sensitivity of the accelerometers.

If vibrations have a white acceleration spectrum, the low frequency noise will be Q times less than that at the proof mass resonances; thus, this noise will not overload the amplifier. Therefore, we chose to start with vibration isolation at higher frequencies where the SQUID amplifier was being overloaded. This isolation would enable us to balance the accelerations and obtain a working gradiometer.

If the proof mass acceleration noise amplitude can be reduced by four orders of magnitude, one will be able to observe the actual Brownian motion at the resonances in a gradiometer with a 60 dB balance. Although such an observation may not improve the acceleration noise at the low frequency end, it

could prove to be very informative. This observation would determine the Brownian motion level of the instrument, and show whether the observed acceleration noise comes from the environment or from the intrinsic noise of the instrument.

Although an electronic "cold damping" technique [8,10] could have been applied to selectively filter the vibration noise at the proof mass resonances, there were other modes in the environment which require wideband isolation. Therefore, we chose to develop a passive vibration isolation system with which the gradiometer can be tested in its simplest form. Satisfactory vibration isolation of the gradiometer was an essential step in leading to a successful demonstration of its performance and the operation of the device as a detector in the inverse square law experiment [7,5]. Various combinations of low-pass vibration filters were tried to isolate the noise coming from the ground and the dewar. Filters were improved in steps with the guidance of vibration data obtained in each step.

With the three-stage vibration isolation system described in Section IIIC, the noise at the proof mass resonance decreased to 2×10^4 K, corresponding to a displacement of 5×10^{-12} m. The achieved improvement at 20 Hz was therefore better than 100 dB. At frequencies above 60 Hz, the spectrum indicated the SQUID-limited noise level.

We now turn to the wideband common mode balance method described in Section IIID of Paper I. In this method, calibrated sinusoidal acceleration signals are provided in the vertical direction by means of an electromagnetic shaker. Two out of the three stored currents I_1, I_2 and i_2 are iteratively adjusted for balance at 0.9 Hz ($\ll \omega_o/2\pi$) and 70 Hz ($\gg \omega_0/2\pi$) in turn. This is a painstaking procedure since a balance point is searched for in a two-dimensional parameter space and sufficient time should be allowed after each

adjustment of currents for the mechanical disturbance of the system to damp down.

Figure 9a shows the 0 - 50 Hz noise spectrum of the gradiometer balanced in the wide band to 1 part in 10^3. The transfer functions are obtained from the accelerometer mode calibrations using the relationships discussed in Section IV. This procedure gives $[H^G_{gi}(\omega)]^{-1} = \omega_o^2 x_-/i_- = 1.29$ m s^{-2} A^{-1}. The gradiometer is less sensitive to external common accelerations now. Shown in the spectrum is the differential mode of the masses at $f_o = \omega_o/2\pi = 24.8$ Hz of an rms amplitude $\omega_o^2 x_- = 2.75$ nm s^{-2}. The noise temperature for this mode is given by

$$\frac{1}{k_B}\left(\frac{m_k}{2}\right)\omega_o^2\, x_-^2 = 4.5 \text{ K} . \qquad (33)$$

Thus, this spectrum represents the observation of the Brownian motion of the proof masses in the differential mode at the liquid He temperature. All other peaks are attenuated by about 10^3, which is the degree of balance obtained. This data confirms that the observed noise is almost entirely environmental and is not intrinsic to the gradiometer.

Figure 9b shows the 0 - 10 Hz spectrum. The vertical scale of the plot has been calibrated by using the accelerometer mode, and confirmed by a direct calibration with a known gravity gradient signal which will be explained in Section VI. The noise in the 5 - 10 Hz band reaches below 1 E Hz$^{-1/2}$ but the background seems to be close to 0.3 E Hz$^{-1/2}$. Excessive vibration noise has degraded the spectrum at several peaks. The noise in the 1 - 4 Hz range is heavily contaminated by the rocking mode of the gradiometer (f_r) at 2.5 Hz and other modes associated with the vibration isolation system. The 0 - 1 Hz spectrum shown in Fig. 9c exhibits the swinging modes (f_{s1}, f_{s2}) around 0.3

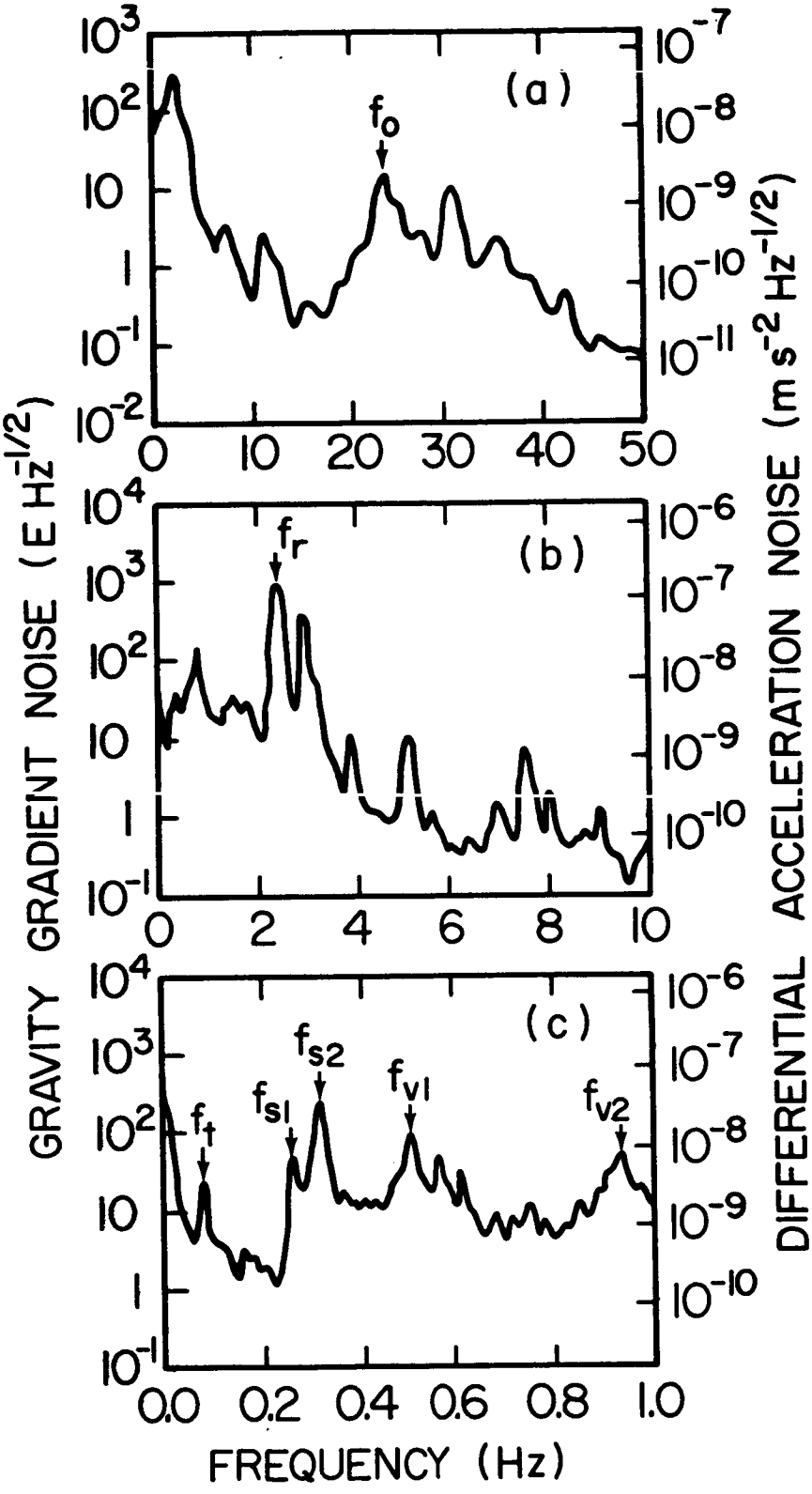

Fig. 9. Noise spectrum of the gradiometer on a three-stage vibration isolation system.

Hz, the vertical dewar suspension mode (f_{v1}) at 0.5 Hz, the vertical gradiometer rubber suspension mode (f_{v2}) at 0.9 Hz, and a torsional mode (f_t) at 0.08 Hz.

Our low-pass filters introduced numerous peaks at their own resonances. These filters were needed initially to prevent the SQUID from overloading at the higher frequency peaks. After the common mode balance, the gradiometer became intrinsically insensitive to the environmental noise. Therefore, in the gradiometer mode, the filters could be reduced to a minimum. We found a single-stage filter provided by the rubber tubing inside the vacuum was sufficient for a balanced gradiometer and eliminated many undesirable peaks from the signal bandwidth.

B. Gradiometer Noise

Figure 10 shows the noise spectra of the gradiometer obtained with the single-stage filter. The upper trace is the noise spectrum measured with the gradiometer in the accelerometer mode. The lower trace is the gradiometer output after the common mode balance to 3 parts in 10^5 has been achieved toward an applied acceleration at 0.18 Hz. The SQUID noise limit of 0.069 E $Hz^{-1/2}$ with the associated 1/f noise is plotted by a dotted line. The vertical scale shows both the acceleration and gradient noise calibrations, which are related by Eq. (32). The ratio of the two spectra at any frequency, therefore, represents the actual reduction of noise outputs at that particular frequency as a result of the balance.

First, comments are due for the measured acceleration noise spectrum (top trace). The general structure of this spectrum, which contains a broad peak around 0.25 Hz and a dip around 0.1 Hz, and the noise level of approximately 2.5×10^{-7} m s^{-2} $Hz^{-1/2}$ at 0.5 Hz are obtained consistently from run to run

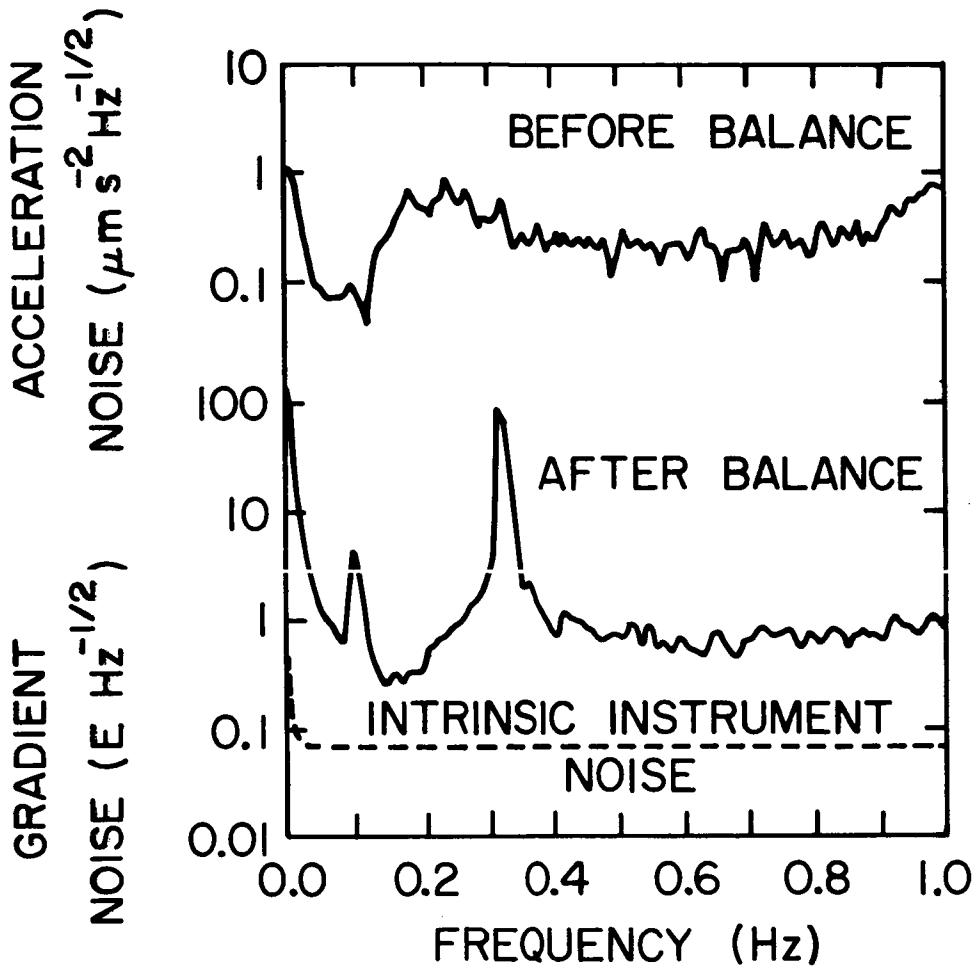

Fig. 10. Low frequency noise spectra of the gradiometer on a single-stage vibration filter.

after waiting sufficiently long for resonances in the gradiometer platform to damp down. This noise data has been reproduced by using conventional accelerometers mounted at the room temperature end of the pendulum suspension and on the laboratory floor, with the exception of the dip at 0.1 Hz for which the room temperature accelerometers did not have enough resolution. Since the data represents the residual acceleration noise of a deep underground laboratory, the upper curve in Fig. 10 must reflect geophysically significant seismic activity, except for the broad peak near 1 Hz which is due to the low-Q vertical mode of the rubber suspension. It is noteworthy that, while acceleration noise spectra measured at the top end of the pendulum in the vertical and horizontal directions looked similar, the noise output of the superconducting accelerometer correlated closely (> 90%) with the vertical acceleration. This correlation indicates that the horizontal acceleration is indeed attenuated by the pendulum action, as has been predicted by the analysis shown in Appendix A. Since the gradiometer is pointing at an umbrella angle $\theta_u = \tan^{-1} \sqrt{2} = 54.7°$, the noise spectrum of Fig. 10 should then be raised by a factor of $\sec \theta_u = \sqrt{3}$ to obtain the proper calibration of the vertical acceleration noise at College Park, Maryland.

The lower trace of Fig. 10 represents a typical residual noise spectrum of a balanced gradiometer, with the exception of the 0.1 Hz peak of the torsional mode which disappears into the background noise in the quietest situations. Unlike the torsional mode, however, the swinging mode at 0.32 Hz is always present with its peak at around 100 E $Hz^{-1/2}$ level. Also persistently present is the low frequency excess noise below 0.1 Hz. The noise level is approximately 0.7 E $Hz^{-1/2}$ between 0.5 and 0.9 Hz and reaches a minimum value of 0.3 E $Hz^{-1/2}$ in a narrow window around 0.15 Hz. Comparison of the two traces reveals that the noise was reduced only by a factor of 3 x

10^3, which represents a discrepancy of a factor of 10 from the value expected from the common mode balance. Another noticeable feature is that, although the general structure of the background spectrum of the balanced gradiometer, with the resonance peaks removed, appears similar to the shape of the acceleration noise, the two spectra are not well correlated. Therefore, the residual noise of the gradiometer must be coming from a source other than vertical acceleration.

It is desirable to determine the Browian motion noise level of the instrument. The power spectral density of the thermal noise of the gradiometer is given in Eq. (87) of Paper I:

$$S_{\Gamma,B}(f) = \frac{8}{m_1 \ell^2} \frac{k_B T}{\tau(f)} . \qquad (34)$$

It is difficult to measure the effective damping time $\tau(f)$ at $f \ll f_o$ directly. If one assumes the "white acceleration noise model", $\tau(f)$ in Eq. (34) can be replaced by the measured quantity, $\tau(f_o)$. The measured Q values are of the order of 5×10^4 and are probably pressure limited. This implies $\tau(f) = 3.2 \times 10^2$ s^{-1} and $S^{1/2}_{\Gamma,B}(f) = 0.01$ E Hz$^{-1/2}$ for our gradiometer. If, on the other hand, the effective Q is assumed to be independent of frequency, the Brownian motion noise would become frequency dependent:

$$S^{1/2}_{\Gamma,B}(f) = 0.01 \text{ E Hz}^{-1/2} \left(\frac{f}{f_o}\right)^{1/2} . \qquad (35)$$

In either case, the thermal noise would be negligible compared to the SQUID noise level of 0.069 E Hz$^{-1/2}$.

We therefore conclude that the observed noise spectrum is <u>extrinsic</u> to the instrument and is due to error mechanisms which couple environmental noise

into the gradiometer output. Error sources responsible for the observed residual noise of the gradiometer are identified in the following section with the aid of Appendices.

C. Instrument Errors

The dynamics of a platform suspended as a pendulum is analyzed in Appendix A. The pendulum decouples the gradiometer from angular motions of the external world. The horizontal acceleration transmitted to the gradiometer is almost exactly cancelled by the modulated Earth's gravity which is caused by the induced tilt of the instrument. It is found, however, that the resulting angular velocity and angular acceleration can couple to the gradiometer through centrifugal acceleration and through the misalignment of the effective gradiometer sensitive axis with respect to the baseline. Since the vertical component of linear acceleration is balanced out to a sufficient degree, the horizontal acceleration can produce a limiting instrument error by driving a secondary angular motion.

Experimentally, the noise of the unbalanced gradiometer correlates with the external acceleration in the vertical direction. This correlation and the absence of a pronounced resonance peak at the pendulum frequency $f_p = 0.32$ Hz in the upper trace of Fig. 10 prove that the horizontal vibration isolation by the pendulum action really works for an accelerometer. A close examination of the noise spectrum reveals a barely visible resonance peak at f_p above the background noise. This result renders a remarkable proof for the theory developed in Appendix A. According to Eqs. (A13), the horizontal acceleration sensed by an accelerometer under the pendulum suspension should be peaked at its resonance with a net gain of unity. Since the measured frequency spectra of the horizontal and vertical accelerations agree within 10 dB, the supercon-

ducting accelerometer pointing at an umbrella angle should measure a horizontal acceleration with a maximum amplitude of approximately 3 times that of the vertical acceleration at f_p. Therefore, the horizontal acceleration peak sticks out barely above the vertical acceleration background.

The analysis in Appendix A also leads to a prediction that, for a gradiometer, the overall effect of the pendulum action is that of a wideband attenuator for a horizontal acceleration, with its attenuation improving as the frequency approaches dc. In particular, when $\omega > \Omega_E/|\delta\hat{n}_{+\ell}|$, the dominant coupling mechanism for the horizontal acceleration is the induced angular acceleration, as given by Eq. (24). Below this frequency, the centrifugal acceleration error dominates. The cross-over frequency is 10^{-2} Hz when $|\delta\hat{n}_{+\ell}| = 10^{-3}$. The frequency response of the angular acceleration, $|h_{\vec{\alpha}}(\omega)|$, has been plotted in Fig. A2. One can see a strong resemblance between this curve and the gradiometer output, the bottom trace of in Fig. 10, above 0.2 Hz. In fact, the agreement improves when the spectrum of the driving background acceleration is taken into account. In Fig. 11, we plot typical observed spectra for the vertical (top dotted line) and horizontal (top dashed line) accelerations $\vec{A}_z(\omega)$ and $\vec{A}_h(\omega)$ as well as the gradiometer noise output (solid line). The residual vertical acceleration expected from the vertical common mode balance of 90 dB is plotted by the bottom dotted line. The bottom dashed line is a fit obtained by multiplying the spectrum for $\vec{A}_h(\omega)$ with its transfer function through the angular acceleration. The misalignment error required for this fit is $|\delta\hat{n}_{+\ell}| \cong 7 \times 10^{-4}$, which is in close agreement with the value determined from the observed centrifugal acceleration: $|\delta\hat{n}_{+\ell}| = 6 \times 10^{-4}$ (see Appendix B). Notice that the gradiometer noise above 0.2 Hz is completely accounted for by this single error mechanism: the horizontal acceleration coupled through the induced angular acceleration.

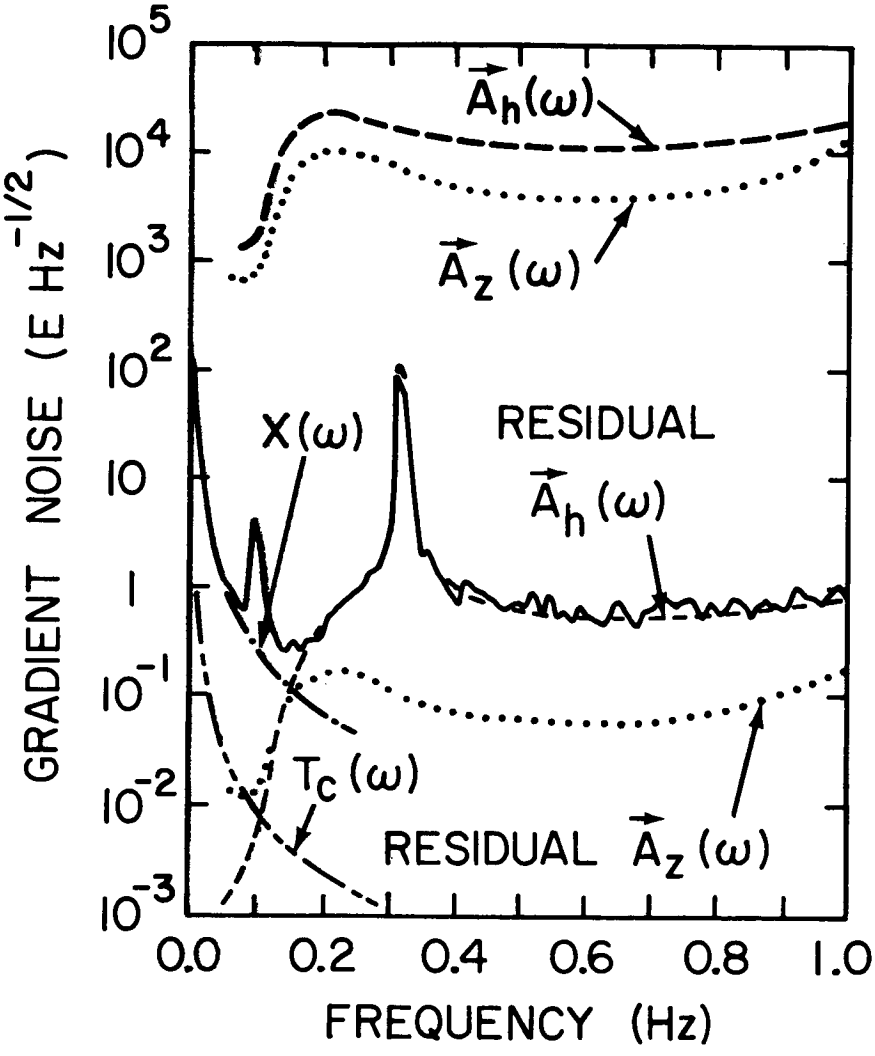

Fig. 11. Various error contributions to the gradiometer noise spectrum.

The value of $\delta\hat{n}_{\wedge}$ (the misalignment of the average sensitive axis of the gradiometer with respect to the baseline vector $\vec{\ell}$) found above is rather large in view of the fact that the parallelism of the mating surfaces of the mechanical components of the gradiometer was specified to 5×10^{-5}. This mechanical precision implies that the experimental value of $\delta\hat{n}_{-}$ (the relative misalignment between the sensitive axes of the component accelerometers) is of the order of 10^{-4}. A similar value could have been obtained also for $\delta\hat{n}_{\wedge}$ if the center lines of the two accelerometers had been located within 10^{-2} mm from each other, which is certainly feasible. However, without realizing the seriousness of the induced angular acceleration problem, we had left the centering of the accelerometers to crude positioning by the mounting screws. This must have produced a mismatch of the center lines by approximately 0.1 mm, causing the observed misalignment $|\delta\hat{n}_{\wedge}| = 6 \times 10^{-4}$.

We now turn our attention to the excess noise below 0.1 Hz, seen in Fig. 10. During the experiment, the SQUID electronics was shielded against rf interference to avoid electronics drift. Although instrument drift can be caused by relaxation of trapped magnetic flux [13], the observed low frequency noise did not decrease significantly when the ambient magnetic field was reduced by a factor of 10^3 by adding mu-metal shields. With these electrical sources of low frequency noise eliminated, we suspect the temperature drift and various nonlinear effects as the most likely sources for the observed excess noise. As has been discussed in the Appendix of Paper I, the superconducting gradiometer can be rather sensitive to temperature noise and nonlinearities in the system can down-convert the wideband vibration noise to a gradient noise near dc. These low frequency error mechanisms are analyzed in detail in Appendix B of this paper. Owing to the limited resolution of the Ge thermometer used to monitor the temperature of the gradiometer assembly,

the low frequency noise spectrum due to temperature fluctuation is computed from an independent measurement of the temperature noise of a liquid He bath of a different experimental setup [8] with the aid of a model for heat conductivity between the He and the gradiometer. The resulting spectrum is found to be

$$[S_{\Gamma,T}(f)]^{1/2} \cong 1.0 \times 10^{-2} \text{ E Hz}^{-1/2} \left(\frac{0.1 \text{ Hz}}{f}\right)^2 . \qquad (36)$$

The scale-factor nonlinearity is computed from the second order circuit equations for component accelerometers, generalized from Eqs. (29) and (33) of Paper I. The low frequency noise expected from this is of comparable magnitude as the temperature effect at 0.1 Hz, but has a slightly different frequency dependence:

$$[S_{\Gamma,cc}(f)]^{1/2} \lesssim 1 \times 10^{-2} \text{ E Hz}^{-1/2} \left(\frac{0.1 \text{ Hz}}{f}\right)^{3/2} . \qquad (37)$$

The effect of the centrifugal acceleration is found to be about two orders of magnitude smaller than this value.

The temperature noise of Eq. (36) is plotted in Fig. 11 by a dash-dot-dot line. The actual low frequency noise, denoted by $X(\omega)$, is about 30 times larger than this calculation. Since the temperature drift of the He bath depends on the exact geometry and thermodynamics of the particular cryostat involved, and on account of additional uncertainties in the thermal model of the instrument, the discrepancy by a factor of 30 does not exclude a possibility that the observed low frequency noise is due to temperature fluctuations. However, because a comparable level of noise is also predicted from the nonlinearity of the instrument, we cannot be conclusive, without further experi-

mental investigations, as to the origin of the observed excess noise below 0.1 Hz. In future experiments, the temperature of the He bath will be regulated, and the gradiometer will be linearized by means of a force rebalance feedback with a hope to eliminate the low frequency excess noise.

Another interesting error mechanism discussed in Appendix B is the second-harmonic generation by the centrifugal acceleration. This effect has been observed for large resonance peaks when the system is disturbed mechanically (Fig. B2). During the quiet operation of the instrument, however, no second harmonics were observed above the background noise spectrum of the gradiometer.

VI. GRAVITY GRADIENT MEASUREMENT AND SENSITIVITY CALIBRATION

We shall now describe the gravity gradient calibration with the observation of signals in two types of experiments. A precise calibration of the instrument can be obtained by using a periodic gravity gradient generator and averaging the signal over a number of periods. For such an ac experiment, however, any electrical pickup or mechanical cross coupling at the signal frequency must be eliminated. A "dc" experiment, in which a compact object is brought near the gradiometer and removed, fares better in this regard. Although the use of signal averaging to improve signal the signal-to-noise ratio is less applicable here, any cross coupling problem will appear as a transient which can be distinguished from the dc shift in the gradiometer output caused by the gravity signal. We have performed both experiments successfully, as well as an inverse square law test in which the gradiometer outputs in three orthogonal orientations of the sensitive axis are summed.

A. AC Gravity Gradient Experiment

The ac calibration of the gradiometer was obtained with a large ($M = 1.6 \times 10^3$ kg) Pb pendulum. The Pb sphere was located approximately in the same horizontal plane with the gradiometer at an average distance r of 2.3 m away. The gradiometer sensitive axis was at an angle of $\cot^{-1} \sqrt{2}$ with respect to the horizontal plane and was in the plane of swing of the pendulum. The gradiometer thus measured a gravity gradient component given by

$$\Gamma_{11} = - \frac{GM}{r^3} \frac{1}{2} [1 + 3 \cos (2 \cot^{-1} \sqrt{2})] = - \frac{GM}{r^3} . \qquad (38)$$

When the pendulum swung by $\Delta r(\omega)$, it generated a change in the gravity gradient by

$$\Delta\Gamma_{11}(\omega) = \frac{3GM}{r^4}\,\Delta r(\omega). \qquad (39)$$

The SQUID amplifier output was measured with a spectrum analyzer.

In order to assure that the observed signal was truly gravitational, various precautions were taken. When all three vibration isolation stages were used, excess signals at various harmonics of the pendulum frequency were seen. Correlation studies indicated that a strong second harmonic was generated by an air current driven by the swinging pendulum. This effect was eliminated by shielding the entire apparatus with a wooden enclosure and by using only one rubber filter which was inside the vacuum (see Fig. 4). The possibility of direct mechanical coupling between the pendulum and the gradiometer has also been investigated. With the gradiometer charged in the accelerometer mode and the pendulum swinging at its full amplitude ±30°, we did not see any acceleration signal at the pendulum frequency above the ground noise. The problem of such mechanical coupling has been alleviated by several factors. The pendulum was suspended from the 2 m thick concrete ceiling; whereas the dewar sat on a firm floor, 12 m below the ground level, in the basement of the building. Furthermore, the gradiometer was balanced against common accelerations, and the pendulum suspension used for the gradiometer gave isolation of tilt at all frequencies. In order to avoid electrical pickup at the signal frequency, a pneumatic driving mechanism was developed for the Pb pendulum and a natural resonant oscillation was used for most tests.

The rms voltage measured at the pendulum frequency of 0.228 Hz is plotted in Fig. 12 against the calculated rms gravity gradient generated by the pendulum. This plot gives a calibration of 58 pA E^{-1} and agrees with the accelerometer mode calibration, reported in Section IVC, to within 7 %. This

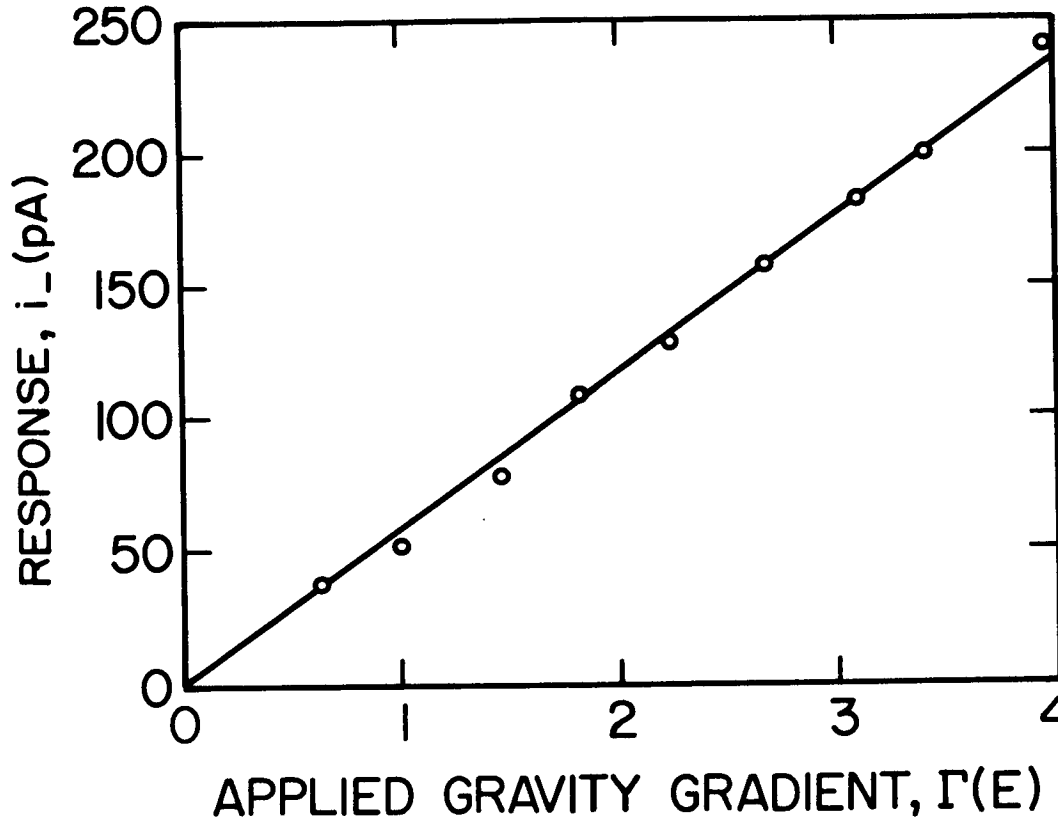

Fig. 12. AC calibration of the gradiometer.

agreement is within our errors. The distance and orientation measurements in either calibration were not intended for high precision.

B. DC Gravity Gradient Experiment

The noise spectrum of Fig. 10 indicates that the noise is lower below the 0.3 Hz swinging mode of the platform. In order to perform a dc experiment, we put in active low-pass filters which filtered off the peaks above 0.16 Hz from the amplifier output. The response function of the filters to a step dc voltage change is shown in Fig. 13a. The characteristic rise time and ripples of the filters will be seen when a step function, gravity gradient signal is applied.

We then moved a Pb brick in and out manually near the dewar at 10 ~ 15 s intervals. The brick weighed 12 kg and was brought to 0.17 m from the gradiometer. The gravity gradient generated was about $GM/r^3 \simeq 40$ E, with a geometrical factor of the order of unity which depends on the exact source-detector orientation.

In Fig. 13b, the Pb brick was moved in, out and then in again, roughly in the horizontal plane of the gradiometer. The times and directions of the movement of the Pb brick are indicated by arrows. The line of sight of the source was approximately at an angle of $\cot^{-1}\sqrt{2}$ from the gradiometer axis. The expected signal is then

$$\frac{GM}{r^3}\left(1 - \frac{13}{72}\frac{\ell^2}{r^2}\right) \simeq 37 \text{ E}. \qquad (40)$$

The ℓ^2/r^2 term is the finite baseline term of the gradiometer. Here the Pb brick has been approximated as a point mass. Its actual geometry and size should be taken into account for a precise calibration. The measured peak-to-

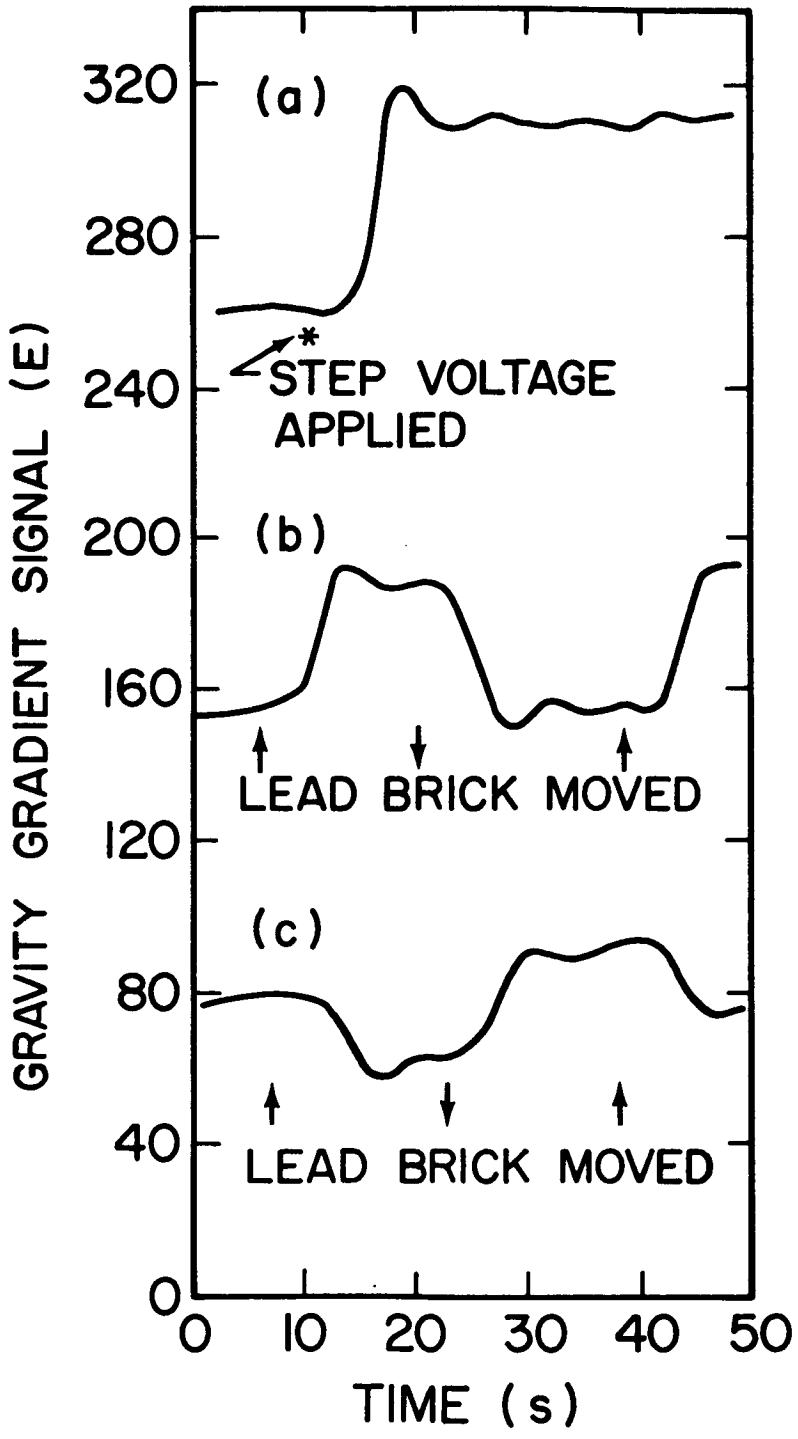

Fig. 13. DC gravity measurements (dc level is arbitrary).

peak dc current change is 2.3 nA. This current corresponds to (38 ± 2) E, in good agreement with Eq. (40), if the accelerometer mode calibration of Section IVC is used.

For Fig. 13c, the brick was moved in the same way but along a direction roughly perpendicular to the gradiometer axis. The expected signal, if the Pb brick were a point mass and were located accurately, is given by

$$-\frac{GM}{r^3}\left(1-\frac{3}{8}\frac{\ell^2}{r^2}\right) \simeq -34 \text{ E}. \qquad (41)$$

The value measured from Fig. 13c is (-25 ± 2) E. An error of 10 % in r and in angular orientation could produce this gradient error of 30 %. The brick has a long rectangular shape so that a substantial amount of its mass was at other orientations and at larger separations relative to the gradiometer.

The experiments have been qualitatively repeated at a few other orientations relative to the gradiometer axis. The results agree with what we expect from the tensor property of the single-axis gradiometer. The validity of a gravity signal has therefore been substantiated.

C. Inverse Square Law Experiment

The most impressive demonstration that the gravity gradiometer output is a genuine gravity gradient signal comes from the inverse square law data [5, 7] in which the angular pattern of the gravity gradient tensor is checked. For this experiment, the sensitive axis of the single-axis gradiometer was turned into three orthogonal directions by rotating the entire experimental cryostat on a turn table incrementally by 120° around the vertical axis while the gradiometer was suspended in the umbrella angle. The resulting three outputs and their sum are plotted in Fig. 14 after signal-averaging over 500

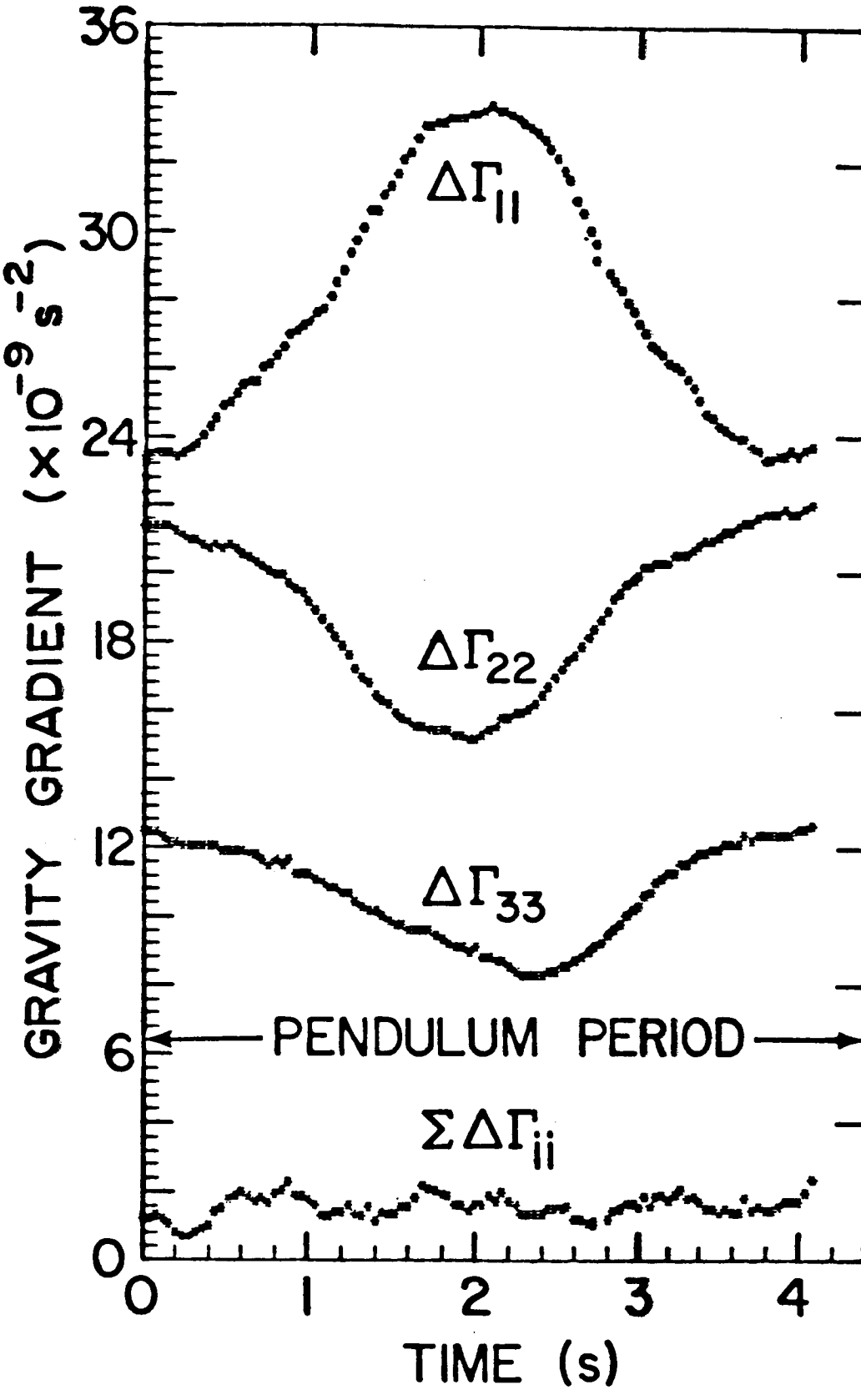

Fig. 14. Inverse square law data (dc level is arbitrary).

pendulum periods. The peak-to-peak amplitudes of the three outputs agree with the theoretical formula:

$$\Delta\Gamma_{ii} = \frac{GM}{r^3}\frac{3\Delta r}{r}\cos 2\phi_i, \tag{42}$$

where $r = 2.3$ m is the average distance between the Pb sphere and the gradiometer, $\Delta r = 0.84$ m is the peak-to-peak amplitude of swing, and $\phi_i = 120°(i - 1) - 3.7°$ is the angle that the projection of the i-th sensitive axis onto the horizontal plane makes with the line of sight between the detector and the source.

The sum of the righthand side of Eq. (42) over i = 1 to 3 vanishes as expected from the Poisson equation for Newtonian gravity, Eq. (12) of Paper I:

$$\sum_i \Delta\Gamma_{ii} = 0. \tag{43}$$

The sum of the three orthogonal measurements, the bottom trace of Fig. 14, verifies this condition within experimental uncertainty:

$$\sum_i \Delta\Gamma_{ii} = (+0.15 \pm 0.23) \times 10^{-9}\ s^{-2}. \tag{44}$$

The signal and noise in this result have been analyzed carefully and published as a null test of the gravitational inverse square law [5]. Within the inverse square law, the mutual cancellation of the signals in three arbitrary orthogonal directions is strong proof that the instrument is really measuring genuine gravity gradient signals since it will be highly unlikely that other error signals also satisfy the condition (43).

VII. SUMMARY AND CONCLUSION

A superconducting gravity gradiometer has been constructed and evaluated very carefully. Both the signal transfer and noise characteristics of the device agree closely with the theoretical model. Practical error sources have been identified experimentally as well as analytically. Although the instrument has only been tested on a passive platform without any feedback or error compensation, it has shown a performance level of $0.3 \sim 0.7$ E $Hz^{-1/2}$, which surpasses the value achieved in a sophisticated room temperature gravity gradiometer [14] by three orders of magnitude in power. Further reduction of noise should be possible by improving the alignment of component accelerometers or by actively stabilizing the gradiometer platform against horizontal accelerations. The temperature of the He bath could also be controlled to reduce the low frequency noise of the instrument.

The instrument has been used to carry out a preliminary null test of Newton's inverse square law of gravitation. The successful operation of the superconducting gradiometer in a rather simple setting demonstrates that the macroscopic quantum mechanical phenomenon exhibited in superconductivity can be taken advantage of to meet many practical challenges posed by sensitive gravity measurements. The careful modelling of the instrument and its experimental confirmation establishes the feasibility of constructing a more advanced superconducting gravity gradiometer and carrying out precision gravity experiments.

Guided by the theoretical and experimental work reported in Papers I and II, we are in the process of constructing a three-axis superconducting gravity gradiometer of an advanced design [6, 15]. The new gradiometer incorporates additional technical innovations such as a "superconducting negative spring" and a "three-dimensional residual common mode balance" as well as the cold

damping and force rebalance feedbacks to achieve an instrument noise level of 10^{-4} E $Hz^{-1/2}$ [16]. Such a sensitive and stable gradiometer will find important applications in inertial navigation and geophysical survey as well as in fundamental physics experiments. A series of precision inverse square law tests as well as tests of general relativistic effects are planned with this instrument both in the terrestrial laboratory and in space [17, 18]. The work presented here lays the ground work for further development of superconducting technology for gravity and acceleration measurements.

ACKNOWLEDGEMENTS

We wish to acknowledge valuable contributions from Drs. Evan Mapoles, Daniel DeBra, and Jean-Paul Richard in the design of the superconducting gravity gradiometer. We thank Bob Horne and Frank Desrosier for their skillful mechanical work in the fabrication of the gradiometer and supporting hardware. The 1.6 ton lead pendulum was constructed with the material provided by the National Bureau of Standards, Gaithersburg, Maryland. We have also benefited from collaboration with Qin Kong and Joel Parke.

APPENDIX A: VIBRATION ISOLATION BY PENDULUM ACTION

Isolation of horizontal vibrations by pendulum action has been analyzed in Ref. 7 by treating the angular motion of the pendulum in time domain. Here we treat the problem in frequency domain. For a platform suspended in a stationary laboratory, the angular amplitude of the pendulum is of the order of 10^{-6} rad at its resonance frequency. Effects that arise from second order contributions in angle will therefore be negligible in general.

1. Vibration Isolation of an Accelerometer

We first consider a single accelerometer mounted on a platform suspended by a symmetric pendulum of effective length ℓ_p, the distance between the pivot point and the "center of percussion" of the platform (see Fig. A1(a)). The effective length of the pendulum is defined from ω_p, the degenerate (angular) resonance frequency of the swinging mode, by

$$\ell_p \equiv g_E/\omega_p^2 \,. \tag{A1}$$

Let the center of mass of the accelerometer proof mass be located at a vertical distance ℓ_o below the pivot point with its sensitive axis defined by $\hat{n}$. We further assume a "perfectly rigid" pendulum in which the pendulum mass and the suspension rod form a perfectly rigid body and the pivot is perfectly rigid for linear motions while it is perfectly soft for angular motions. This condition could be approached in practice by designing the pendulum with the resonance frequencies of unwanted modes high compared to the swinging mode frequency ω_p.

Under these assumptions, the accelerometer platform is completely iso-

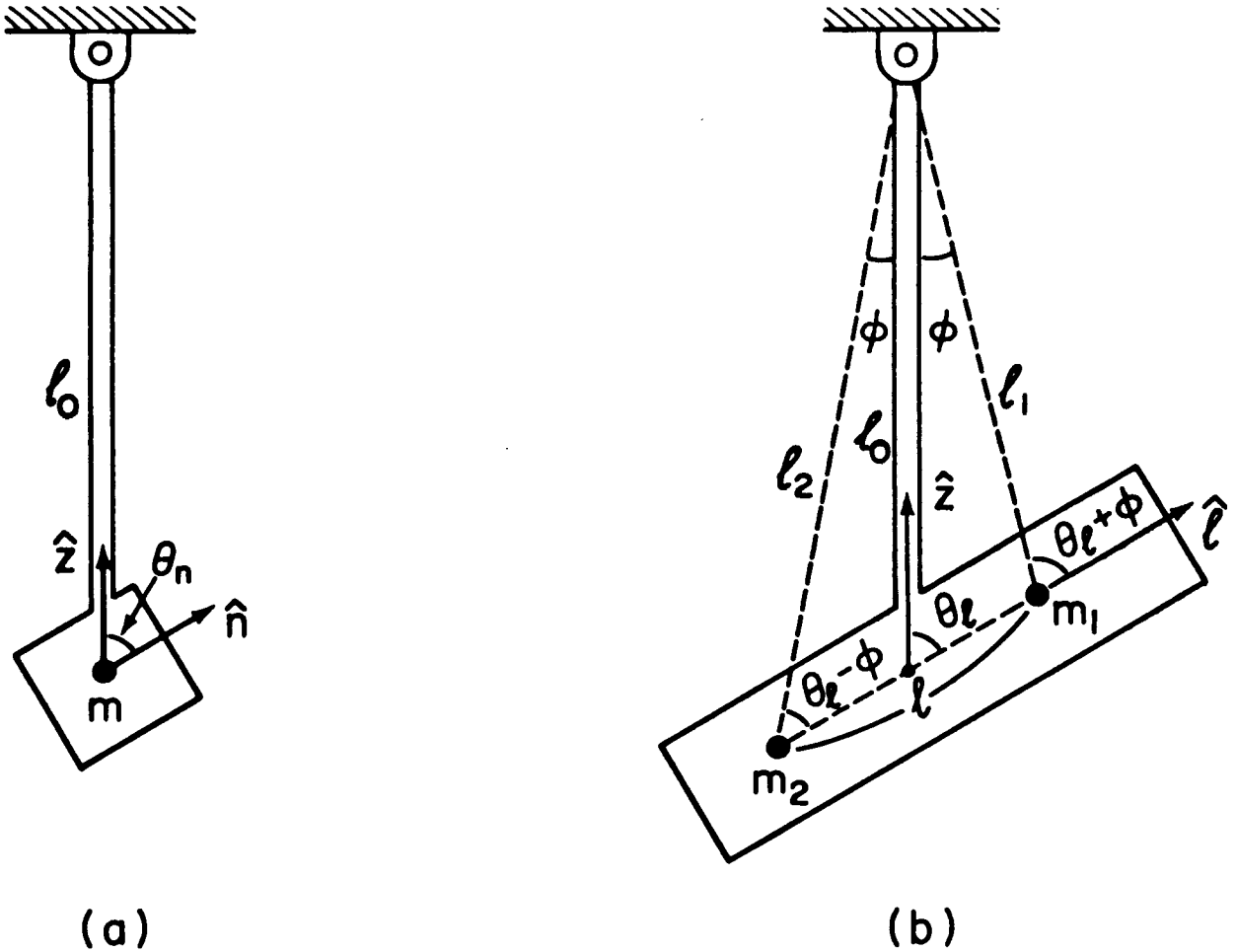

Fig. A1. Pendulum suspension of (a) an accelerometer and (b) a gradiometer.

lated from the angular motions of the ceiling from which the pendulum is suspended. This isolation is independent of frequency although, in practice, finite rigidity for the torsional mode tends to make the pendulum a low-pass filter for the torsional jitter of the external world. No attenuation is expected for vertical vibrations. Since linear accelerations can be balanced out in one direction in a gradiometer, our interest is in the extent to which horizontal accelerations $\vec{a}_h(t)$ can be rejected by means of the pendulum action.

Let us denote the horizontal displacements of the pivot point and the center of percussion of the platform by $\vec{R}_h(t)$ and $\vec{r}_h(t)$, respectively. Then, the equation of motion of the pendulum can be written as

$$\ddot{\vec{r}}_h + \tau_p^{-1}(\dot{\vec{r}}_h - \dot{\vec{R}}_h) + \omega_p^2(\vec{r}_h - \vec{R}_h) = 0. \qquad \text{(A2)}$$

Taking a Fourier transform of this equation, one finds

$$\vec{r}_h(\omega) = \frac{\omega_p^2 + j\omega\tau_p^{-1}}{\omega_p^2 - \omega^2 + j\omega\tau_p^{-1}} \vec{R}_h(\omega). \qquad \text{(A3)}$$

The horizontal acceleration of the platform is therefore

$$\vec{a}_h(\omega) = -\omega^2 \vec{r}_h(\omega) = \frac{\omega_p^2 + j\omega\tau_p^{-1}}{\omega_p^2 - \omega^2 + j\omega\tau_p^{-1}} \vec{A}_h(\omega), \qquad \text{(A4)}$$

where $\vec{A}_h(\omega) \equiv -\omega^2 \vec{R}_h(\omega)$ represents the external acceleration.

The resulting angular displacement of the platform in the Earth coordinate system is given by

$$\vec{\theta}_p(\omega) = \frac{1}{\ell_p} [\vec{r}_h(\omega) - \vec{R}_h(\omega)] \times \hat{z}, \qquad \text{(A5)}$$

to the first order in $\vec{\theta}_p$. Substitution of Eq. (A3) into Eq. (A5) leads to

$$\vec{\theta}_p(\omega) = \frac{-1}{\omega_p^2 - \omega^2 + j\omega\tau_p^{-1}} \frac{1}{\ell_p} \vec{A}_h(\omega) \times \hat{z} , \tag{A6a}$$

$$\vec{\Omega}_p(\omega) = j\omega \vec{\theta}_p(\omega) = \frac{-j\omega}{\omega_p^2 - \omega^2 + j\omega\tau_p^{-1}} \frac{1}{\ell_p} \vec{A}_h(\omega) \times \hat{z} , \tag{A6b}$$

$$\vec{\alpha}_p(\omega) = -\omega^2 \vec{\theta}_p(\omega) = \frac{\omega^2}{\omega_p^2 - \omega^2 + j\omega\tau_p^{-1}} \frac{1}{\ell_p} \vec{A}_h(\omega) \times \hat{z} . \tag{A6c}$$

Notice here that $\vec{\Omega}_p(\omega)$ represents the angular velocity of the platform with respect to Earth.

The total specific force acting on the accelerometer proof mass is

$$g'(t) = \hat{n}(t) \cdot [\vec{g}_E - \vec{a}_{ho}(t)], \tag{A7}$$

where $\vec{a}_{ho}(t)$ is the horizontal acceleration of the platform at the proof mass, which is given by a weighted average of $\vec{A}_h(t)$ and $\vec{a}_h(t)$:

$$\vec{a}_{ho}(t) = (1 - \frac{\ell_o}{\ell_p}) \vec{A}_h(t) + \frac{\ell_o}{\ell_p} \vec{a}_h(t). \tag{A8}$$

The Fourier transform of Eq. (A7) is

$$g(\omega) = \vec{\theta}_p(\omega) \times \hat{n} \cdot \vec{g}_E - \hat{n} \cdot \vec{a}_{ho}(\omega), \tag{A9}$$

to the first order in $\vec{\theta}_p$, where the vector identity (A11) of Paper I has been utilized to obtain $\hat{n}(\omega)$ and

$$\vec{a}_{ho}(\omega) = \frac{\omega_p^2 + j\omega\tau_p^{-1} - (1 - \ell_o/\ell_p)\omega^2}{\omega_p^2 - \omega^2 + j\omega\tau_p^{-1}} \vec{A}_h(\omega). \tag{A10}$$

Substitution of $\vec{g}_E = -g_E \hat{z}$ into Eq. (A9) gives the form:

$$g(\omega) = \hat{n} \cdot [g_E \vec{\theta}_p(\omega) \times \hat{z} - \vec{a}_{ho}(\omega)]. \qquad \text{(A11)}$$

Now, we substitute Eqs. (A6a) and (A10) to obtain

$$g(\omega) = \frac{(1 - \ell_o/\ell_p)\,\omega^2 - j\omega\tau_p^{-1}}{\omega_p^2 - \omega^2 + j\omega\tau_p^{-1}}\, \hat{n} \cdot \vec{A}_h(\omega), \qquad \text{(A12)}$$

where the main contributions to the two terms in Eq. (A11) have cancelled each other by Eq. (A1). Namely, the horizontal acceleration of the proof mass is almost exactly balanced out by the modulation of Earth's gravity which results from the tilt of the platform.

According to Eq. (A12), residual errors in the horizontal vibration isolation arises from two sources: misposition of the accelerometer proof mass ($\ell_o \neq \ell_p$) and damping ($Q_p = \omega_p\tau_p < \infty$). When $\ell_o = \ell_p$ is chosen, the attenuation obtained by the pendulum action goes as

$$\left|\frac{g(\omega)}{\hat{n} \cdot \vec{A}_h(\omega)}\right| \cong \begin{cases} (\omega/\omega_p)\, Q_p^{-1}, & \omega \ll \omega_p, \qquad \text{(A13a)} \\ 1, & \omega = \omega_p, \qquad \text{(A13b)} \\ (\omega_p/\omega)\, Q_p^{-1}, & \omega \gg \omega_p. \qquad \text{(A13c)} \end{cases}$$

At resonance, the platform is actually driven to an amplitude Q_p times larger, as can be seen from Eq. (A10), and the pendulum action balances the horizontal acceleration to Q_p^{-1} so that the net gain will be unity. Away from resonance, the horizontal acceleration is attenuated by Q_p^{-1} times a frequency factor

which helps the isolation further. Thus, we have proved that the pendulum suspension indeed provides wideband isolation of an accelerometer from horizontal accelerations as well as tilts except in the immediate vicinity of its resonance frequency.

We have assumed symmetry of the pendulum frequency in two horizontal directions for simplicity. Equation (A12) shows that this assumption is not necessary for the operation of the pendulum action. Since the accelerometer is not sensitive to a horizontal acceleration perpendicular to $\hat{n}$, the foregoing analysis will be valid as long as ℓ_o is chosen to be equal to the effective length of the pendulum ℓ_p in the vertical plane which includes $\hat{n}$.

2. Vibration Isolation of a Gravity Gradiometer

We now turn to a gradiometer mounted on a platform under pendulum suspension (Fig. A1(b)). In general, the two component accelerometers have slightly different sensitive axes, $\hat{n}_1$ and $\hat{n}_2$, and are located at different distances, ℓ_1 and ℓ_2, from the pivot point. The distance between the pivot point and the center of percussion, which is near the midpoint between the two proof masses, is denoted by ℓ_o. Since a very small differential acceleration signal is sought for in general, errors coupled through misalignments of the sensitive axes will have to be examined carefully. The result of a general analysis of the misalignment errors is given by Eq. (A6b) of Paper I, which can be written in the form:

$$\delta\Gamma_{\substack{\hat{n}+\hat{\ell}}}(t) = \frac{1}{\ell}\,\delta\hat{n}_{-} \cdot [\vec{g}_E - \vec{a}(t)]$$

$$+ (\delta\hat{n}_{\substack{\hat{}\\+n}} + \delta\hat{\ell}) \cdot [\vec{\Gamma}_E - \vec{\Omega}(t)\,\vec{\Omega}(t)] \cdot \hat{n} - \delta\hat{n}_{\substack{\hat{}\\+\ell}} \times \hat{n} \cdot \vec{\alpha}(t), \quad \text{(A14)}$$

where ℓ is the baseline of the gradiometer, and $\delta\hat{n}_-$, $\delta\hat{n}_{+\ell}$, $\delta\hat{n}_{+n}$, $\delta\hat{\ell}$ are the misalignment and misorientation vectors defined by Eqs. (92) - (94) of Paper I. The gravity gradient ($\vec{\Gamma}_E$) term can be ignored in comparison with the gravity ($\vec{g}_E$) term, and the correction term to centrifugal acceleration can be dropped since the full centrifugal acceleration is regarded as a separate error source in Paper II.

Upon Fourier transformation, Eq. (A14) becomes, to the first order in $\vec{\theta}_p$,

$$\delta\Gamma_{n+\ell}(\omega) = \frac{1}{\ell}\,\delta\hat{n}_- \cdot [g_E\vec{\theta}_p(\omega) \times \hat{z} - \vec{a}_{ho}(\omega)] + \delta\hat{n}_{+\ell} \times \hat{n} \cdot \vec{\alpha}_p(\omega), \quad \text{(A15)}$$

where appropriate quantities for the pendulum suspension have been substituted into the linear and angular accelerations. Here $\vec{a}_{ho}(\omega)$ is the horizontal acceleration of the midpoint between the two accelerometers. In deriving Eq. (A15), use has been made of the relationship between the accelerations at the two accelerometers, $\vec{a}_{hk}(\omega)$, and $\vec{a}_{ho}(\omega)$:

$$\left|\frac{\vec{a}_{hk}(\omega)}{\vec{a}_{ho}(\omega)}\right| = \frac{\ell_k}{\ell_o} = \frac{\sin\theta_\ell}{\sin\,[\theta_\ell - (-1)^k\,\phi]}\,, \quad \text{(A16)}$$

to obtain a perfect balance of the accelerations along the direction $\hat{\ell}$:

$$\hat{\ell} \cdot [\vec{a}_{h2}(\omega) - \vec{a}_{h1}(\omega)] = a_{h2}(\omega)\,\sin(\theta_\ell - \phi) - a_{h1}(\omega)\,\sin(\theta_\ell + \phi) = 0. \quad \text{(A17)}$$

The angles θ_ℓ and ϕ are defined in Fig. A1(b). In addition, we have assumed $\ell_o >> \ell$ to approximate

$$\frac{1}{2}\,\delta\hat{n}_- \cdot [\vec{a}_{h2}(\omega) + \vec{a}_{h1}(\omega)] \simeq \delta\hat{n}_- \cdot \vec{a}_{ho}(\omega)\,. \quad \text{(A18)}$$

Substitution of Eqs. (A6) and (A10) into Eq. (A15) results in

$$\delta \Gamma_{\hat{n}+\hat{\ell}}(\omega) = \frac{(1 - \ell_o/\ell_p)\,\omega^2 - j\omega\tau_p^{-1}}{\omega_p^2 - \omega^2 + j\omega\tau_p^{-1}} \frac{1}{\ell}\, \delta\hat{n}_- \cdot \vec{A}_h(\omega)$$

$$+ \frac{\omega^2}{\omega_p^2 - \omega^2 + j\omega\tau_p^{-1}} \frac{1}{\ell_p}\, \delta\hat{n}_{+\hat{\ell}} \times \hat{n} \cdot \vec{A}_h(\omega) \times \hat{z} \,. \qquad \text{(A19)}$$

The first term in Eq. (A19) is again minimized by choosing $\ell_o = \ell_p$; i.e., by locating the center of the gradiometer at the center of percussion of the platform. In this case, however, the horizontal acceleration couples in through the second term which represents the effect of the induced angular acceleration. In order to balance out $\vec{A}_h(\omega)$ in the two terms, ℓ_o should rather be chosen to satisfy

$$\left(\frac{\ell_p - \ell_o}{\ell}\right) \delta\hat{n}_- + (\hat{n} \cdot \hat{z})\, \delta\hat{n}_{+\hat{\ell}} - (\delta\hat{n}_{+\hat{\ell}} \cdot \hat{z})\, \hat{n} = 0. \qquad \text{(A20)}$$

Since there are three independent components in this equation, it is impossible in general to satisfy this equation by adjusting a single parameter ℓ_o even if $\delta\hat{n}_-$ and $\delta\hat{n}_{+\hat{\ell}}$ are predetermined. Therefore, in order to obtain a wide-band rejection of the horizontal accelerations in a gradiometer by means of the pendulum suspension, a sufficiently small value of $\delta\hat{n}_{+\hat{\ell}}$ is required.

An additional error term is generated through the centrifugal acceleration of the gradiometer proof masses induced by $\vec{A}_h(\omega)$. This error is given by Eq. (A10) of Paper I:

$$\delta\Gamma_{\vec{C}}(\omega) = -2\left[(\hat{n} \cdot \vec{\Omega}_E)\,\{\hat{n} \cdot \vec{\Omega}_p(\omega)\} - \vec{\Omega}_E \cdot \vec{\Omega}_p(\omega)\right], \qquad \text{(A21)}$$

where $\vec{\Omega}_E$ is the constant angular velocity of Earth. Substitution of Eq. (A6b)

into this equation yields

$$\delta\Gamma_{\vec{C}}(\omega) = \frac{j\omega}{\omega_p^2 - \omega^2 + j\omega\tau_p^{-1}} \frac{2}{\ell_p} [(\hat{n} \cdot \vec{\Omega}_E)\,\hat{n} - \vec{\Omega}_E] \cdot \vec{A}_h(\omega) \times \hat{z}. \quad \text{(A22)}$$

Combination of Eqs. (A19) and (A22) gives the total residual error arising from $\vec{A}_h(\omega)$:

$$\delta\Gamma_h(\omega) = \frac{\omega^2 \delta\hat{n}_{+\ell} \times \hat{n} + j\omega\, 2[(\hat{n} \cdot \vec{\Omega}_E)\,\hat{n} - \vec{\Omega}_E]}{\omega_p^2 - \omega^2 + j\omega\tau_p^{-1}} \cdot \frac{1}{\ell_p} \vec{A}_h(\omega) \times \hat{z} \quad \text{(A23)}$$

Equation (A23) shows that the pendulum works as an attenuator with an attenuation factor proportional to $(\ell/\ell_p)\,|\delta\hat{n}_{+\ell}|$ and $(\ell/\ell_p)(\Omega_E/\omega)$, respectively, for each error term, plus a high-pass filter with the cut-off frequency ω_p. Therefore, for a gradiometer, the pendulum action attenuates the horizontal accelerations at all frequencies, with the isolation becoming perfect as the signal frequency approaches dc. This is usually sufficient because the signal bandwidth satisfies $\omega < \omega_p$ in most applications of a gradiometer. It is truly remarkable that the pendulum action accomplishes a nearly perfect, passive vibration isolation in two dimensions near dc because vibration isolation below 1 Hz is very difficult to achieve by means of conventional spring-mass isolators.

In the frequency range $\omega > \Omega_E/|\delta\hat{n}_{+\ell}|$, the centrifugal acceleration term can be ignored in comparison with the angular acceleration term so that

$$\delta\Gamma_h(\omega) \cong \vec{h}_{\alpha}(\omega) \frac{1}{\ell_p} \delta\hat{n}_{+\ell} \times \hat{n} \cdot \vec{A}_h(\omega) \times \hat{z}\,, \quad \text{(A24)}$$

where

$$h_{\vec{\alpha}}(\omega) \equiv \frac{\omega^2}{\omega_p^2 - \omega^2 + j\omega\tau_p^{-1}} \tag{A25}$$

is the normalized transfer function for coupling of $\vec{A}_h(\omega)$ through induced angular acceleration. The absolute value of this function is plotted in Fig. A2 (solid line) for parameter values of $\omega_p/2\pi = 0.32$ Hz and $Q_p = \omega_p\tau_p = 300$. Also plotted in the figure (dotted line) for comparison is the absolute value of the transfer function for direct transmission of $\vec{A}_h(\omega)$ to the pendulum mass:

$$h_t(\omega) \equiv \frac{\omega_p^2 + j\omega\tau_p^{-1}}{\omega_p^2 - \omega^2 + j\omega\tau_p^{-1}}\ , \tag{A26}$$

which is read from Eq. (A4). Thus, the pendulum itself responds to the horizontal acceleration as a low-pass filter with a frequency characteristic given by Eq. (A26). Equation (A6a) shows that the induced angular displacement has an almost identical frequency response which cancels the direct transmission term to approximately Q_p^{-1}. What is left over after this cancellation is the frequency characteristic of a high-pass filter given by Eq. (A25).

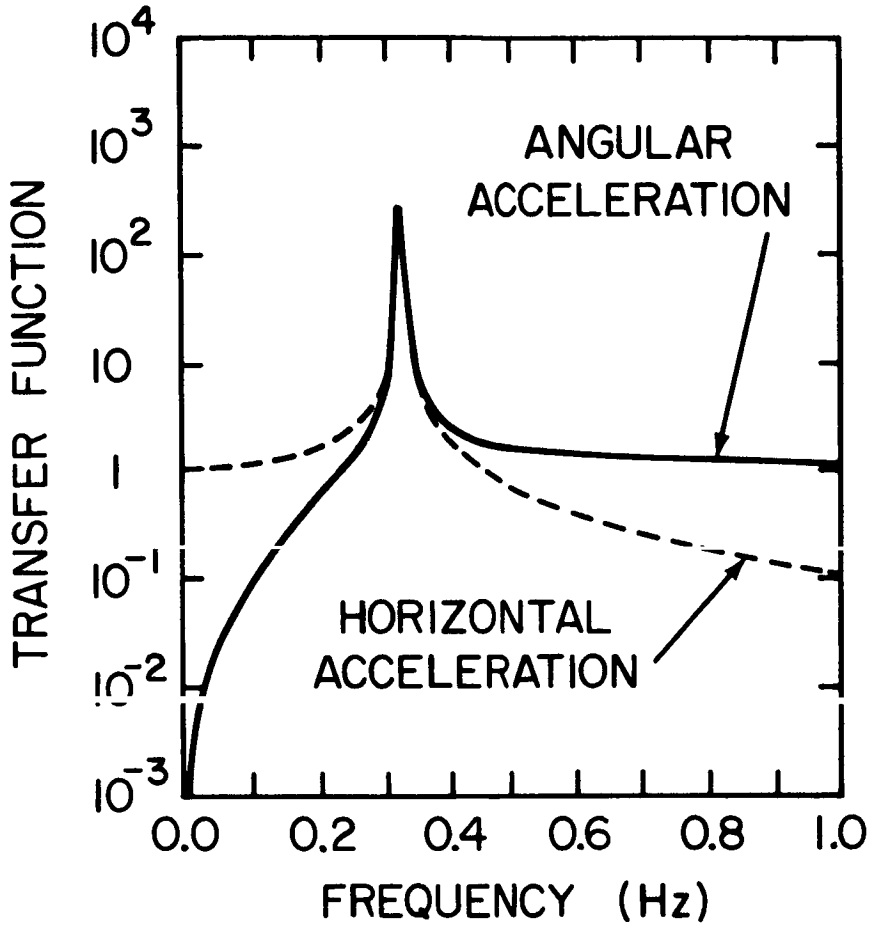

Fig. A2. Transfer functions of the pendulum suspension for horizontal accelerations.

APPENDIX B: LOW FREQUENCY NOISE OF THE GRADIOMETER

Gravity gradient signals of interest are usually at very low frequencies ($10^{-4} \sim 1$ Hz). Excess low frequency noise (red noise), which raises the overall instrument noise above the Brownian motion noise, is therefore of great concern in constructing a sensitive gravity gradiometer. Red noise in the gradiometer output can be generated by thermal and mechanical drift of the gradiometer, nonlinearities in the instrument, centrifugal acceleration of the platform, the 1/f noise and drift of the detecting electronics, etc. One way of overcoming certain types of such low frequency noise is an up-conversion of the gravity gradient signal by rotating the instrument followed by a heterodyne detection of the modulated signal [19]. The rotation, however, increases the centrifugal acceleration and introduces additional dynamically induced noise sources. In this Appendix, we analyze how various error mechanisms contribute to the excess low frequency noise for a non-rotating gravity gradiometer.

1. Temperature Drift

Temperature coefficients of the superconducting gravity gradiometer have been derived in Appendix of Paper I. It has been found that the dominant effect comes from the functional dependence of the penetration depth $\lambda(T)$ on temperature T. The good thermal conductivity through the gradiometer body makes the differential temperature fluctuation $T_d(\omega)$ negligible compared to the common temperature fluctuation $T_c(\omega)$. The temperature-induced error can therefore be written as

$$\delta g_{d,T}(\omega) = h_{Tc}(\omega)\ T_c(\omega), \qquad \text{(B1)}$$

where

$$h_{Tc}(\omega) \equiv [\alpha_2^T(\omega_{2\lambda}^2 - \omega^2) - \alpha_1^T(\omega_{1\lambda}^2 - \omega^2)]\ (1 + \zeta)\ \frac{d\lambda}{dT}\ , \qquad (B2)$$

and α_k^T, $\omega_{k\lambda}^2$ are defined by Eqs. (A42) and (A45) of Paper I, respectively, and $\zeta \lesssim 1$ is the modulation efficiency of the penetration depth for the pancake coils.

In the experiment, $i_k \cong 0$ was chosen so that

$$\alpha_k^T \cong \frac{L_{ka} - L_{kb}}{L_{ks}}\ , \qquad (B3)$$

$$\omega_{k\lambda} \cong \omega_{kM}. \qquad (B4)$$

Substituting into Eq. (B2) the measured values of these parameters listed in Table I and

$$\frac{d\lambda}{dT} = \frac{2\lambda(0)}{T_o}\ \frac{(T/T_o)^3}{[1 - (T/T_o)^4]^{3/2}} = 9.7 \times 10^{-10}\ \text{m/K} \qquad (B5)$$

for Nb at T = 4.2 K, one obtains

$$\varepsilon_n^T(\omega) \equiv \frac{1}{\ell}\ h_{Tc}(\omega) = -\ 2.9 \times 10^4\ E\ K^{-1}, \qquad \omega << \omega_{kM}\ , \qquad (B6)$$

for the present gradiometer.

Thus far the temperature-induced error has been analyzed in the frequency domain. Although this description is complete, it is often convenient to measure and compensate for the temperature effect in real time. Notice that $h_{Tc}(\omega)$ becomes independent of ω when $\omega << \omega_{k\lambda}$. Therefore, for a slow drift

with $t \gg \omega_{k\lambda}^{-1}$, one expects a linear relationship:

$$\delta g_{d,T}(t) = h_{Tc}\, T_c(t) \ , \tag{B7}$$

where

$$h_{Tc} \cong h_{Tc}\ (\omega = 0) \ . \tag{B8}$$

The observed noise $T_c(t)$ in time domain can be related to the power spectral density $S_T(f)$ by a standard formula for the digital FFT (fast Fourier transform) [20]:

$$S_T(f) = \left\langle \frac{2}{\tau} \left| \int_{-\tau/2}^{\tau/2} T_c(t)\, e^{-j2\pi ft}\, dt \right|^2 \right\rangle, \tag{B9}$$

where τ is the sample length. For a linear drift,

$$T_c(t) = at, \tag{B10}$$

this equation yields

$$S_T(f) = \frac{\tau}{4\pi^2} \frac{\langle a^2 \rangle}{f^2} \ , \ f \gtrsim \frac{1}{\pi\tau} \ . \tag{B11}$$

Notice that the result depends on the choice of τ. Combination of Eqs. (B1) and (B9) leads to

$$S_{T,T}(f) = \left(\varepsilon_n^T\right)^2 \frac{\tau}{4\pi^2} \frac{\langle a^2 \rangle}{f^2} \ . \tag{B12}$$

Thus, a linear temperature drift causes a $1/f^2$ power spectrum at the gradiometer output.

In the experiment, the gradiometer was thermally isolated from the He bath through vacuum. The large heat capacity of the gradiometer body and the low conductivity through the electrical leads and the residual He gas formed a low-pass RC filter for heat flow with a transfer function:

$$h_F(f) = \frac{1}{1 + j2\pi f\tau_F} , \tag{B13}$$

where τ_F is the filter time constant. In high vacuum, τ_F exeeded 10^3 s. In fact, we had to maintain a pressure level of approximately 10^{-4} mm Hg to bring the gradiometer assembly into thermal equilibrium with the He bath in a reasonable time after turning on heat-switches on the gradiometer. A typical response time used was $\tau_F \cong 500$ s. A Ge thermometer was mounted on the gradiometer assembly to measure $T_c(t)$. However, the thermometer did not have enough resolution to track the stable temperature of the gradiometer. All we could determine directly is a rough estimate of the experimental upper limit, 2×10^{-4} K hr^{-1}, for dT_c/dt so that

$$a_{rms} \lesssim 5.6 \times 10^{-8} \text{ K s}^{-1}. \tag{B14}$$

Substituting τ = 125 s, the sampling time used for the spectrum analyzer, and Eqs. (B6) and (B14) into Eq. (B12), we obtain

$$[S_{T,T}(f)]^{1/2} \lesssim 2.9 \times 10^{-2} \text{ E Hz}^{-1/2} \left(\frac{0.1 \text{ Hz}}{f}\right). \tag{B15}$$

In a separate experiment [8], the temperature of the He bath was measured

by dipping a "superconducting penetration depth thermometer" of the type similar to the one described in Ref. 21 into a storage dewar. The Fourier analysis of this data is shown in Fig. B1. This data indicates that, in the frequency range of interest between 10^{-2} Hz and 10^{-1} Hz, the spectrum can be described by

$$[S_T(f)]^{1/2}_{Bath} = 1.1 \times 10^{-4} \text{ K Hz}^{-1/2} \left(\frac{0.1 \text{ Hz}}{f}\right). \qquad \text{(B16)}$$

Since the exact behavior of the temperature noise should depend on the characteristics of the dewar and the insert as well as the barometric pressure fluctuation in the laboratory, this data should be interpreted as an order-of-magnitude estimate for the temperature noise in our experiment. Combining Eq. (B16) with Eqs. (B6) and (B13), one finds

$$[S_{\Gamma,T}(f)]^{1/2} \cong \frac{1}{2\pi f \tau_F} \varepsilon_n^T [S_T(f)]^{1/2}_{Bath} = 1.0 \times 10^{-2} \text{ E Hz}^{-1/2} \left(\frac{0.1 \text{ Hz}}{f}\right)^2. \qquad \text{(B17)}$$

This estimate falls within the approximate limit given by Eq. (B15).

2. General Consideration of Nonlinear Effects

Since nonlinearity is a higher order effect, the most important error coupling mechanisms will involve the second order nonlinearity. Thus we restrict our discussion to a nonlinear behavior of the form:

$$\delta g_{d,N}(t) = \int_{-\infty}^{\infty} h_N(t - t')\, g^2(t')\, dt'. \qquad \text{(B18)}$$

The driving acceleration g(t) could be either $g_c(t)$ or $g_d(t)$. In this section, we wish to obtain a relationship between the Fourier components $g(\omega)$

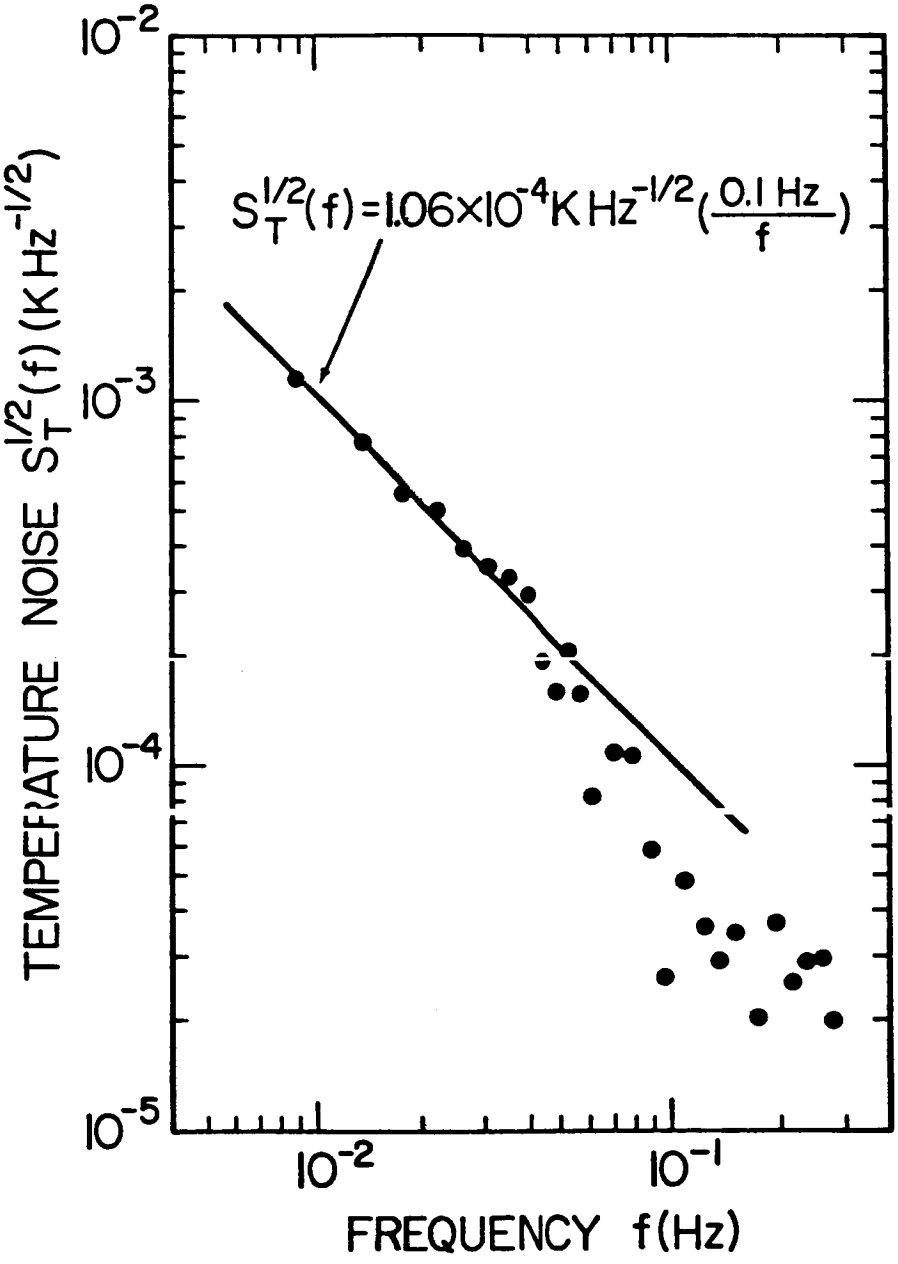

Fig. B1. Temperature noise spectrum of a liquid helium bath.

and $\delta g_{d,N}(\omega)$, and investigate specifically how the wideband noise $g(\omega)$ contributes to a low frequency divergence in $\delta g_{d,N}(\omega)$ through the squaring process.

The Fourier transform of Eq. (B18) is

$$\delta g_{d,N}(\omega) = h_N(\omega)\ G(\omega), \tag{B19}$$

where $G(\omega)$ is the Fourier transform of

$$G(t) \equiv g^2(t). \tag{B20}$$

In experiments, one usually measures <u>one-sided</u> power spectral densities as functions of $f = \omega/2\pi > 0$ rather than ω. Equation (B19) implies a relationship for such power spectral densities:

$$S_{\Gamma,N}(f) = \frac{1}{\ell^2}\ |h_N(f)|^2\ S_G(f), \tag{B21}$$

where $h_N(f) = h_N(\omega)$ and $S_G(f)$ is related to $S_g(f)$ by a convolution [22]:

$$\tilde{S}_G(f) = \int_{-\infty}^{\infty} \tilde{S}_g(f')\ \tilde{S}_g(f - f')\ df'. \tag{B22}$$

The tilde ($\sim$) represents two-sided spectral densities with a property:

$$\tilde{S}(-f) = \tilde{S}(f) = \frac{1}{2}\ S(f)\ ,\ f > 0. \tag{B23}$$

For a sinusoidal function with <u>random phase</u>,

$$g(t) = g \cos (2\pi f_o t + \theta), \tag{B24}$$

it is straightforward to show [23]

$$\tilde{S}_g(f) = \frac{1}{4} g^2 [\delta(f - f_o) + \delta(f + f_o)], \tag{B25}$$

$$\tilde{S}_G(f) = \frac{1}{16} g^4 [\delta(f - 2f_o) + 4\delta(f) + \delta(f + 2f_o)]. \tag{B26}$$

In practice, the δ-functions in these equations are replaced by continuous functions with finite peaks and widths due to the finite sample length τ used in the computation of the spectral densities. Denoting this narrowband response function with a subscript τ, the one-sided spectral densities can be written as

$$S_g(f) = \frac{1}{2} g^2 \delta_\tau(f - f_o), \tag{B27}$$

$$S_G(f) = \frac{1}{8} g^4 [2\delta_{\tau/2}(f) + \delta_{\tau/2}(f - 2f_o)], \tag{B28}$$

where the line broadening by a factor 2 that takes place in the squaring operation [22] has been indicated by $\tau/2$. Notice that the factor 1/2 in front of g^2 comes from the assumption that the phase θ of the signal is random. For a signal in phase with the reference signal, $g^2/2$ must be replaced by g^2 in Eqs. (B27) and (B28).

The exact line shape $\delta_\tau(f)$ depends on the window function employed in the Fourier analysis. A simple box-car shape window yields

$$\delta_\tau(f) = \delta_\tau^B(f) \equiv \int_{-\tau/2}^{\tau/2} e^{-j2\pi ft}\, dt = \frac{\sin(\pi f\tau)}{\pi f}. \tag{B29}$$

In the experiment, a Hanning window function [23] with the characteristic

$$\delta_\tau^H(f) \equiv \frac{1}{4}\,\delta_\tau^B(f - \frac{1}{\tau}) + \frac{1}{2}\,\delta_\tau^B(f) + \frac{1}{4}\,\delta_\tau^B(f + \frac{1}{\tau}) \tag{B30}$$

was used. Substitution of Eq. (B29) into Eq. (B30) leads to

$$\delta_\tau(f) = \delta_\tau^H(f) = \frac{\sin(\pi f\tau)}{2\pi f}\,\frac{1}{1 - (f\tau)^2}\,. \tag{B31}$$

Notice that the Hanning filter produces a tail that goes as f^{-3}.

In the frequency range $2/\tau \lesssim f \lesssim f_o$, Eq. (B28) can now be approximated as

$$S_G(f) \cong \frac{g^4}{2\pi\tau^2}\,\frac{1}{f^3}\,. \tag{B32}$$

In the general case when $S_g(f)$ is continuous, $g^2/2$ must be replaced by an integral of $S_g(f)$ over all frequencies so that

$$S_G(f) \cong \frac{2}{\pi\tau^2}\,\frac{1}{f^3}\,[\int_o^\infty S_g(f')\,df']^2. \tag{B33}$$

Substituting this into Eq. (B21), one obtains the final result:

$$[S_{\Gamma,N}(f)]^{1/2} \cong (\frac{2}{\pi})^{1/2}\,\frac{1}{\ell\tau}\,\frac{1}{f^{3/2}}\,|h_N(f)|\,\int_o^\infty S_g(f')\,df'. \tag{B34}$$

Notice that $S_{\Gamma,N}(f)$ can be reduced by increasing the sample length τ.

The nonlinearity coefficient $|h_N(f)|$ can be measured by driving the system with a sinusoidal acceleration at the frequency $f/2$:

$$g_F(t) = g_F \cos(\pi f t + \theta_F), \tag{B35}$$

and observing the resulting gradient at its second harmonic f:

$$\Gamma_S(t) = \frac{1}{\ell} g_S \cos (2\pi ft + \theta_S). \qquad \text{(B36)}$$

From the foregoing analysis, it is easily seen that

$$g_S = \frac{1}{2} |h_N(f)| g_F^2 . \qquad \text{(B37)}$$

The value of $|h_N(f)|$ obtained from this relationship could then be substituted into Eq. (B34).

3. Nonlinearities of the Instrument

A general expression of the nonlinearity errors was given in Paper I:

$$\delta g_{d,N}(\omega) = h_{cc}(\omega)\, G_{cc}(\omega) + h_{dd}(\omega)\, G_{dd}(\omega) + h_{cd}(\omega)\, G_{cd}(\omega), \quad \text{(B38)}$$

where $G_{cc}(\omega)$, $G_{dd}(\omega)$ and $G_{cd}(\omega)$ are the Fourier transforms of $[g_c(t)]^2$, $[g_d(t)]^2$ and $g_c(t)g_d(t)$. The derivation of the nonlinearity coefficients in this equation requires knowledge of experimental details.

We divide nonlinear mechanisms into three classes: 1) the instrument scale factor nonlinearity internal to the gradiometer, 2) dynamical nonlinear effects in which second order terms are produced by the finite compliance of the gradiometer structure in undesirable directions, and 3) nonlinear effects of the platform. The first class of nonlinearity can be overcome by linearizing the gradiometer by means of a "force rebalance" feedback; i.e. by operating the gradiometer as a null detector in a feedback circuit. This method, however, will not suppress the latter two classes of nonlinearity

errors inasmuch as these nonlinear effects are produced external to the instrument. In the pendulum-suspended platform, the third class of nonlinearity is produced by the centrifugal acceleration of the platform. In this section, we discuss the first two classes of nonlinearity, deferring the treatment of the third class to the following section.

The scale factor nonlinearity can come from a failure of Hooke's law in the mechanical front end ($\partial x/\partial g$), from a nonlinear response of the transducer ($\partial i/\partial x$), and from nonlinearity in the gain of the amplifier ($\partial V/\partial i$) (see Fig. 1 of Paper I). Since the SQUID operates in a negative feedback mode, it is a highly linear device and $\partial V/\partial i$ can be regarded as a constant. Further, the "cantilever" suspension spring for the proof masses has been specially designed to achieve a high degree of linearity along the sensitive axis. However, the transfer function $\partial i/\partial x$ of the superconducting transducer is intrinsically nonlinear, as can be seen in Eqs. (19), (25), and (32) of Paper I. The second order terms in the transducer transfer functions vanish if $L_a = L_b$ (symmetric coils) and $i = 0$ (absence of symmetric current). The first condition, however, is difficult to satisfy in practice because the spacings between the coils and the surfaces of the proof masses are not easily matched.

In order to obtain relationships between the nonlinearity coefficients of the component acceleration transducers and of the gradiometer, we expand the current responses $i_k(t)$ of individual transducers as functions of driving accelerations $g_k(t)$:

$$i_k(t) = h^k_{gi}\, g_k(t) + h^k_{Gi}\, g^2_k(t) + \cdots \equiv h^k_{gi}\, [g_k(t) + C^N_k\, g^2_k(t) + \cdots]. \quad \text{(B39)}$$

Here an instantaneous response of the circuit has been assumed because of the low frequency nature of the signals under investigation. The coefficients of

the linear terms are matched by the common mode balance of the gradiometer so that the gradiometer output can be written as

$$g_d'(t) = g_d(t) + (C_2^N - C_1^N)\ [g_c^2(t) + \frac{1}{4}\, g_d^2(t)] + (C_1^N + C_2^N)\ g_c(t)g_d(t) + \cdots . \tag{B40}$$

The transition from Eq. (B39) to Eq. (B40) is approximate because the electrical coupling between the two component transducers affects C_k^N, as they are combined into a gradiometer. Taking the Fourier transform of this equation and comparing it with Eq. (B38), one can identity

$$h_{cc}(\omega) \cong 4h_{dd}(\omega) \cong C_2^N - C_1^N\ , \tag{B41a}$$

$$h_{cd}(\omega) \cong C_1^N + C_2^N\ . \tag{B41b}$$

Notice that nonlinearity arises in the gradiometer even when the nonlinearity coefficients of the individual acceleration transducers are matched: i.e., $C_1^N = C_2^N$. The only way to eliminate the nonlinearity from the gradiometer scale factor is by making $C_1^N = C_2^N = 0$.

In the low frequency limit, one can derive an <u>approximate</u> relationship:

$$C_k^N \cong \frac{1}{\omega_{kM}^2}\ \frac{\Lambda}{L_{kp} + 2L_o}\ \frac{L_{ka} - L_{kb}}{L_{ka} + L_{kb}} \cong \left(\frac{1}{\omega_M^2\ \bar{d}_L}\ \frac{L_a - L_b}{L_a + L_b}\right)_k , \tag{B42}$$

where $\bar{d}_L$ is the average coil-to-proof-mass spacing. Substituting values listed in Table 1, we find $C_1^N \cong -7.5 \times 10^{-2}\ (\mathrm{m\ s^{-2}})^{-1}$ and $C_2^N \cong -1.7 \times 10^{-1}\ (\mathrm{m\ s^{-2}})^{-1}$ so that

$$h_{cc}(\omega) \cong 4h_{dd}(\omega) \cong -1.0 \times 10^{-1} \ (m\ s^{-2})^{-1}, \tag{B43a}$$

$$h_{cd}(\omega) \cong -2.5 \times 10^{-1} \ (m\ s^{-2})^{-1}. \tag{B43b}$$

These values must be considered only as order-of-magnitude estimates in view of the approximations used in the derivation.

The dynamic nonlinearity of the instrument arises from the finite compliance of the gradiometer structure which allows the misalignment angles $\delta\hat{n}_-$ and $\delta\hat{n}_{+\ell}$ to be driven by external accelerations $\vec{a}(t)$ or $\vec{\alpha}(t)$. From Eq. (A6b) of Paper I, it is clear that a nonlinearity error arises if $\delta\hat{n}_-$ or $\delta\hat{n}_{+\ell}$ is proportional to $\vec{a}(t)$ or $\vec{\alpha}(t)$. A bending mode of the structure can be excited by the perpendicular component of $\vec{a}(t)$ or $\vec{\alpha}(t)$ applied to the midpoint between the two accelerometers. The symmetry of the induced motion is such that the sensitive axes of the component accelerometers, $\hat{n}_1$ and $\hat{n}_2$, go out of alignment with respect to the baseline vector $\hat{\ell}$, with opposite signs for $\vec{a}(t)$, and with an equal sign for $\vec{\alpha}(t)$. Therefore, the induced misalignments have functional forms given by

$$\delta\hat{n}_-(t - t') = h_{\vec{a}\vec{a}}(t - t')\ \vec{a}_\perp(t'), \tag{B44a}$$

$$\delta\hat{n}_{+\ell}(t - t') = h_{\vec{\alpha}\vec{\alpha}}(t - t')\ \vec{\alpha}_\perp(t'), \tag{B44b}$$

where the history dependence of the coupling coefficients has resulted from the resonant response. Equation (A6b) of Paper I is then generalized into

$$\delta g_{d,N}(t) = -\int_{-\infty}^{\infty} [\delta\hat{n}_-(t-t') \cdot \vec{a}(t') + \ell\ \delta\hat{n}_{+\ell}(t-t') \times \hat{n} \cdot \vec{\alpha}(t')]\ dt'. \tag{B45}$$

The general form (B18) is obtained if Eqs. (B44) are substituted into Eq. (B45). The corresponding equation for frequency domain is

$$\delta g_{d,N}(\omega) = h_{\substack{\rightarrow\rightarrow \\ aa}}(\omega)\, G_{\substack{\rightarrow\rightarrow \\ aa}}(\omega) + h_{\substack{\rightarrow\rightarrow \\ \alpha\alpha}}(\omega)\, G_{\substack{\rightarrow\rightarrow \\ \alpha\alpha}}(\omega), \tag{B46}$$

where $G_{\substack{\rightarrow\rightarrow \\ aa}}(\omega)$ and $G_{\substack{\rightarrow\rightarrow \\ \alpha\alpha}}(\omega)$ are the Fourier transforms of $a_\perp^2(t)$ and $\alpha_\perp^2(t)$, respectively.

The coefficient $h_{\substack{\rightarrow\rightarrow \\ aa}}(\omega)$ has been computed [24] for a circular tube that connects the two accelerometers. We only quote the result here:

$$\left|h_{\substack{\rightarrow\rightarrow \\ aa}}(\omega)\right| = \frac{3}{\ell\omega_B^2}\left[1 + \frac{1}{Q_B^2}\left(\frac{\omega}{\omega_B}\right)^2\right]^{1/2} f\left(\frac{\omega}{\omega_B}\right), \tag{B47}$$

where

$$f(r) \equiv \left[(1 - r^2) + Q_B^{-2}\, r^2\right]^{-1/2}. \tag{B48}$$

Here ω_B and Q_B represent the (angular) resonance frequency and the quality factor of the bending mode involved. A similar result is expected for $\left|h_{\substack{\rightarrow\rightarrow \\ \alpha\alpha}}(\omega)\right|$.

Experimentally, the mounting cube for the gradiometer was made rather rigid so that $\omega_B/2\pi \gtrsim 300$ Hz. This gives upper limits for the nonlinearity error coefficients:

$$\left|h_{\substack{\rightarrow\rightarrow \\ aa}}(\omega)\right| \cong \left|h_{\substack{\rightarrow\rightarrow \\ \alpha\alpha}}(\omega)\right| \lesssim 4.7 \times 10^{-6}\ (\mathrm{m\ s^{-2}})^{-1}\ , \quad \omega < \omega_B. \tag{B49}$$

This is completely negligible compared to the coefficients of the scale factor nonlinearity, evaluated in Eqs. (B43). Unlike the latter, however, the former

cannot be reduced by means of feedback operation of the instrument. It can therefore become a dominant source of nonlinearity when a very sensitive gradiometer is operated in the force rebalance mode. Further, larger values of $h_{\vec{a}\vec{a}}(\omega)$ and $h_{\vec{\alpha}\vec{\alpha}}(\omega)$ may arise under certain conditions from undesirable modes of the suspension springs of the proof masses which are much more compliant than the mounting structure of the gradiometer.

Experimental values for the scale factor nonlinearity coefficients can be obtained in principle from the curvature of the calibration curve of the instrument. In the calibration data displayed in Figs. 7 and 12, however, the stochastic measurement error was too large to determine a systematic departure from a linear response. Only an upper limit for $C_1^N + C_2^N$ can be obtained from Fig. 7. For an applied acceleration $g_c \cong 4 \times 10^{-2}$ m s^{-2}, the current response lies within 5 % from the linear fit of the data. Equation (B39) then implies

$$\frac{1}{2} (C_1^N + C_2^N) g_c^2 \lesssim 0.05 g_c \qquad \text{(B50)}$$

or

$$C_1^N + C_2^N \lesssim 0.1 g_c^{-1} = 2.5 (\text{m s}^{-2})^{-1}. \qquad \text{(B51)}$$

The predicted value for $C_1^N + C_2^N$, given by Eq. (B43b), is an order of magnitude smaller than this experimental limit.

Using the nonlinearity coefficients predicted by Eqs. (43), one can compute the contribution of the scale factor nonlinearity to the low frequency noise spectrum of the gradiometer. The total common acceleration measured in the experiment is approximately

$$\int_o^\infty S_g(f')\, df' \lesssim 10^{-10}\ (m\ s^{-2})^2. \qquad (B52)$$

Substituting this and $|h_{cc}(f)| = 0.1\ (m\ s^{-2})^{-1}$, $\ell = 0.16$ m, $\tau = 125$ s into Eq. (B34), we find

$$[S_{\Gamma,cc}(f)]^{1/2} \lesssim 1 \times 10^{-2}\ E\ Hz^{-1/2}\ \left(\frac{0.1\ Hz}{f}\right)^{3/2}. \qquad (B53)$$

Effects coming from terms involving $g_d(t)$ can be shown to be many orders of magnitude smaller.

4. Centrifugal Acceleration

Here we consider nonlinear effects of the platform which convert external accelerations into low frequency acceleration noise of the platform, which then couples into the gradiometer by the linear transfer function of the instrument. A well-known nonlinear mechanism of the platform is its angular motion driven by an external acceleration. The resulting centrifugal acceleration is a second order effect.

An accelerometer mounted on the pendulum-suspended platform will experience a centrifugal acceleration $\vec{a}_C(t)$, in the radial direction away from the pivot point, with a magnitude:

$$a_C(t) = \ell_p\, \Omega_p^2(t). \qquad (B54)$$

For sinusoidal motions:

$$\Omega_p(t) = \Omega_p \cos\ (\omega t/2 + \theta_\Omega), \qquad (B55)$$

$$a_C(t) = a_C \cos(\omega t + \theta_a) + a_{Co}, \tag{B56}$$

the amplitudes are related by

$$a_C = \frac{1}{2} \ell_p \Omega_p^2 . \tag{B57}$$

By using Eqs. (A6b) and (A12), Ω_p can be related to the apparent acceleration g_F measured by the accelerometer at the fundamental frequency f/2:

$$\Omega_p = \frac{1}{|\hat{n} \cdot (\hat{\Omega} \times \hat{z})|} \frac{Q_p}{\ell_p \omega_p} g_F, \tag{B58a}$$

where $\hat{\Omega} \equiv \vec{\Omega}_p / \Omega_p$ is the unit vector along the direction of $\vec{\Omega}_p$ and $\ell_o = \ell_p$ has been assumed. Likewise, a_C can be related to the acceleration g_S measured by the accelerometer at the second harmonic f:

$$a_C = \frac{1}{|\hat{n} \cdot \hat{z}|} g_S. \tag{B58b}$$

Substitution of Eqs. (B58) into Eq. (B57) leads to Eq. (B37) with the identification:

$$|h_N(f)| = \frac{|\hat{n} \cdot \hat{z}|}{|\hat{n} \cdot (\hat{\Omega} \times \hat{z})|^2} \frac{Q_p^2}{g_E} , \tag{B59}$$

where Eq. (A1) has been used. The quantity $|h_N(f)|$ is the coefficient of apparent nonlinearity of an accelerometer suspended by a pendulum.

When $\ell_o \neq \ell_p$ for the accelerometer, Eq. (B58a) must be replaced by

$$\Omega_p = \frac{1}{|\hat{n} \cdot (\hat{\Omega} \times \hat{z})|} \frac{1}{(1 - \ell_o/\ell_p)\, \pi \ell_p f} g_F, \tag{B58a'}$$

so that

$$|h_N(f)| = \frac{|\hat{n} \cdot \hat{z}|}{|\hat{n} \cdot (\hat{\Omega} \times \hat{z})|^2} \frac{1}{(1 - \ell_o/\ell_p)^2 \, g_E} \left(\frac{2f_p}{f}\right)^2 . \qquad \text{(B59')}$$

Therefore, the magnitude of apparent nonlinearity coefficient depends on how well the horizontal acceleration is rejected by the pendulum action.

For a gradiometer mounted on the same platform, ℓ_p should be replaced by ℓ in Eq. (B54) so that

$$a_C = \frac{1}{2} \ell \, \Omega_p^2 . \qquad \text{(B60)}$$

With the aid of Eqs. (A6b) and (A19), Ω_p and a_C can be related to the <u>apparent differential acceleration</u> signals g_F and g_S at f/2 and f, respectively:

$$\Omega_p = \frac{1}{|\delta \hat{n}_{+\hat{\ell}}|} \frac{1}{\pi \ell f} g_F , \qquad \text{(B61a)}$$

$$a_C = \frac{1}{1 - (\hat{n} \cdot \hat{\Omega})^2} g_S , \qquad \text{(B61b)}$$

where $\ell_o = \ell_p$ is assumed so that the second term dominates in Eq. (A19). Substituting Eqs. (B61) into Eq. (B60), we find

$$|h_N(f)| = \frac{1 - (\hat{n} \cdot \hat{\Omega})^2}{|\delta \hat{n}_{+\hat{\ell}}|} \frac{\ell_p}{g_E \ell} \left(\frac{2f_p}{f}\right)^2 . \qquad \text{(B62)}$$

This is the coefficient of <u>apparent nonlinearity of a gradiometer</u> suspended by a pendulum.

We now evaluate $|h_N(f)|$ numerically for the gravity gradiometer in the umbrella orientation for three modes of operation: 1) common accelerometer

mode, 2) single accelerometer mode, and 3) gradiometer mode. For the particular orientation chosen, one finds $\hat{n} \cdot \hat{z} = 1/\sqrt{3}$, $\hat{n} \cdot \hat{\Omega} = 0$, $\hat{n} \cdot (\hat{\Omega} \times \hat{z}) = \sqrt{2/3}$. The condition $\ell_o = \ell_p$ is satisfied for the common mode and the gradiometer mode. For the single accelerometer mode, one can show that

$$\left|1 - \frac{\ell_o}{\ell_p}\right| = \frac{1}{2} (\hat{n} \cdot \hat{z}) \frac{\ell}{\ell_p} = \frac{1}{2\sqrt{3}} \frac{\ell}{\ell_p} . \qquad \text{(B63)}$$

Substituting $\ell = 0.16$ m, $\ell_p = 2.4$ m, $Q_p = 300$, and $|\delta \hat{n}_{\hat{+\ell}}| = 7 \times 10^{-4}$ into Eqs. (B59), (B59'), and (B62), we obtain the following theoretical predictions:

$$|h_N(f)|_{th} = \begin{cases} 8.0 \times 10^3 \ (\text{m s}^{-2})^{-1}, & \text{common accelerometer,} \\ 2.4 \times 10^2 \ (\text{m s}^{-2})^{-1} \left(\frac{2f_p}{f}\right)^2, & \text{single accelerometer,} \\ 3.0 \times 10^6 \ (\text{m s}^{-2})^{-1} \left(\frac{2f_p}{f}\right)^2, & \text{gradiometer.} \end{cases} \qquad \text{(B64)}$$

In the experiment, we were able to observe $|h_N(f)|$ at $f = 2f_p$ by detecting the second harmonic amplitudes for the swinging mode of resonance frequency $f_p = 0.32$ Hz. Figure B2 shows the data for the common accelerometer mode (crosses), the single accelerometer mode (dots), and the gradiometer mode (triangles). The experimental values of $|h_N(2f_p)|$ are determined from these graphs with the aid of Eq. (B37):

$$|h_N(2f_p)|_{ex} = \begin{cases} 5.6 \times 10^3 \ (\text{m s}^{-2})^{-1}, & \text{common accelerometer,} \\ 4.6 \times 10^2 \ (\text{m s}^{-2})^{-1}, & \text{single accelerometer,} \\ 4.4 \times 10^6 \ (\text{m s}^{-2})^{-1}, & \text{gradiometer.} \end{cases} \qquad \text{(B65)}$$

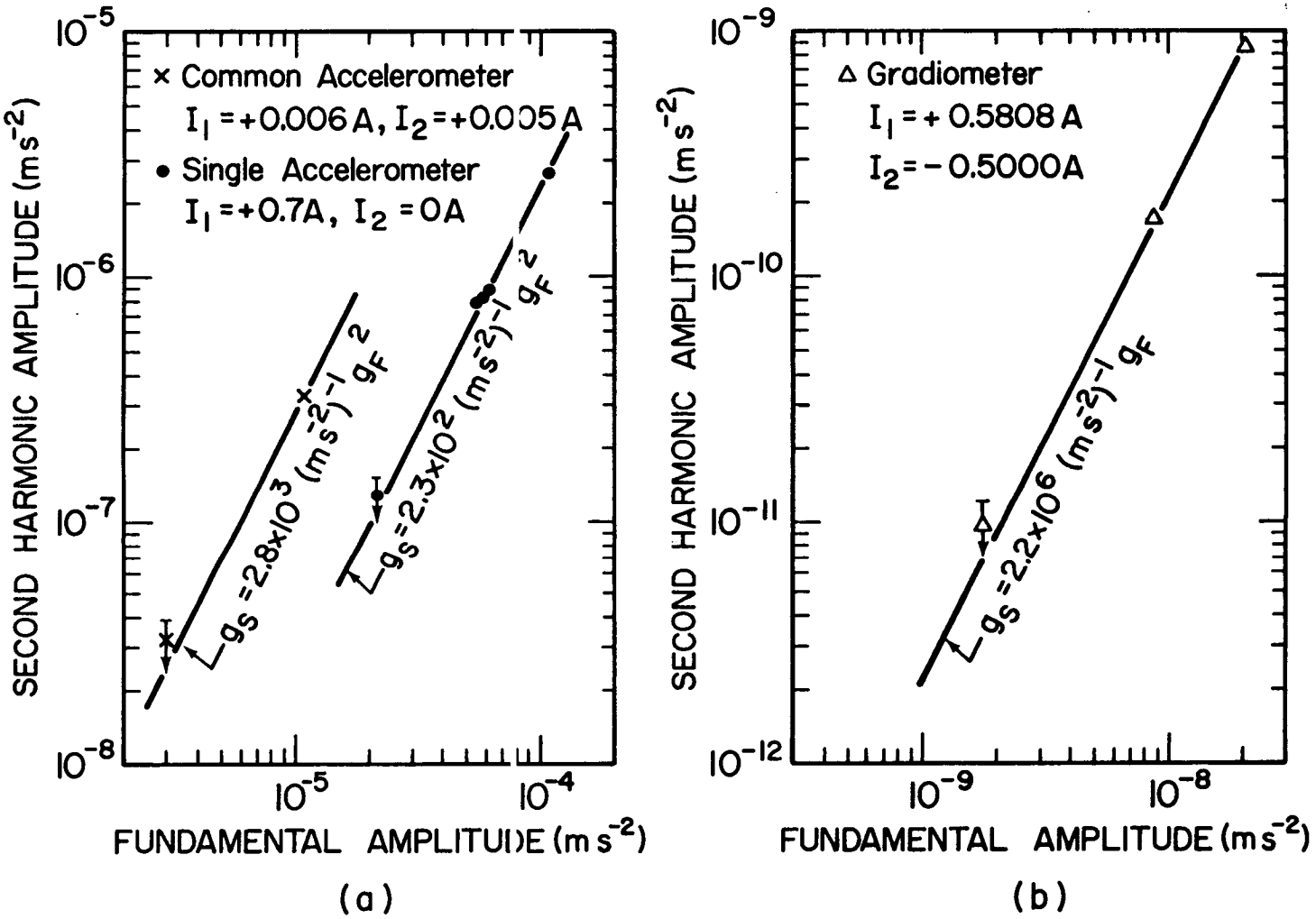

Fig. B2. Second harmonic generation by the centrifugal acceleration in (a) accelerometer modes and (b) the gradiometer mode.

Notice that all three of these values agree with the corresponding theoretical values within a factor of 2.

This excellent agreement gives us confidence that the observed second harmonics are indeed the centrifugal acceleration of the platform. Since only one parameter, $|\delta\hat{n}_{+\hat{\ell}}|$, is relatively unknown in Eq. (B62), one can use this equation and the measured value of $|h_N(2f_p)|$ for the gradiometer to obtain a more reliable value of the misalignment:

$$|\delta\hat{n}_{+\hat{\ell}}| = 6 \times 10^{-4}. \tag{B66}$$

This represents a better measurement of $|\delta\hat{n}_{+\hat{\ell}}|$ than the estimate 7×10^{-4} obtained from the observed wideband noise spectra in Section VC.

We now compute the low frequency noise of the gradiometer which is generated by the centrifugal acceleration. The formalism developed in Section B2 of this Appendix can be directly applied to the nonlinear equation:

$$\delta g_{d,\vec{C}}(t) = \ell[1 - (\hat{n} \cdot \hat{\Omega})^2]\, \Omega_p^2(t). \tag{B67}$$

Substituting $\ell[1 - (\hat{n} \cdot \hat{\Omega})^2]\, \delta(t - t')$ into $h_N(t - t')$ and $\Omega_p(t)$ into $g(t)$, one finds the power spectral density of the centrifugal acceleration error:

$$S_{\Gamma,\vec{C}}(t) = [1 - (\hat{n} \cdot \hat{\Omega})^2]\, \frac{2}{\pi\tau^2}\, \frac{1}{f^3} \left[\int_o^\infty S_{\vec{\Omega}}(f')\, df'\right]^2, \tag{B68}$$

where $S_{\vec{\Omega}}(f')$ is the power spectral density of $\vec{\Omega}_p(t)$.

For the gradiometer under pendulum suspension, Eq. (A6b) leads to

$$\int_o^\infty S_{\vec{\Omega}}(f')\, df' = \frac{\tau_p}{2\pi\ell_p^2} \int_o^\infty d\omega\, \frac{\tau_p^{-1}\, \omega^2}{(\omega_p^2 - \omega^2)^2 + \tau_p^{-2}\, \omega^2}\, S_{\vec{A}}\left(\frac{\omega}{2\pi}\right), \tag{B69}$$

where $S_{\vec{A}}(f)$ is the power spectral density of the horizontal acceleration $\vec{A}_h(t)$ of the pivot point. Thus, the pendulum acts as a narrowband filter centered at f_p so that $S_{\vec{A}}(\omega/2\pi)$ can be evaluated at f_p and taken out of the integral. The integral then has the well-known value $\pi/2$ so that

$$\int_0^\infty S_{\vec{\Omega}}(f')\, df' = \frac{\tau_p}{4\ell_p^2} S_{\vec{A}}(f_p). \tag{B70}$$

Substituting this and $\hat{n} \cdot \hat{\Omega} = 0$ into Eq. (B68), we obtain

$$S_{\Gamma,\vec{C}}(f) = \frac{1}{8\pi} \left(\frac{\tau_p}{\tau}\right)^2 \frac{1}{f^3} \left[\frac{1}{\ell_p^2} S_{\vec{A}}(f_p)\right]^2. \tag{B71}$$

When the experimental values $\tau_p = 150$ s, $\tau = 125$ s, $\ell_p = 2.4$ m, and $S_{\vec{A}}(f_p) = 7 \times 10^{-13}\ \mathrm{m^2\ s^{-4}\ Hz^{-1}}$ are substituted, this yields

$$[S_{\Gamma,\vec{C}}(f)]^{1/2} = 2 \times 10^{-4}\ \mathrm{E\ Hz^{-1/2}} \left(\frac{0.1\ \mathrm{Hz}}{f}\right)^{3/2}. \tag{B72}$$

The derivation of this spectrum does not involve a detailed model for the apparent nonlinearity coefficient $|h_N(f)|$. Neither does it depend on the estimate of integrated acceleration noise such as Eq. (B52), since the high frequency part of $S_{\vec{A}}(f)$ is cut off sufficiently fast by the pendulum. Therefore, the resulting formula (B72) must give a reliable estimate of the low frequency noise generated by the centrifugal acceleration.

REFERENCES

1. P. Vanicek and E.J. Krakiwsky, Geodesy: The Concepts (North-Holland, Amsterdam, 1982), p. 530.

2. T.P. Yunck, W.G. Melbourne and C.L. Thornton, IEEE Trans. Geoscience and Remote Sensing, GE-23, 450 (1985).

3. C.W. Misner, K.S. Thorne and J.A. Wheeler, Gravitation (Freedman, San Francisco, 1973), Chapter 16.

4. For a recent survey of the gravity gradiometer instrument development, see S.K. Jordan, in Proceedings of the Third International Symposium on Inertial Technology for Surveying and Geodesy, edited by K.P. Schwarz (University of Calgary Press, Canada, 1986), Vol. 2, p. 639.

5. H.A. Chan, M.V. Moody and H.J. Paik, Phys. Rev. Lett. 49, 1745 (1982).

6. H.A. Chan, M.V. Moody, H.J. Paik and J.W. Parke, in Proceedings of the 17th International Conference on Low Temperature Physics, edited by U. Eckern et al (North-Holland, Amsterdam, 1984), Vol. 2, p. 927.

7. H.A. Chan, Ph.D. thesis, University of Maryland, College Park, Maryland (1982), unpublished.

8. E.R. Mapoles, Ph.D. thesis, Stanford University, Stanford, California (1981), unpublished.

9. H.J. Paik, Ph.D. thesis and HEPL Report No. 743, Stanford University, Stanford, California (1974), unpublished.

10. K.Y. Wang, Ph.D. thesis, Stanford University, Stanford, California (1979), unpublished.

11. D.G. Blair, H.J. Paik and R.C. Taber, Rev. Sci. Instrum. 46, 8 (1975).

12. H.J. Paik, J. Astronaut. Sci. 29, 1 (1981).

13. J.W. Parke, H.J. Paik, E.R. Mapoles, W.M. Fairbank and D. DeBra, paper in preparation.

14. E.H. Metzger, in Proceedings of AIAA Guidance and Control Specialist Conference (Hollywood, Florida, 1977).

15. H.A. Chan, H.J. Paik, M.V. Moody and J.W. Parke, IEEE Trans. Magnetics, MAG-21, 411 (1985).

16. M.V. Moody, H.A. Chan and H.J. Paik, submitted to J. Appl. Phys.

17. H.A. Chan and H.J. Paik, in Precision Measurements and Fundamental Constants II, edited by B.N. Taylor and W.D. Phillips (NBS Spec. Pub. 617, 1984), p. 601.

18. H.J. Paik, IEEE Trans. Geoscience and Remote Sensing, GE-23, 524 (1985).

19. R.L. Forward, in Proceedings of AIAA Unmanned Spacecraft Meeting (Los Angles, California, 1965), p. 346.

20. M. Schwartz, Information, Transmission, Modulation, and Noise (McGraw-Hill, New York, 1980), p. 348.

21. M.V. Moody, H.A. Chan, H.J. Paik, and C. Stephens, in Proceedings of 17th International Conference on Low Temperature Physics, edited by U. Eckern et al (North-Holland, Amsterdam, 1984), Vol. 1, p. 407.

22. S.O. Rice, in Selected Papers on Noise and Stochastic Processes, edited by N. Wax (Dover, New York, 1954), pp. 264 and 293.

23. J.S. Bendat and A.G. Piersol, Random Data: Analysis and Measurement Procedures (Wiley, New York, 1971), pp. 74, 81, and 320.

24. D. Sonnabend, Engineering Memo 314-388, Jet Propulsion Laboratory, Pasadena, California (1986), unpublished.

PART 3

DESIGN OF AN ADVANCED THREE-AXIS SUPERCONDUCTING GRAVITY GRADIOMETER

A SUPERCONDUCTING GRAVITY GRADIOMETER FOR SPACE AND TERRESTRIAL APPLICATIONS

M.V. Moody, H.A. Chan and H.J. Paik
Department of Physics and Astronomy,
University of Maryland, College Park, MD 20742

A three-axis superconducting gravity gradiometer with a potential sensitivity better than 10^{-3} $\ddot{E}$otvos $Hz^{-1/2}$ is currently under development for applications in space. Though such a high sensitivity may be needed for only a limited number of terrestrial applications, superconductivity offers many extraordinary effects which can be used to obtain a gravity gradiometer with other characteristics necessary for operation in a hostile moving-base environment. Utilizing a number of recently devised techniques which rely on certain properties of superconductors, we have produced a design for a sensitive yet rugged gravity gradiometer with a high degree of stability and a common mode rejection ratio greater than 10^9. With a baseline of 0.11 m, a sensitivity of 0.1 $\ddot{E}$otvos $Hz^{-1/2}$ is expected in an environment monitored to a level of 10^{-2} m s^{-2} $Hz^{-1/2}$ for linear vibration and 7×10^{-6} rad s^{-1} $Hz^{-1/2}$ for angular vibration. A conventional stabilitized platform can be used at this level. The intrinsic noise level, which is two orders of magnitude lower, could be achieved by monitoring the attitude with a superconducting angular accelerometer which is under development. In addition, the new gradiometer design has the versatility of adapting the instrument to different gravity biases by adjusting stored dc currents.

I. INTRODUCTION

The Equivalence Principle of Einstein makes it impossible, even in principle, to separate gravity and acceleration by a local measurement. However, by making a differential measurement over a baseline, one can cancel out acceleration and detect gravity without being confused by platform motion. Although torsion balances have been used to detect gravitational force gradients for over two centuries, only in the most recent two decades have we seen serious efforts to develop moving-base gravity gradiometers.[1,2,3] Research on superconducting gravity gradiometers started more recently as an outgrowth of the superconducting transducer work for low temperature gravitational wave detectors.[4]

In a superconducting instrument, the inconvenience of cryogenic operation is offset by the opportunity of utilizing many exotic properties of superconductors to improve the sensitivity and stability of gravity sensors. In addition to the obvious reduction of the thermal noise of the instrument, the quantization of magnetic flux can be used to obtain "perfectly" stable means of signal transduction, scale factor matching, and proof mass levitation. The availability of SQUIDs (Superconducting QUantum Interference Devices) at liquid helium temperatures is another important factor that makes the superconducting device attractive. SQUIDs are highly sensitive flux measuring devices which are based on the concepts of Josephson tunneling and fluxoid quantization in superconducting loops.[5] The commercial SQUIDs we employ are coupled to input coils for measuring small currents. The sensitivity of these instruments is 1.5×10^{-12} A $Hz^{-1/2}$ and the dynamic range is 10^8.

A three-axis superconducting gravity gradiometer with a potential sensitivity better than 10^{-3} E $Hz^{-1/2}$ (1 E $\equiv$ 1 Eötvös $\equiv 10^{-9}$ s^{-2}) is currently under development at the University of Maryland.[6] This instrument has been

designed primarily for applications in space. However, a sensitive gravity gradiometer would also have a number of terrestrial applications if a satisfactory method of rejecting the high levels of environmental noise can be found. This paper describes a design for a superconducting gravity gradiometer which incorporates several new features to help deal with the problems of a dynamically noisy environment. This design maintains a high sensitivity along with the convenience of a short base line. A versatile magnetic levitation is applied to the proof masses so that the same hardware can be operated in any gravity environment from 0 g_E to 1 g_E (g_E is the earth's gravitational acceleration) by adjusting persistent currents in a number of superconducting coils.

Although the analysis in this paper will be confined to an in-line (i.e. a gradiometer which is sensitive to the diagonal components of the gravity gradient tensor, Γ_{ii}) component gradiometer, it can be extended to a cross-component gradiometer (i.e. one which is sensitive to an off-diagonal component of the gravity gradient tensor, Γ_{ij}, $j \neq i$).

II. PRINCIPLE OF OPERATION

An in-line component superconducting gravity gradiometer consists of a pair of spring-mass accelerometers coupled together by a superconducting circuit to measure differential acceleration.[7] Each accelerometer consist of a superconducting proof mass confined to move along a single axis and a spiral superconducting sensing coil located near the surface of the proof mass (see Fig. 1). An acceleration will cause a displacement of the proof mass which, because of the Meissner effect, will modulate the inductance of the coil at frequencies down to dc. The sensing coil is connected to the input coil of a SQUID amplifier forming a closed superconducting loop. Since the flux in this

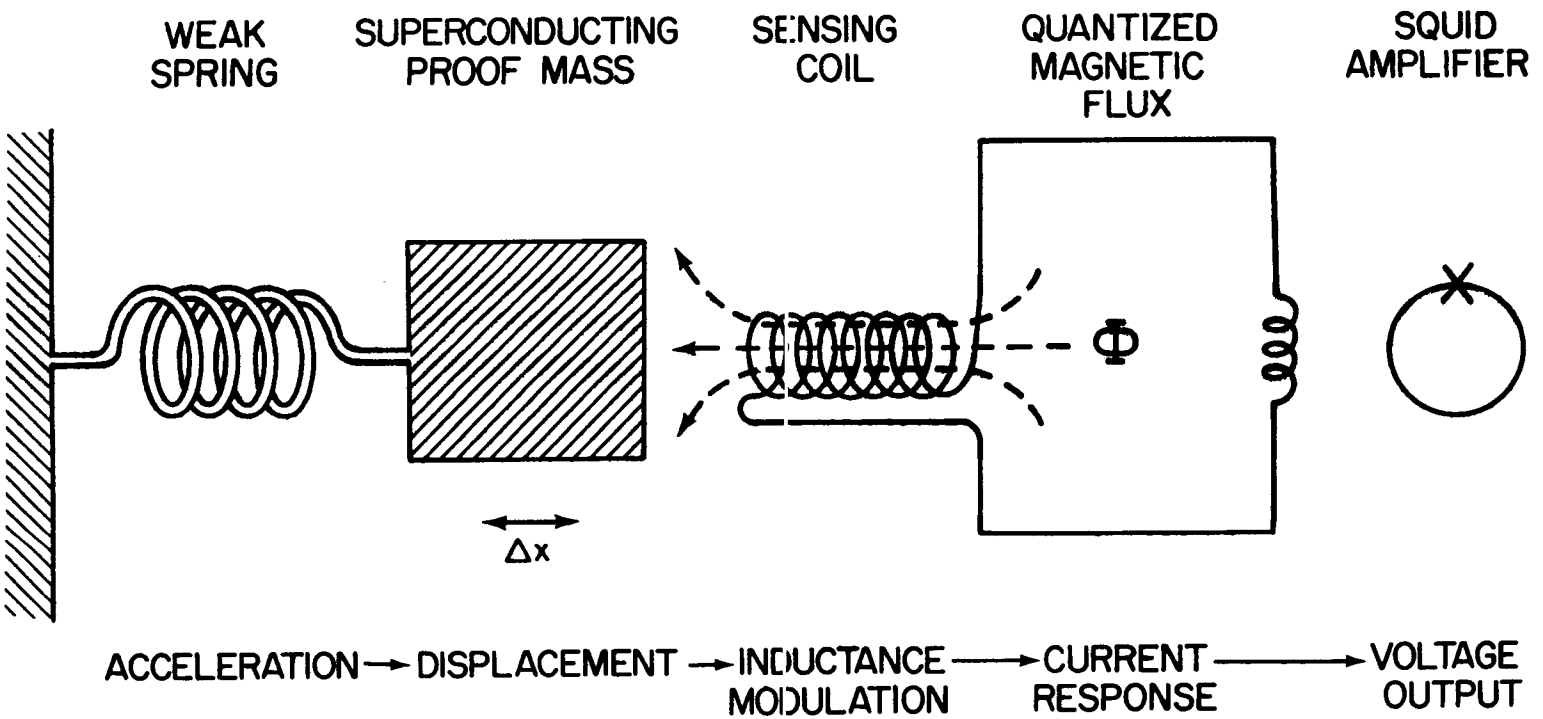

Fig. 1. Schematic diagram of a superconducting accelerometer.

loop must remain constant, the change in the inductance of the sensing coil results in a current change through the SQUID input coil. In this manner very small accelerations can be detected.

In the present design, each proof mass is confined to move along a single axis by a pair of low-loss cantilever spring systems. In practice, the dynamic axes of the proof masses cannot be perfectly aligned and this misalignment can cause various error signals to couple to the gradiometer output. These effects will be discussed in Section VI. As in any two-mass system with only one degree of freedom, the motions of the proof masses can be decomposed into a common mode (i.e. the displacements of the proof masses are in the same direction) and a differential mode (i.e. the displacements are in opposite directions). By coupling the two proof masses together by persistent currents I_{d1} and I_{d2}, flowing in the closed superconducting loops shown by the solid lines in Fig. 2, and adjusting the ratio of I_{d1} to I_{d2}, the sensitivity of the system to common-mode accelerations can be balanced out. By using a similar design, a balance of 2 parts in 10^5 has been demonstrated.[8] Though this degree of balance should be sufficient in a low noise space environment, a higher degree of rejection to common-mode noise is necessary for terrestrial applications and ground tests of the instrument.

By incorporating additional superconducting coils, shown by the dotted lines in Fig. 2, into the circuitry, the frequency of the common-mode resonance can be increased and the resonance peak passively damped without affecting the differential-mode resonance. This effect may be understood by noting that the flux in each of these loops, must remain constant. The electromagnetic energy in these two loops is given by,

$$E = \frac{\Phi_{c1}^2}{2(L_1 + L_2)} + \frac{\Phi_{c2}^2}{2(L_3 + L_4)} , \qquad (1)$$

C-3

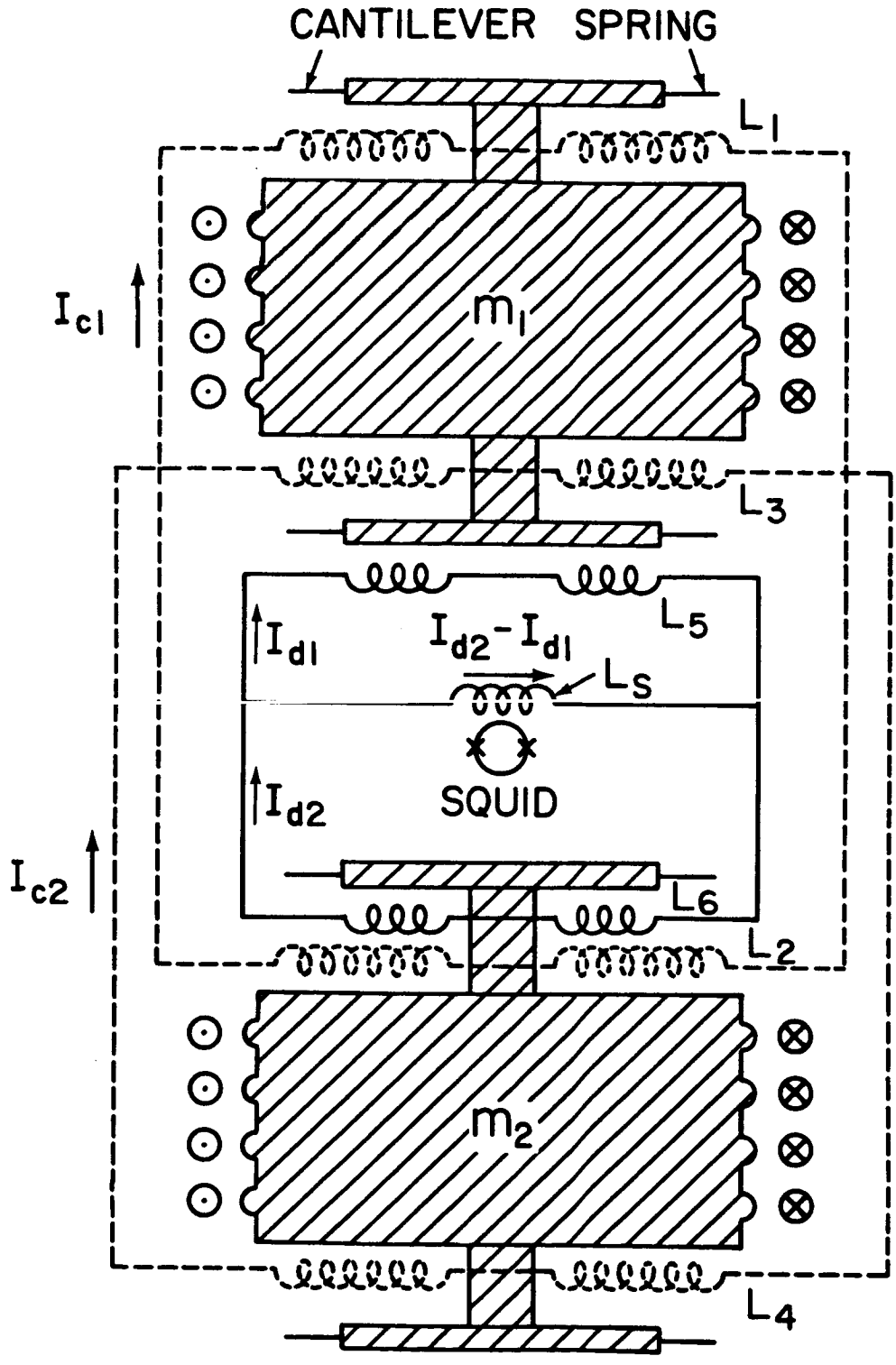

Fig. 2. Circuitry for a superconducting gravity gradiometer.

where Φ_{c1} and Φ_{c2} are the trapped fluxes. In a zero-g environment, $\Phi_{c1} \cong \Phi_{c2}$ is chosen. In the earth's gravity environment, one of these fluxes can be greater than the other. When the gradiometer experiences a common-mode acceleration, the two inductances in each loop change in a like manner resulting in a change in E. However, during a differential acceleration, the changes in the two inductances cancel and E remains constant. Increasing the common-mode frequency decreases the sensitivity of the gradiometer to common-mode accelerations while making isolation of the common-mode resonance peak from environmental noise a simpler task. This isolation, along with the passive damping, limits the amplitude of the signal produced by the common-mode peak at the input of the SQUID amplifier and allows greater dynamic range.

The upward shifting of the common-mode spring constant not only increases the rejection to common-mode accelerations, but it also increases the linearity of the gradiometer by confining the motions of the proof masses. Though the springs are designed for a high degree of linearity, the spring constant still contains higher order terms which may become significant for large displacements.

A conventional approach to the linearity and dynamic range problem of an inertial instrument is to use an active feedback network which senses and cancels the response of the proof mass. One disadvantage of this approach is the possible introduction of a significant noise source from the feedback signal. Since the circuit discussed above is passive and superconducting, there are no additional noise sources to increase the fundamental noise level of the gradiometer. If necessary, active "force rebalance" feedback can of course be applied to both common and differential modes in addition to the simple passive circuitry.

III. DYNAMICS OF THE INSTRUMENT

The inductance of a spiral coil located at a distance d from a superconducting plane is given by

$$L = \mu_o n^2 A\, d, \tag{2}$$

where n is the turns density and A is the area of the coil. With damping ignored, the equations of motion for two proof masses, m_1 and m_2, coupled by the superconducting circuits of Fig. 2 are

$$\ddot{x}_1(t) + \omega_{10}^2[x_1(t) + x_{10}] - \frac{1}{2m_1}\left[\frac{L_{10}}{d_1} I_{c1}^2(t) - \frac{L_{30}}{d_3} I_{c2}^2(t) + \frac{L_{50}}{d_5} I_{d1}^2(t)\right] = g_1(t), \tag{3a}$$

$$\ddot{x}_2(t) + \omega_{20}^2[x_2(t) + x_{20}] - \frac{1}{2m_2}\left[\frac{\bar{L}_{20}}{d_2} I_{c1}^2(t) - \frac{\bar{L}_{40}}{d_4} I_{c2}^2(t) + \frac{\bar{L}_{60}}{d_6} I_{d2}^2(t)\right] = g_2(t), \tag{3b}$$

where ω_{10} and ω_{20} are the uncoupled (angular) resonance frequencies of the proof masses and x_{10} and x_{20} are their equilibrium positions. The driving specific forces for the two proof masses are denoted by $g_1(t)$ and $g_2(t)$. Also, d_i is the equilibrium spacing between the i-th coil and the proof mass, and $L_{i0} = \mu_o n^2 A_i d_i$.

The requirement that the flux in a closed superconducting loop must remain constant imposes four constraints:

$$\{L_{10}[1 + x_1(t)/d_1] + L_{20}[1 + x_2(t)/d_2]\}\, I_{c1}(t) = \Phi_{c1}, \tag{4a}$$

$$\{L_{30}[1 - x_1(t)/d_3] + L_{40}[1 - x_2(t)/d_4]\}\, I_{c2}(t) = \Phi_{c2}, \tag{4b}$$

$$\{L_{50}[1 + x_1(t)/d_5] + L_S\}\ I_{d1} - L_S\ I_{d2} = \Phi_{d1}, \tag{4c}$$

$$\{L_{60}[1 + x_2(t)/d_6] + L_S\}\ I_{d2} - L_S\ I_{d1} = \Phi d_2. \tag{4d}$$

The constraint equations give, to the first order in x/d,

$$I_{c1} = I_{c10}\left(1 - \frac{L_{10}\ x_1/d_1 + L_{20}\ x_2/d_2}{L_{10} + L_{20}}\right), \tag{5a}$$

$$I_{c2} = I_{c20}\left(1 - \frac{L_{30}\ x_1/d_1 + L_{40}\ x_2/d_4}{L_{30} + L_{40}}\right), \tag{5b}$$

$$I_{d1} = I_{d10}\left[1 - \frac{L_{50}(L_{60} + L_S)\ x_1/d_5 + (I_{d20}/I_{d10})\ L_{60}L_S x_2/d_6}{(L_{50} + L_S)\ (L_{60} + L_S) - L_S^2}\right], \tag{5c}$$

$$I_{d2} = I_{d20}\left[1 - \frac{L_{60}(L_{50} + L_S)\ x_2/d_6 + (I_{d10}/I_{d20})\ L_{50}L_S x_1/d_5}{(L_{50} + L_S)\ (L_{60} + L_S) - L_S^2}\right]. \tag{5d}$$

Upon substitution of these results into the equations of motion, one finds

$$\ddot{x}_1 + \frac{1}{m_1}\left[K_{10} + K_1 + K_3 + K_5\left(1 + \frac{L_{60}}{L_S}\right)\right] x_1$$

$$+ \frac{1}{m_1}\left[(K_1K_2)^{1/2} + (K_3K_4)^{1/2} + (K_5K_6)^{1/2}\right] x_2$$

$$+ \frac{K_{10}}{m_1} x_{10} - \frac{1}{2m_1}\left[\frac{L_{10}}{d_1} I_{c10}^2 - \frac{L_{30}}{d_3} I_{c20}^2 + \frac{L_{50}}{d_5} I_{d10}^2\right] = g_1, \tag{6a}$$

$$\ddot{x}_2 + \frac{1}{m_2}\left[K_{20} + K_2 + K_4 + K_6\left(1 + \frac{L_{50}}{L_S}\right)\right] x_2$$

$$+ \frac{1}{m_2}\left[(K_1K_2)^{1/2} + (K_3K_4)^{1/2} + (K_5K_6)^{1/2}\right] x_1$$

$$+ \frac{K_{20}}{m_2} x_{20} - \frac{1}{2m_2} \left[\frac{L_{20}}{d_2} I_{c10}^2 - \frac{L_{40}}{d_4} I_{c20}^2 + \frac{L_{60}}{d_6} I_{d20}^2\right] = g_2, \qquad (6b)$$

where

$$K_1 \equiv \frac{I_{c10}^2 L_{10}^2}{d_1^2(L_{10} + L_{20})}, \quad K_2 \equiv \frac{I_{c10}^2 L_{20}^2}{d_2^2(L_{10} + L_{20})}, \qquad (7a,b)$$

$$K_3 \equiv \frac{I_{c20}^2 L_{30}^2}{d_3^2(L_{30} + L_{40})}, \quad K_4 \equiv \frac{I_{c20}^2 L_{40}^2}{d_4^2(L_{30} + L_{40})}, \qquad (7c,d)$$

$$K_5 \equiv \frac{I_{d50}^2 L_{50}^2}{d_5^2(L_{50}L_{60}/L_S + L_{50} + L_{60})}, \quad K_6 \equiv \frac{I_{d60}^2 L_{60}^2}{d_6^2(L_{50}L_{60}/L_S + L_{50} + L_{60})}. \qquad (7e,f)$$

Equations (6a) and (6b) can be rewritten in a simpler form:

$$\ddot{x}_1 + \frac{\nu_1}{m_1} x_1 + \frac{\nu_3}{m_1} x_2 + \omega_{10}^2 x_{10} - c_1 = g_1, \qquad (8a)$$

$$\ddot{x}_2 + \frac{\nu_2}{m_2} x_2 + \frac{\nu_3}{m_2} x_1 + \omega_{20}^2 x_{20} - c_2 = g_2, \qquad (8b)$$

by defining

$$\nu_1 \equiv K_{10} + K_1 + K_3 + K_5 (1 + L_{60}/L_S), \qquad (9a)$$

$$\nu_2 \equiv K_{20} + K_2 + K_4 + K_6 (1 + L_{50}/L_S), \qquad (9b)$$

$$\nu_3 \equiv (K_1K_2)^{1/2} + (K_3K_4)^{1/2} + (K_5K_6)^{1/2}, \qquad (9c)$$

and

$$c_1 \equiv \frac{1}{2m_1} \left(\frac{L_{10}}{d_1} I_{c10}^2 - \frac{L_{30}}{d_3} I_{c20}^2 + \frac{L_{50}}{d_5} I_{d10}^2\right), \qquad (10a)$$

$$c_2 \equiv \frac{1}{2m_2}\left(\frac{L_{20}}{d_2} I_{c10}^2 - \frac{L_{40}}{d_4} I_{c20}^2 + \frac{L_{60}}{d_6} I_{d20}^2\right) . \tag{10b}$$

Thus the equilibrium positions are given by

$$x_{10} = (c_1 + g_{10})/\omega_{10}^2 , \tag{11a}$$

$$x_{20} = (c_2 + g_{20})/\omega_{20}^2 , \tag{11b}$$

where g_{10} and g_{20} are constant bias forces. The solutions to Eqs. (8a) and (8b) are of the form:

$$x_1 = Ae^{i\omega t} \quad , \quad x_2 = Be^{i\omega t}. \tag{12}$$

Making these substitutions gives

$$\omega_{1,2}^2 = \frac{1}{2}\left\{\frac{\nu_1}{m_1} + \frac{\nu_2}{m_2} \pm \left[\left(\frac{\nu_1}{m_1} - \frac{\nu_2}{m_2}\right)^2 + \frac{4\nu_3^2}{m_1 m_2}\right]^{1/2}\right\} , \tag{13}$$

where the general solutions are

$$x_1 = A_1 e^{i\omega_1 t} + A_{-1} e^{-i\omega_1 t} + A_2 e^{i\omega_2 t} + A_{-2} e^{-i\omega_2 t}, \tag{14a}$$

$$x_2 = B_1 e^{i\omega_1 t} + B_{-1} e^{-i\omega_1 t} + B_2 e^{i\omega_2 t} + B_{-2} e^{-i\omega_2 t}. \tag{14b}$$

As we will show later, if ω_{10} and ω_{20} are small, the amplifier noise is negligible and the coupling to the amplifier can be reduced. In this case I_{d1} and I_{d2} are small and the terms involving K_5 and K_6 can be neglected. By combining Eq. (13) with Eq. (6a) or (6b), one can show that the eigenvalues

approach $x_1 + x_2$ and $x_2 - x_1$ only if

$$\frac{K_1}{m_1} \approx \frac{K_2}{m_2} \quad , \quad \frac{K_3}{m_1} \approx \frac{K_4}{m_2} \quad \text{and} \quad \omega_{10} \approx \omega_{20}. \tag{15}$$

Thus in order for the coupled resonance frequencies to correspond to the true differential and common modes, the coil geometries of L_1 and L_2, and L_3 and L_4 as well as the masses and the uncoupled resonance frequencies must be matched. Under these conditions, the differential-mode resonance frequency is given by

$$\omega_{od}^2 = \frac{1}{2} (\omega_{10}^2 + \omega_{20}^2), \tag{16}$$

and the common-mode resonance frequency is

$$\omega_{oc}^2 = \omega_{od}^2 + \frac{2}{m_1} (K_1 + K_3). \tag{17}$$

The eigenvalues are then

$$X_d \equiv x_2 - x_1 = 2(A_d e^{i\omega_{od}t} + A_{-d} e^{-i\omega_{od}t}), \tag{18a}$$

$$X_c \equiv \frac{1}{2} (x_1 + x_2) = 2(A_c e^{i\omega_{oc}t} + A_{-c} e^{-i\omega_{oc}t}). \tag{18b}$$

The equations of motion can now be rewritten in the form of two simple harmonic oscillators:

$$\ddot{X}_d + \omega_{od}^2 (X_d - X_{do}) = g_d, \tag{19a}$$

$$\ddot{X}_c + \omega_{oc}^2 (X_c - X_{co}) = g_c, \tag{19b}$$

where

$$g_d(t) \equiv g_2(t) - g_1(t), \tag{20a}$$

$$g_c(t) \equiv \frac{1}{2}\,[g_1(t) + g_2(t)]. \tag{20b}$$

Since the displacement of a driven harmonic oscillator at frequencies below the resonance frequency is inversely proportional to the square of the resonance frequency, the sensitivity to common-mode acceleration is reduced by a factor of $\omega_{oc}^2/\omega_{od}^2$.

The signal through the input coil of the SQUID is, from Eqs. (5c) and (5d),

$$I_{d2} - I_{d1} = I_{d20} - I_{d10} + \left[\left(\frac{I_{d20}}{d_6} - \frac{I_{d10}}{d_5}\right) X_d - 2\left(\frac{I_{d10}}{d_5} + \frac{I_{d20}}{d_6}\right)X_c\right]\left[1 + L_S\left(\frac{1}{L_{50}} + \frac{1}{L_{60}}\right)\right]^{-1}. \tag{21}$$

Thus the sensitivity to common-mode excitations may be further reduced by matching I_{d20}/d_6 and $-I_{d10}/d_5$. In fact, in this simple model, perfect common-mode rejection may be obtained in principle by adjusting I_{d20} and I_{d10}; however, experimentally it is often easier to match several sets of parameters to moderate accuracy than to match one set to very high accuracy.

IV. SUPERCONDUCING NEGATIVE SPRING

A description of the superconducting negative spring has been presented in a previous paper[9]. That paper, however, gave only a numerical solution. In this section, after a discussion of its application to the gradiometer, we

present an analytical solution which allows the data to be more easily related to other geometries.

The noise power spectral density of the gradiometer can be expressed[10] as

$$S_\Gamma(f) = \frac{8}{m\ell^2}\left[2\pi f\, k_B T\, R(f) + \frac{\omega_{od}^2}{2\beta\eta}\, E_A(f)\right], \qquad (22)$$

where m, ℓ, $E_A(f)$, and $\beta\eta$ are, respectively, the mass of each proof mass, the baseline, the amplifier noise energy (called the "input energy resolution"), and the energy coupling factor for the amplifier. The function R(f) is a frequency-dependent damping factor, which becomes equal to the inverse of the quality factor at the resonance frequency $f = \omega_{od}/2\pi$. The first term on the right hand side of Eq. (22) is due to the Brownian motion noise and the second term on the right is due to the noise of the amplifier. This version of the sensitivity equation is different from the version which appeared in Ref. 10. In its present form, the equation has been modified to include the fact that the magnitude of the force fluctuations at the signal frequency f is, in general, different from that at the resonance frequency. Namely, the Brownian motion noise has a frequency dependence which is governed by the nature of the loss mechanism in the spring.

The superconducting gravity gradiometer at present has its fundamental noise limited by the amplifier noise rather than the Brownian motion noise.[8] Equation (22) indicates that one of the most obvious ways to increase the resolution of the gradiometer is to lower its resonance frequency ω_{od}. Lowering the mechanical spring constant while maintaining rigidity along the nonsensitive axes is a difficult task. One method of overcoming this dilemma for a superconducting gradiometer has been previously demonstrated.[9] This method uses a superconducting negative spring to counteract the positive

mechanical spring. Each negative spring consists of a disk with a semi-circular edge located in a solenoid with a length less than the thickness of the disk. The proof mass is shaped to contain several of these "disks" (see Fig. 2). The negative spring constant can be adjusted by changing the persistent current I_n in the solenoid. The lower limit for the resonance frequency will be determined by a number of factors. These factors include the required bandwidth of the gradiometer, the 1/f noise of the SQUID amplifier, and the magnitude of the higher order terms in the spring constant.

When two large spring constants are balanced to obtain a low frequency spring, the stability and linearity requirements for each of these springs can become much more important. In the present design, the stability of the spring constants is maintained by a number of beneficial features which are available at liquid helium temperatures. These features include the stability of materials, the stability of persistent currents in superconducting loops, and the stable temperature environment. The linearity requirement is substantially decreased by the common-mode rejection coils which confine the motions of the proof masses. Also, if necessary, the stability and linearity of the system can be further enhanced by standard feedback techniques.

To estimate the negative spring constant (see Fig. 3), we approximate that the field between the solenoid and the superconducting surface is constant for a given displacement. Then, the change in the magnetic field energy with displacement is due to a change in the effective volume of the solenoid. The volume as a function of displacement x is

$$V(x) = \frac{1}{2}\pi D\ [L(d_o + R) - R^2\theta] = V_o - \frac{1}{2}\pi DR^2\theta, \qquad (23)$$

where

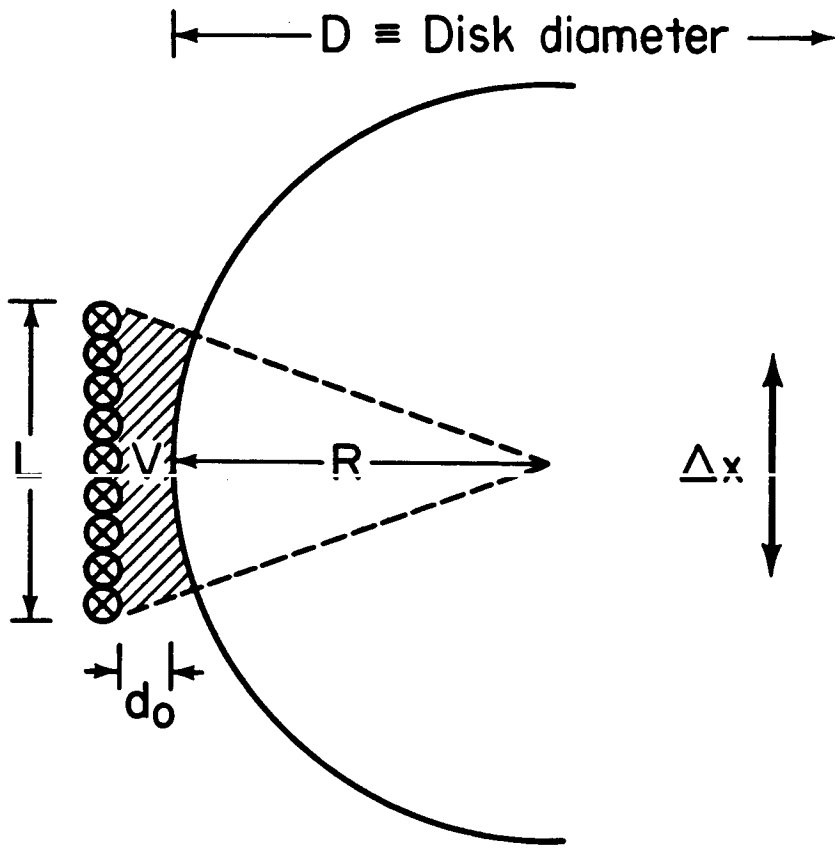

Fig. 3. Diagram for negative spring calculation showing the edge of a disk and a section of a solenoid.

$$\theta = \tan^{-1}\left(\frac{L/2 + x}{d_o + R}\right) + \tan^{-1}\left(\frac{L/2 - x}{d_o + R}\right). \tag{24}$$

Here, D, L, R and d_o are defined in Fig. 3. The magnetic potential energy is

$$E(x) = \frac{\Phi_o^2}{2L} = \frac{\Phi_o^2}{2\mu_o n^2 V(x)} . \tag{25}$$

Expanding E(x) in powers of x gives

$$E(x) = \frac{1}{2}\mu_o n^2 I_n^2 (V_o - c_1 x^2 + c_2 x^4 + \cdots), \tag{26}$$

where

$$c_1 = \frac{\pi D R^2 L}{2(R + d_o)^3 \left[1 + (L/2)^2/(R + d_o)^2\right]^2} . \tag{27}$$

Dropping the higher order terms and differentiating twice with respect to x leads to the spring contant:

$$k_n = \frac{\partial^2 E}{\partial x^2} = -\mu_o n^2 I_n^2 c_1 . \tag{28}$$

For the geometry in the aforementioned demonstration, this expression gives $k_n = -1100\ N\ m^{-1}$, which is in good agreement with the experimental value of $-1180\ N\ m^{-1}$.

V. A PRACTICAL DESIGN

If the effect of the resonance frequency is excluded, the determining quantities for the Brownian motion and amplifier noise terms of Eq. (22) are R(f) and $E_A(f)$, respectively. Presently, the most sensitive commercially

available SQUID[11] has an energy resolution of $E_A(f) = 3 \times 10^{-30}$ J $Hz^{-1/2}$ down to 0.1 Hz at which point 1/f noise becomes important. The damping factor of the proof mass motion contains contributions from both the mechanical and electromagnetic spring constants with the latter generally dominating for large coupling between the electrical and mechanical systems. Though difficult to obtain, $R(f) \lesssim 10^{-6}$ has been observed in the superconducting coils of similar design near 1 kHz.[12] For the purpose of our sensitivity calculation, we assume that $R(f) \cong 10^{-6}$ can be achieved at low frequencies ($f \lesssim 1$ Hz).

With the above values in mind, and keeping with the objectives stated in the introduction, we propose the following parameters for a practical design: a differential-mode resonance frequency of 1.6 Hz, a baseline of 0.11 m, and a hollow niobium (Nb) proof mass 0.038 m in diameter by 0.029 m long with a mass of 0.1 kg. This design would give a sensitivity of 2×10^{-3} E $Hz^{-1/2}$. The dimensions can be reduced further if the sensitivity goal is set at a more moderate level of 0.1 E $Hz^{-1/2}$.

For the common-mode rejection (CMR) coils and negative spring coils, the primary limitation is the critical field of the proof mass material. For Stanford grade niobium at 4.2 K, the critical field is 0.12 Wb m^{-2}.[13] A second limitation is the minimum spacing between the superconducting coils and the surface of the proof mass. These coils have been made in the past with niobium wire. With a wire coil, the minimum spacing is about 1×10^{-4} m. One should be able to reduce this value substantially using thin-film coils.

For the CMR coils, the field value at the surface of the proof mass should be kept approximately 10% below the critical field value. This precaution would allow the gradiometer to withstand a common-mode acceleration of up to twice the earth's gravity without the field exceeding the critical value

and trapping flux in the superconductors. In order to maintain the correct spacing between the proof mass and the coils, two CMR circuits (containing persistent currents I_{c10} and I_{c20}, respectively) with one coil on each side of each proof mass are necessary (see Fig. 2). For vertical orientation, $I_{c10}^2 \approx 0.8\ I_{c20}^2$ to compensate for the earth's gravitational field. Then, with $\mu_o n I_{c10} = 0.10$ Wb m^{-2}, $\mu_o n I_{c20} = 0.11$ Wb m^{-2}, $d = 1 \times 10^{-4}$ m and $A = 1.1 \times 10^{-3}$ m^2, and with Eqs. (17) and (7), the common-mode resonance frequency is 230 Hz. With this increased stiffness, Eqs. (19) and (21) imply that a total CMRR (common-mode rejection ratio) of 1×10^9 is achievable, if the gradiometer is balanced to two parts in 10^5.

For the negative spring coils, the field strength can be near the critical value giving $nI_n = 0.9 \times 10^5$ A m^{-1}. The expression in Eq. (27) has a maximum value of 0.27 at $L/(R + d_o) = 2/\sqrt{3}$. If 12 disks with a diameter of 3.8×10^{-2} m are used, one obtains $k_n = -4.3 \times 10^3$ N m^{-1}, which can compensate a mechanical resonance frequency of 33 Hz at 4.2 K. By lowering the temperature to 1.1 K, the critical field will increase by 25% allowing the mechanical resonance and the common-mode frequencies to be increased to 40 Hz and 300 Hz, respectively.

VI. ENVIRONMENTAL NOISE AND INSTRUMENT ERRORS

In order to realize an operational sensitivity of 2×10^{-3} E $Hz^{-1/2}$ with a CMRR of 1×10^9 and a baseline of 0.11 m, a linear acceleration noise level better than 2×10^{-5} g_E $Hz^{-1/2}$ is required. The seismic noise level in a relatively quiet place is less than 10^{-6} g_E $Hz^{-1/2}$; consequently, the passive CMR will be sufficient for a stationary platform. For a moving base application, however, the platform vibration level can be as high as 10^{-3} g_E $Hz^{-1/2}$. With this vibration level, a sensitivity of 0.1 E $Hz^{-1/2}$ would still

be obtainable. This sensitivity would be sufficient for many applications. To extend a moving base system to 10^{-3} E $Hz^{-1/2}$, the platform vibrations would have to be monitored to a level of 10^{-5} g_E $Hz^{-1/2}$ to compensate the common-mode errors of the gradiometer. A vector measurement of the platform acceleration with this resolution could be made by using a triad of conventional accelerometers. Alternatively, in a three-axis gradiometer, an additional SQUID could be coupled to the CMR circuit of each component gradiometer to obtain a simultaneous reading of the three linear acceleration components of the gradiometer.

With the common-mode error removed, the second most important error source is the angular motion of the gradiometer with respect to an inertial frame. Angular motion about an axis other than its own sensitive axis produces error signals even in a perfectly aligned gradiometer through the centrifugal acceleration, which is indistinguishable from an in-line component gravity gradient. In order to suppress this error to a level of 2×10^{-3} E $Hz^{-1/2}$, for a vertical or horizontal orientation, the attitude rate of the gradiometer must be known or controlled to 1.4×10^{-8} rad s^{-1} $Hz^{-1/2}$. For 0.1 E $Hz^{-1/2}$, this value becomes 7×10^{-6} rad s^{-1} $Hz^{-1/2}$. The requirement for the 0.1 E $Hz^{-1/2}$ instrument could be met with conventional gyroscopes mounted to the platform. The measurement of the attitude rate at the level of 10^{-8} rad s^{-1} $Hz^{-1/2}$ may be difficult for a conventional gyroscope. A superconducting "six-axis" accelerometer, which measures three linear and three angular acceleration components simultaneously with high sensitivity is under development[14] and could be used for this purpose.

Up to this point, this paper has dealt with a gravity gradiometer in which the sensitive axes of the component accelerometers are perfectly aligned. In a gradiometer whose sensitive axes are misaligned, linear and

angular motion will generate additional errors in the gradiometer output. Linear motion orthogonal to the direction along which a single-axis gradiometer is balanced would couple directly to the gradiometer output at a level proportional to the degree of misalignment. Angular motion can couple in through axis misalignment in one of two ways. First, in the earth's field, an angular displacement will result in a change in the dc bias level for the two accelerometers. When the two sensitive axes are misaligned with respect to each other, the change in the bias level will be different for the two accelerometers. Second, the misalignment of the average sensitive axis with respect to the baseline will result in a direct coupling of angular acceleration to the gradiometer output. We summarize below the error model associated with these misalignments.

The gradiometer axis alignment errors can be described in terms of a misalignment between the sensitive axes of the component accelerometers:

$$\delta\hat{n}_{-} \equiv \hat{n}_2 - \hat{n}_1 \ , \tag{29}$$

and a misalignment between the average direction of the sensitive axis and the direction of the base line:

$$\delta\hat{n}_{+\hat{\ell}} = \frac{1}{2}\left(\hat{n}_2 + \hat{n}_1\right) - \hat{\ell} \ . \tag{30}$$

In these equations, $\hat{n}_1$ and $\hat{n}_2$ are the unit vectors in the direction of the sensitive axes of the two component accelerometers and $\hat{\ell}$ is the unit vector in the direction of the baseline. In addition to causing a gradiometer orientation error, these alignment errors cause coupling to the gravity gradient output from the common-mode acceleration component along the $\delta\hat{n}_{-}$ direction and

from the angular acceleration component along the $\delta\hat{n}_{\hat{+\ell}} \times \hat{n}$ direction.

In a terrestrial environment, a common-mode acceleration along the $\delta\hat{n}_-$ direction is generated not only by linear motions, but also by angular motions which modulate the earth's gravity field $\vec{g}_E$. The error term along the $\delta\hat{n}_-$ direction is then given by

$$\delta\Gamma_{\hat{n}_-}(f) = \frac{1}{\ell}\,\delta\hat{n}_- \cdot [\vec{g}_E \times \vec{\theta}_n(f) + \vec{a}_n(f)] \,, \tag{31}$$

where $\vec{\theta}_n(f)$ is the angular displacement noise and $\vec{a}_n(f)$ is the linear acceleration noise. The error term along the $\hat{n}_{\hat{+\ell}} \times \hat{n}$ direction is given by

$$\delta\Gamma_{\hat{n}_+}(f) = \delta\hat{n}_{\hat{+\ell}} \times \hat{n} \cdot \vec{\alpha}_n(f) \,, \tag{32}$$

where $\vec{\alpha}_n(f)$ is the angular acceleration noise. A detailed derivation of Eqs. (31) and (32) will be published elsewhere.

Using ordinary machining techniques and taking care to relieve stress in the mechanical components, the alignment errors $\delta\hat{n}_-$ and $\delta\hat{n}_{\hat{+\ell}}$ can be reduced to the level of 10^{-4}. One possible method of improving the mechanical alignment is through the use of piezoelectric crystals. In such a system, a set of three or four piezoelectric crystal stacks would be used to adjust the relative angle of the sensitive axes of the two accelerometers in a single-axis gradiometer. An alignment of one part in 10^8 for both $\delta\hat{n}_-$ and $\delta\hat{n}_{\hat{+\ell}}$ appears feasible by using this method.

A second method for reducing the alignment error $\delta\hat{n}_-$ requires a three-axis gradiometer. In this method, additional superconducting circuits which are sensitive to the common-mode components of the acceleration along two axes are coupled to the proof masses of the third "orthogonal" axis. By adjusting

the persistent currents in these circuits, in a manner similar to the one-dimensional balance discussed in Sections II and III, the residual coupling between common-mode accelerations and the gravity gradient outputs due to axis misalignment is balanced out. Thus a rigorous three-dimensional balance against sensitivity to linear accelerations is obtained. However, the angular acceleration error caused by the misalignment $\delta\hat{n}_{\hat{+\ell}}$ must be compensated for separately.

Equations (31) and (32) determine the requirements for the attitude and attitude acceleration control/knowledge for a gravity gradiometer with a given sensitivity. In order to achieve 2×10^{-3} E $Hz^{-1/2}$, $\theta_n(f)$ and $\alpha_n(f)$ must be controlled or known to 2×10^{-6} rad $Hz^{-1/2}$ and 2×10^{-4} rad s^{-2} $Hz^{-1/2}$, respectively, if $\delta\hat{n}_-$ and $\delta\hat{n}_{\hat{+\ell}}$ can be reduced to the level of 10^{-8}. For 0.1 E $Hz^{-1/2}$, these requirements become 10^{-4} rad $Hz^{-1/2}$ and 10^{-2} rad s^{-2} $Hz^{-1/2}$, respectively. Conventional gyroscopes could be used to satisfy these requirements. If the alignment errors cannot be reduced sufficiently below 10^{-4}, the gradiometer may be integrated with the superconducting six-axis accelerometer, which will have orders of magnitude improvement in attitude resolution over the conventional gyroscopes.

We are also investigating a "pendulum suspension"[10] for the gravity gradiometer. If properly designed, a pendulum suspension can provide isolation in the three angular and two of the three linear degrees of freedom. Since the gradiometer can be balanced in the remaining linear degree of freedom, rejection of acceleration noise in all six degrees of freedom is achieved. Details of the pendulum isolation will be presented in a forthcoming paper.

The extreme sensitivity of the gravity gradiometer requires careful isolation of the device from the thermal and electromagnetic fluctuations of the

environment as well. Below the lamda point (T_c = 2.17 K), the liquid helium provides a stable and a gradient-free thermal environment. Also, the sensitivity of the instrument to temperature drift can be tuned out by employing a method similar to the common-mode acceleration rejection technique discussed in Section II.[6] The superconductor itself is a nearly perfect shield against fluctuating magnetic and electric fields. Thus, the superconducting gravity gradiometer can be isolated very effectively from the thermal and electromagnetic noise, leaving the mechanical noise mechanisms discussed above as the most important error sources.

VII. CONCLUSIONS

The necessity of operating a very sensitive gravity gradiometer in an environment with a large common-mode acceleration background requires extreme stability in the acceleration-to-current transfer functions of component accelerometers and a reliable means of balancing out the common-mode sensitivity. The perfect stability of quantized magnetic flux in superconductors can be used to obtain a very sensitive gravity gradiometer with a high CMRR. Combining experiences obtained with a prototype superconducting gravity gradiometer and new technological innovations, we have produced a design which gives a sensitivity of 2×10^{-3} E $Hz^{-1/2}$ and a CMR in excess of 1×10^{9}. A three-axis in-line component gravity gradiometer, which incorporates many of the features discussed in this paper, is under construction for space applications. This instrument has been designed for a relatively quiet environment and has been scaled up slightly to deliver a sensitivity of 10^{-4} E $Hz^{-1/2}$

The new design utilizes magnetic levitation of the proof masses to null out the gravity bias, permitting operation of the instrument in an arbitrary orientation on the earth and in space. The low temperature environment gives

an opportunity to isolate the instrument from thermal and electromagnetic fluctuations in the survey vehicle. The inherent sensitivity of all gravity gradiometers to angular motion induced errors makes the attitude control of the gradiometer platform a challenge. However, superconducting techniques can again be employed to monitor the linear and angular motions of the platform with sufficiently high sensitivity and stability. The feedback and error compensation techniques which have been developed for conventional inertial navigation systems and gravity gradiometers could be adapted to the cryogenic instruments discussed here.

ACKNOWLEDGEMENTS

We acknowledge a fruitful collaboration with Q. Kong and J.W. Parke on the experimental development of superconducting gravity gradiometers. We have also benefited from discussions with Professor Daniel DeBra.

Supported in part by NASA Contract NAS8-33822 and Army Contract DACA72-84-C-0004.

REFERENCES

1. R.L. Foward, Hughes Research Laboratories, Research Report 469 (1973).

2. E.H. Metzger and D.R. Allen, Bell Aerospace Co. Report 9500-92044 (1972).

3. M.B. Trageser, in Proceedings of the 2nd International Symposium on Inertial Technology for Surveying and Geodesy, edited by K. Schwartz (Canadian Inst. of Surveying, Ottawa, 1981).

4. H.J. Paik, J. Appl. Phys., 47, p. 1168, (1976).

5. B.B. Schwartz and S. Foner (Eds.), Superconducting Applications: SQUIDs and Machines, (Plenim Press, New York, 1977).

6. H.A. Chan, M.V. Moody, H.J. Paik, and J.W. Parke, in Proceedings of Seventeenth International Conference on Low Temperature Physics, edited by U. Eckern, A. Schmid, W. Weber, and H. Wahl (North Holland, New York, 1984), pp. 927-928.

7. H.J. Paik, J. Astronaut. Sci., 29, pp. 1-18 (1981).

8. M.V. Moody, H.A. Chan and H.J. Paik, IEEE Trans. Mag., MAG-19, pp. 461-463, (1983).

9. J.W. Parke, H.J. Paik, H.A. Chan, and M.V. Moody, in Proceedings of Tenth International Cryogenic Engineering Conference, edited by H. Collon, P. Berglund, and M. Krusius (Butterworth, London, 1984).

10. H.A. Chan, Ph.D. thesis, Univeristy of Maryland, College Park, Maryland (1982).

11. Model 440 DC SQUID System, Biomagnetic Technologies, Inc., San Diego, California.

12. P.F. Michelson and R.C. Taber, Phys. Rev. D, 29, pp. 2149-2157 (1984).

13. H.J. Paik, Ph.D. thesis, Stanford University, Stanford, California (1974).

14. H.A. Chan, H.J. Paik, M.V. Moody, and J.W. Parke, IEEE Trans. .Mag., MAG-21, pp. 411-414 (1985).

1. REPORT NO.	2. GOVERNMENT ACCESSION NO.	3. RECIPIENT'S CATALOG NO.
NASA CR-4011		

4. TITLE AND SUBTITLE	5. REPORT DATE
Development of a Sensitive Superconducting Gravity Gradiometer for Geological and Navigational Applications	September 1986
	6. PERFORMING ORGANIZATION CODE
7. AUTHOR(S) H. J. Paik and J-P. Richard	8. PERFORMING ORGANIZATION REPOR
9. PERFORMING ORGANIZATION NAME AND ADDRESS Department of Physics and Astronomy University of Maryland College Park, MD 20742	10. WORK UNIT NO. M-536
	11. CONTRACT OR GRANT NO. NAS8-33822
12. SPONSORING AGENCY NAME AND ADDRESS National Aeronautics and Space Administration Washington, DC 20546	13. TYPE OF REPORT & PERIOD COVER Contractor Report July 80 - July 85
	14. SPONSORING AGENCY CODE RTOP 676-59-33

15. SUPPLEMENTARY NOTES
Final Report
Research Program Technical Monitor
George C. Marshall Space Flight Center

16. ABSTRACT

A sensitive and stable gravity gradiometer would provide high resolution gravity measurements from space. The instrument could also provide precision tests of fundamental laws of physics and be applied to inertia guidance systems of the future. This report describes research on the superconducting gravity gradiometer program at the University of Marylan from July 1980 to July 1985. The report describes the theoretical and experimental work on a prototype superconducting gravity gradiometer. The design of an advanced three-axis superconducting gravity gradiometer is also discussed.

17. KEY WORDS	18. DISTRIBUTION STATEMENT
geophysics gravity measurements gradiometer accelerometers inertial guidance superconductors	Unclassified - Unlimited Subject Category 46

19. SECURITY CLASSIF. (of this report)	20. SECURITY CLASSIF. (of this page)	21. NO. OF PAGES	22. PRICE
Unclassified	Unclassified	214	A10

For sale by National Technical Information Service, Springfield, Virginia 22

NASA-Langley, 1986